Laboratory studies of granular materials under shear: from avalanches to force chains

Thesis by
Eloïse Marteau

In Partial Fulfillment of the Requirements for the
degree of
Doctor of Philosophy

CALIFORNIA INSTITUTE OF TECHNOLOGY
Pasadena, California

2018
Defended October 25, 2017

Eloïse Marteau
ORCID: 0000-0001-7696-6264

ACKNOWLEDGEMENTS

I would like to express my sincere gratitude to my advisor, Prof. José Andrade, whose insight, guidance, and encouragement were invaluable in the course of this work. My time as a graduate student has been extremely enjoyable and I attribute it to this wonderful environment that you provide. I would also like to thank Prof. Domniki Asimaki, Prof. Kaushik Bhattacharya, and Prof. Guruswami Ravichandran for their time and willingness to serve on my committee.

I would like to acknowledge all past and present members of the Computational Geomechanics Group at Caltech who have been wonderful research partners throughout the past years.

I thank the staff at the Mechanical and Civil Engineering department, who have been a helpful resource to help me navigate through graduate school. I would especially like to thank Petros Arakelian for the hours spent troubleshooting in the lab.

I would like to thank my family and friends from all over the world who have provided the support often required when research becomes tedious. Finally, my warmest love goes to Christian for his understanding, patience, and encouragement and for sharing this journey with me.

ABSTRACT

Granular materials reveal their complexity and some of their unique features when subjected to shear deformation. They can dilate, behave like a solid or a fluid, and are known to carry external forces preferentially as force chains. In this dissertation, we employ laboratory experiments to study the complex behavior of granular materials under shear. We introduce a multiscale approach in which the underlying grain-scale mechanics are experimentally measured and homogenized to obtain enriched macroscopic quantities. First, we investigate granular avalanches spontaneously generated by a rotating drum. Measurements of grain kinematics are directly incorporated into a rate-dependent plasticity model that explains and reproduces the life cycle of laboratory avalanches. The results presented here feature dilatancy as the key material parameter governing the triggering of an avalanche. Second, we report a set of experiments performed on a custom-built mechanical device that allows a specimen composed of a two-dimensional analogue granular assembly to be subjected to quasi-static shear conditions. A numerical force inference technique, the Granular Element Method (GEM), provides direct observation and quantitative characterization of force chain structures in assemblies made of realistic grains. Equipped with a complete description of the grain-scale mechanics, we show that shear deformation creates geometrical (fabric) and mechanical (force) anisotropy. Finally, the influence of grain shape on grain-scale processes is studied. We find that grain interlocking is a prominent deformation mechanism for non-circular grains that ultimately promotes a significant increase in macroscopic shear strength. By seamlessly connecting grain-scale information to continuum scale experiments, this dissertation sheds light on the multiscale mechanical behavior of granular assemblies under shear.

PUBLISHED CONTENT AND CONTRIBUTIONS

[1] E. Marteau and J.E. Andrade. "Do force chains exist? Effect of grain shape on force distribution and mobilized strength". In preparation. 2018.
E.M. participated in the conception of the project, designed the experimental setup, performed the experimental tests, prepared the data, and participated in the writing of the manuscript.

[2] E. Marteau and J.E. Andrade. "A model for decoding the life-cycle of granular avalanches in a rotating drum". In: *Acta Geotechnica* (2017). DOI: https://doi.org/10.1007/s11440-017-0609-2.
E.M. participated in the conception of the project, performed the experimental tests, prepared the data, and participated in the writing of the manuscript.

[3] E. Marteau and J.E. Andrade. "A novel experimental device for investigating the multiscale behavior of granular materials under shear". In: *Granular Matter* 19 (2017), p. 77. DOI: https://doi.org/10.1007/s10035-017-0766-x.
E.M. participated in the conception of the project, designed the experimental setup, performed the experimental tests, prepared the data, and participated in the writing of the manuscript.

[4] R. Hurley, E. Marteau, G. Ravichandran, and J.E. Andrade. "Extracting inter-particle forces in opaque granular materials: Beyond photoelasticity". In: *Journal of the Mechanics and Physics of Solids* 63 (2014), pp. 154–166. DOI: https://doi.org/10.1016/j.jmps.2013.09.013.
E.M. designed and performed the experimental test, prepared the experimental data, and participated in the writing of the manuscript.

TABLE OF CONTENTS

LIST OF ILLUSTRATIONS

Chapter 1

INTRODUCTION

1.1 Objectives

This thesis examines the shear behavior and shear strength of dry cohesionless granular assemblies. A key aspect of this work is the combination of laboratory experiments with measurements and modeling techniques that can probe the mechanics of granular materials at various length scales. We present a multiscale approach in which grain-scale mechanics are experimentally measured and ultimately homogenized to obtain enriched macroscopic quantities. An essential aspect to this work is the ability to extract grain-scale quantities using image-based techniques with an unprecedented level of accuracy. First, the shear strength associated with granular avalanches is studied in a rotating drum where, under gravity, a simple shear is achieved, and kinematic properties are measured. Second, we shed light on the multiscale mechanical behavior of granular assemblies under quasi-static shear loading by seamlessly connecting grain-scale information to continuum scale experiments. Of particular interest is the measurement of force chains at the grain-scale, and the concept of critical state at the continuum scale. The proposed experimental procedure provides a powerful tool to deepen our understanding of the grain-scale origin of shear strength in granular materials.

1.2 Granular materials under shear

Granular materials are complex systems that are defined as a collection of distinct grains. The study of these ubiquitous materials is of critical relevance to natural phenomena spanning from earthquakes to landslides and to various industries such as agriculture, mining, and pharmaceutical processing. Several scientific disciplines, including civil engineering, geomechanics, physics, and applied mathematics, have demonstrated substantial interests in accurately modeling the behavior of granular materials. However, due to the diverse and unique characteristics of granular materials, it remains a challenge to describe their overall behavior. The same granular assembly can mimic behavioral features of a solid, a fluid, or even a gas under slightly different conditions [1].

When subjected to shear, granular materials reveal their inherent complexity and some of their unique features. The fundamental properties of granular materials

under shear were first explored by the work of Coulomb (1773) on slope stability in which the theory of frictional resistance for granular materials was pioneered. Reynolds (1885) introduced the notion of dilatancy that describes the ability of granular materials to expand as they are deformed under shear. Both Coulomb's friction law and Reynolds dilatancy are central concepts for understanding the mechanics of granular materials and have implications for current research to this date. Although the scientific study of granular materials has a long history, there remain many outstanding challenges and opportunities, some of which will be discussed throughout this thesis.

In an attempt to lay the groundwork for this thesis, the next section examines our current knowledge and understanding of the shear behavior and shear strength of granular materials. The following discussion focuses on the aspects of granular materials and experimental techniques that are relevant to this work.

1.3 Background

Modeling approaches to granular materials

Early studies in geomechanics focused on modeling the continuum mechanical behavior of granular materials. Constitutive models have been postulated based on phenomenological approaches and empirical measurements, rather than on derivation from underlying grain-scale quantities. The plasticity theory has provided a framework from which many of these constitutive models have emanated. The Mohr-Coulomb model is and remains one of the most frequently used plasticity models in geomechanics and has paved the way for solving practical geotechnical problems.

An important contribution to the continuum modeling of granular materials has come from the 'critical-state soil mechanics' developed at Cambridge University in the 1950s [2–4]. This modeling paradigm hinges on the concept of a critical state that is defined as an equilibrium state where no further changes in volume or stress state occur in a granular assembly with increased shear deformation [3, 4] (see Figure 1.1). When a granular assembly reaches a critical state, it is assumed that the shear strength, normal stress and void ratio are uniquely related. The identification of a critical state has provided a foundation for the development of constitutive models within the plasticity framework [3–5]. While the continuum approach has and will continue to occupy an essential place in the modeling of granular materials, it has limitations: it relies heavily on the use of phenomenology, and its predictive

capabilities are impeded when applied outside of their intended realm.

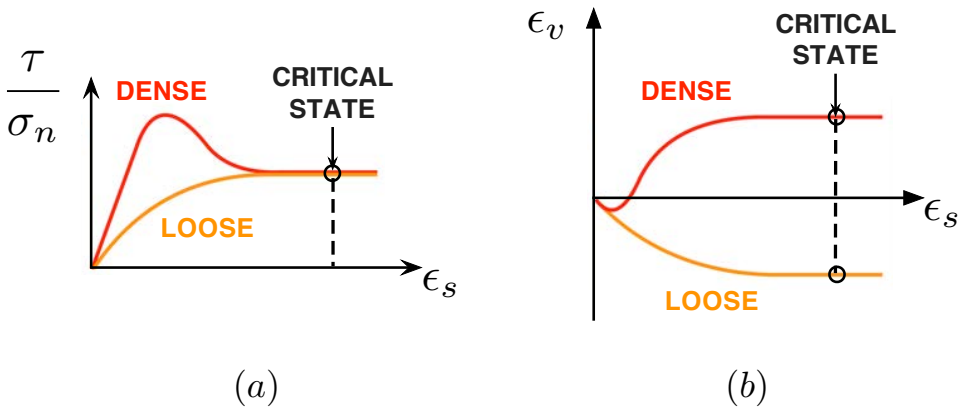

Figure 1.1: Schematics of typical macroscopic response of dense and loose granular samples under shear and (a). Stress ratio τ/σ_n and (b). Volumetric strain ϵ_v as a function of shear strain ϵ_s.

More recently, grain-scale approaches have emerged and provided new insights into properties of granular materials that were simply not accessible to continuum models. The development of grain-scale modeling techniques has been driven by novel experimental techniques and discrete numerical methods. The introduction of X-ray Computed Tomography has enabled to experimentally access grain kinematics [6–8] (i.e., displacements and rotations) and, when combined with X-ray Diffraction, to measure intra-grain strains during macroscopic loading [9, 10]. Nonetheless, such advanced experimental imaging techniques are not always available and involve analyzing a large volume of raw data. As a result, tests performed on quasi two-dimensional (2D) granular systems imaged by a standard digital camera, such as those presented in Chapters 4 and 5 and in [11–13], remain valuable to study the behavior of granular materials. In 2D, full-field measurement techniques, such as Digital Image Correlation (DIC), and force inference techniques, such as photoelasticity and the Granular Element Method (GEM), have been applied to extract grain-scale quantities. Those experimental methods are described in detail in subsequent sections.

The advent of computers gave rise to numerical methods for simulating the behavior of granular materials. Most notably, the Discrete Element Method (DEM) was first introduced by Cundall at al. (1979) [14] based on the idea of solving Newtonian physics for each individual grain in a granular assembly. As DEM provides data on the fabric, grain kinematics, and contact forces, it has been extensively used to investigate grain-scale features of granular materials under various loading conditions

(e.g., [15–19] to name a few). Despite its widespread use, DEM has significant shortcomings: a high computational cost required for simulating a large number of grains, and a lack of quantitative validation against experiments.

As we deepen our understanding at the grain-scale from both experimental measurements and simulations, a major challenge that remains is to develop models that can accurately and efficiently describe the behavior of granular materials by incorporating information at various scales.

Granular avalanches

Most continuum modeling approaches mentioned in the last section concern quasi-static deformations of granular materials. Besides quasi-static deformations, where a granular assembly behaves like a solid, the same assembly can also flow like a fluid. A granular avalanche, as studied in Chapter 2, marks the transition between these distinct solid-like and fluid-like states. The solid-like state is classically described using the plasticity models emanating from critical-state theory. Theoretical and experimental studies of granular materials deformed under quasi-static conditions have shown that the strength of granular materials can be decomposed into a dilatancy strength and a residual strength [4, 20, 21]. The strength provided by Reynolds dilatancy [22] typically vanishes toward the critical state where no further change in volume occurs. At the critical state, the material strength is only furnished by the residual resistance, which is considered to be constant and rate-independent according to classical soil mechanics [4].

In the fluid state, much attention from the physics community has been given to granular flows in the steady regime. Numerous experiments and DEM simulations have been performed on various geometries (plane shear, inclined plane, rotating drum, etc. [23]) in an attempt to define constitutive laws for granular flows. Such studies have led to the development of a local rheology based on a unique relation between the friction coefficient μ and the dimensionless inertial number I [24–26], where I is understood as the ratio of the macroscopic timescale to displace a layer of particles imposed by the shear rate and the microscopic timescale for particle rearrangements controlled by the pressure [23–26]. This phenomenological law for steady granular flows in combination with continuum conservation equations correctly describe the velocity and stress fields in various flow geometries [25, 27].

These efforts have been mainly focusing on uniform steady flows, and, as a consequence, our understanding of the mechanism governing the solid-fluid-like transition

remains limited. Modeling this transition is of practical importance in geomechanics and for various industries. In Chapter 2, we explore the transition between solid and fluid states occurring during an avalanche by combining rotating-drum experiments with a rate-dependent plasticity model [28].

Measuring contact forces using photoelasticity

Granular materials are known to carry external forces through so-called force chains. Within this force network, relatively small groups of particles carry significant forces while a comparably small load is borne by the adjacent particle. This heterogeneous force network was first observed through experiments using photoelastic materials [29, 30] (see Figure 1.2).

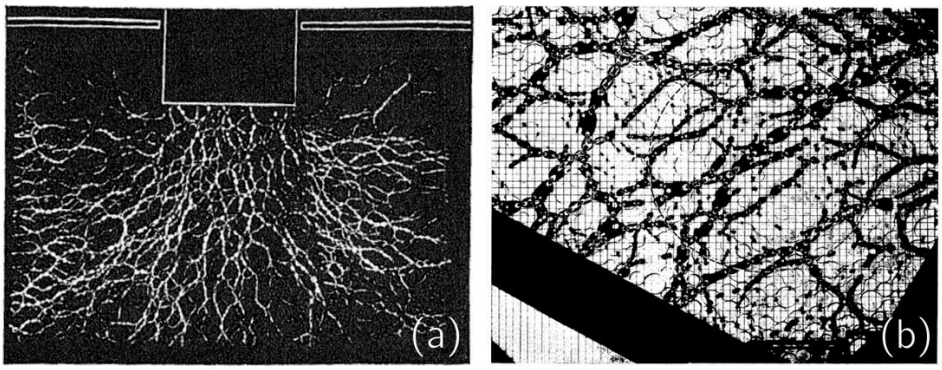

Figure 1.2: Historical examples of force chains visualized with photoelasticity (a). Source: reprinted from Dantu [29], (b). Source: reprinted from Drescher and de Josselin de Jong [30].

Photoelasticity technique applied to idealized granular materials has a longstanding history. This method uses grains made of photoelastic materials (e.g., many transparent glasses and plastics such as urethane and acrylic), which exhibit stress-induced birefringence under loading. Birefringence causes a change in the polarization state of the transmitted light, resulting in the formation of interference fringes (see Figure 1.2). The intensity of these inference fringes is directly related to the difference of principal stresses $\sigma_1 - \sigma_2$ within the material through the stress-optic law [31, 32].

Originally, photoelastic images 1.2 were used for qualitative studies only [29, 30]. Capability to infer contact forces was later developed by Behringer et. al (2005) [33]. Given the data obtained from photoelastic images, it is possible to solve an inverse problem to infer contact forces in the granular assembly [34]. The goal is to determine the vector of contact forces that results in measured difference of

principal stresses $\sigma_1 - \sigma_2$. This experimental method relies on the knowledge of the analytical solutions for the stress created by point contact forces on a disk [31, 32]. Prior to running experiments, a calibration test where a disk is diametrically compressed by a known force must be performed in order to relate the force to the difference of principal stresses $\sigma_1 - \sigma_2$ and thus, to the fringe patterns.

Photoelasticity has played an important role in our understanding of force transmission in granular materials. Studies using photoelasticity to infer contact forces have examined the probability distribution of contact forces [33], buckling of force chains [35], force network dependence on shear rate [36], evolution of shear jammed states [12], shear in an analogue to geological faults [37], follow slow dynamics under shear [38, 39], and quantify fast dynamics [40–42]. It is important to note that these studies have been performed on a specific type of granular assemblies as photoelasticity requires the use of birefringent grains with simple geometry (disks or ellipses). In comparison to photoelasticity, the force inference method presented in Chapter 3 (GEM) exhibit the significant advantage to be applied to complex materials of arbitrary shape and opacity. We will show in Chapters 4 and 5 that GEM has great potential for yielding more understanding of granular systems.

Digital Image Correlation (DIC)

Since its development in the 1980s, Digital Image Correlation (DIC) has been widely used in the field of experimental soils mechanics [7, 43, 44]. The laboratory studies presented in these thesis hinge on DIC's ability to measure grain kinematics. 2D-DIC provides displacements, rotations, and full-field strain measurements by comparing the gray intensity levels of the specimen surface before and after deformation. We present here the basic principles of 2D-DIC, briefly describe its numerical algorithm, and give practical considerations for accurate measurements.

The first step of any DIC measurement is the acquisition of digital images at different states. The next step involves the definition of regions of interest (ROI) in the reference image. The DIC procedure is based on tracking the same pixels between reference and deformed images as shown in Figure 1.3. To perform this tracking, a correlation window, also called subset, is chosen and deformed until the pattern in the deformed image matches the pattern in the reference image as closely as possible. The degree of similarity between the reference and deformed subsets is computed using a correlation coefficient C. The matching procedure is achieved by detecting the position of the correlation coefficient peak, as illustrated in Figure 1.3.

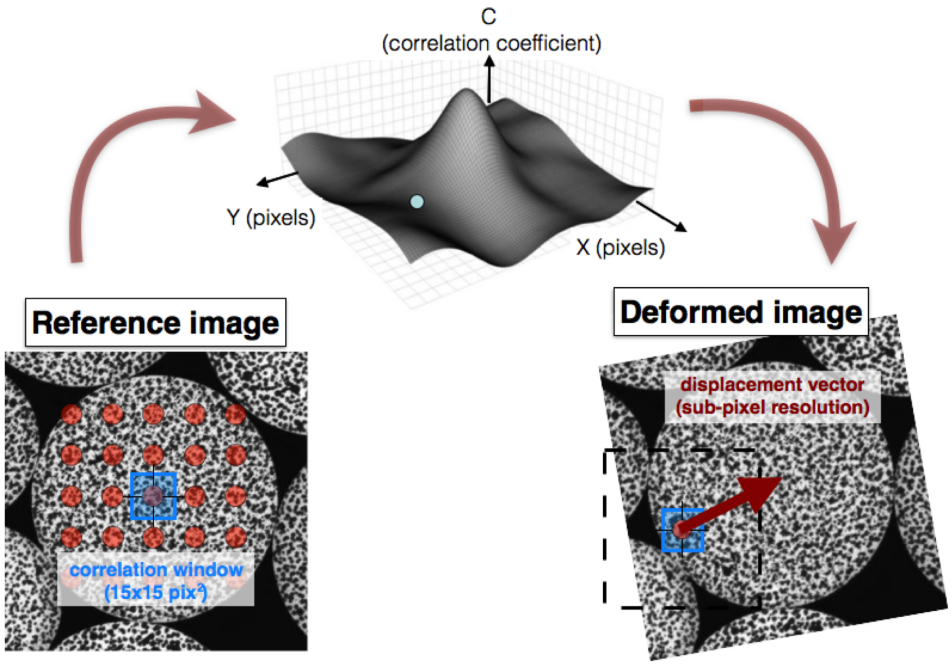

Figure 1.3: DIC concept. Comparison between reference and deformed images is performed using a correlation coefficient C

Once the position of the deformed subset is determined, the in-plane displacement is obtained by calculating the difference between the position of each point in the reference subset and the position of the corresponding point in the deformed subsets. The shape of the reference subset may be changed in the deformed image. The relation between point (x_i, y_j) of the reference image and point (x_i', y_j') of the deformed image is defined by:

$$\begin{aligned} x_i' &= x_i + \xi(x_i, y_j) \\ y_j' &= y_j + \eta(x_i, y_j) \end{aligned} \tag{1.1}$$

where $\xi(x_i, y_j)$ and $\eta(x_i, y_j)$ are the shape functions. First-order shape functions are used to depict the following deformation states: translation, rotation, shear, normal strains, and their combinations. The correlation coefficient C can be optimized using sub-pixel algorithms to detect sub-pixel locations and thus improve the accuracy of the displacement measurement. Finally, the strain field is computed by numerical differentiation of the displacement field. A typical intra-grain field measurement is showcased in Figure 1.4b.

The accuracy and resolution of DIC measurements strongly relies on a high-contrast, non repetitive, isotropic pattern applied to the specimen's surface [45]. Practically, if

the specimen does not present a natural random pattern, a speckle pattern is created by applying a coat of standard off-the-shelf flat white on which black speckles are added using black spray paint or marker. A typical speckle pattern generated on a grain surface with the described procedure is presented in Figure 1.4a.

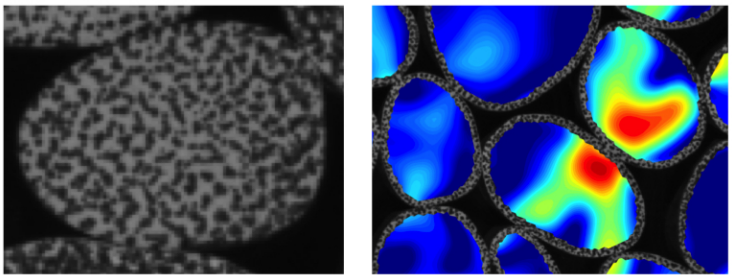

(a) (b)

Figure 1.4: (a). Grain surface prepared with a random high-contrast speckle pattern.(b). Typical intra-grain surface measurement obtained with 2D-DIC.

The accuracy, precision, and resolution of DIC measurements also depends on the choice of a set of parameters, including subset size and strain computation window [46]. The choice of this set of parameters is user-defined and is made according to the specific application. As a rule of thumb, the subset size should be larger than the speckle size to allow for optimal tracking but not unnecessarily large to avoid loss of resolution. To minimize systematic errors due to lens distortion, an appropriate calibration should be performed [47]. We point out that such errors can be completely eliminated with telecentric lenses [48] or by using 3D-DIC to measure and correct for out-of-plane deformation.

1.4 Scope of the thesis

The layout of this thesis is as follows. In Chapter 2, we employ laboratory experiments of transient avalanches spontaneously generated by a rotating drum. We report measurements of dilatancy and grain kinematics before, during, and after each avalanche. Those measurements are directly incorporated into a rate-dependent plasticity model that quantitatively predicts the granular flow measured in experiments. Furthermore, we find that dilatancy in the solid-like state controls the triggering of granular avalanches and therefore plays a key role in the solid-fluid-like transition. With the proposed approach, we demonstrate that the life cycle of a laboratory avalanche, from triggering to runout, can be fully explained.

Chapter 3 describes the Granular Element Method (GEM), a technique for inferring

contact forces in quasi-static experiments. GEM combines experimental imaging techniques with equations governing particle behavior to allow force inference in cohesionless materials with grains of arbitrary shape, texture, and opacity. We present the numerical framework and an example of contact force inference in granular materials under compression.

Chapter 4 introduces a novel mechanical device that allows a specimen composed of a two-dimensional opaque granular assembly to be subjected to quasi-static shear conditions. A complete description of the grain-scale quantities that control the mechanical behavior of granular materials is extracted throughout the shear deformation. Geometrical arrangement, or fabric, is quantified by means of image processing, grain kinematics are obtained using Digital Image Correlation (DIC), and contact forces are inferred using the Granular Element Method (GEM). Aiming to bridge the micro-macro divide, macroscopic average stresses for the granular assembly are calculated based on grain-scale fabric parameters and contact forces. The experimental procedure is detailed and validated using a simple uniaxial compression test. Macroscopic results of shear stress and volumetric strain exhibit typical features of the shear response of dense granular materials and indicate that critical state is achieved at large deformations. At the grain scale, attention is given to the evolution of fabric and contact forces as the granular assembly is sheared.

In Chapter 5, we present results on force transmission and shear strength in an arbitrarily-shaped assembly. Grain shapes are directly extracted from a real sand sample and manufactured using 3D-printing technology. We analyze the effect of grain shapes on the grain- to continuum-scale response of sheared granular materials. Investigated grain-scale quantities include the average grain rotation, the coordination number, and the distribution of contact forces. Moreover, the different grain-scale mechanisms underpinning the shear strength of granular materials are geometrically identified. We report that grain interlocking creates a stable structure that leads to significantly higher shear strength in arbitrarily-shaped samples.

Chapter 6 offers concluding remarks, and ongoing and future works are outlined.

Chapter 2

A MODEL FOR DECODING THE LIFE-CYCLE OF GRANULAR AVALANCHES IN A ROTATING DRUM

2.1 Introduction

Laboratory experiments and discrete element simulations carried out on dry cohesionless particles have revealed the complexity of granular flows [1, 23, 49–51]. A striking characteristic of granular materials evidenced during transient avalanches is their unique ability to exhibit both solid and fluid properties [23, 49]. While a few efforts have been made to unify the solid-like and fluid-like behavior [52–55], no constitutive model has yet been applied to simulate the life-cycle of a granular avalanche.

It is well-known that a granular material confined in a half-filled drum that is rotating at a slow angular velocity ω and undergoes a series of transient avalanches [51]. Initially, the inclination angle θ of the free surface of the material increases linearly with time at the rate ω. Experiments show that the granular material remains perfectly static until the free surface reaches the maximum stable inclination angle, called the angle of avalanche θ_A [51]. Once the critical inclination angle θ_A is exceeded, an avalanche is spontaneously released: under gravity [56], a thin layer of grains close to the free surface flows rapidly downslope. The inclination angle θ decreases until the grains stop flowing. The inflection point in the time evolution of the inclination angle occurs when the surface velocity reaches a maximum and is referred to the angle of peak velocity θ_V. After the avalanche, the grains reassume a static structure and rest at a lower angle called the angle of repose θ_R [57]. Further rotation leads to another avalanche and the phenomenon is repeated. A typical avalanche event is depicted in Figure 2.1. Despite the apparent simplicity, the mechanism causing an avalanche to trigger and later to stop remains unknown. This work elucidates the avalanche triggering mechanism and the underlying cause of the difference $\Delta\theta$ between the angle of avalanche θ_A and the angle of repose θ_R.

2.2 Experimental method

To investigate the origin of $\Delta\theta$, we devised experiments of granular assemblies subjected to external shearing forces imposed by the rotation of a drum. A picture of the experimental setup and imaging system is shown in Figure 2.2. For simplicity,

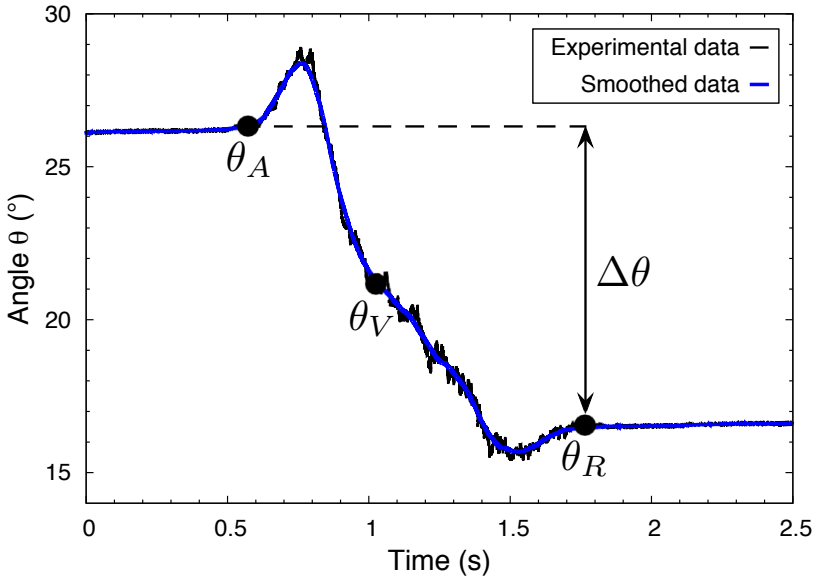

Figure 2.1: Experimental measurements of the inclination angle θ as a function of time. The black curve represents the value of the inclination angle θ obtained using image processing. The experimental data are then fitted using a smoothing spline [58]. The smoothed data is represented by the blue curve.

and in light of existing work [23, 25, 26, 51, 59], we consider an assembly of dry monodispersed spheres. Our experimental setup, shown in Figure 2.2 and in the inset of Figure 2.4, consists of a drum half-filled with steel beads of 1 mm diameter. The drum, of inner diameter 30 cm and inner width 16 mm, is slowly rotated at constant angular velocity ω of 0.05 revolutions per minute. After randomly pouring the steel beads into the drum, the container is slowly rotated for a sufficient amount of time so that tens of transient avalanches occur. This procedure enables us to prepare the granular assembly in a reasonably consistent initial arrangement prior to the start of each run and settles the granular assembly to an initial packing fraction of $\phi_0 \approx 0.60$. A high-speed camera PHANTOM V310 is used to capture the progressive response of the particles. Images of 640×480 pixels are acquired at a rate of 10,300 frames per second with a spatial resolution of 0.07 mm.

At slow angular velocity ω, experiments show that the free surface inclination angle θ has a linear profile [51, 60]. Quantitative measurements of the inclination angle θ are obtained with image processing techniques. The step-by-step process is illustrated in Figure 2.3. Gray images are first converted into binary images based on a threshold (see Figure 2.3b). Thresholding segments the image into background (segment with value 0) and solid (segment with value 1). The threshold value is

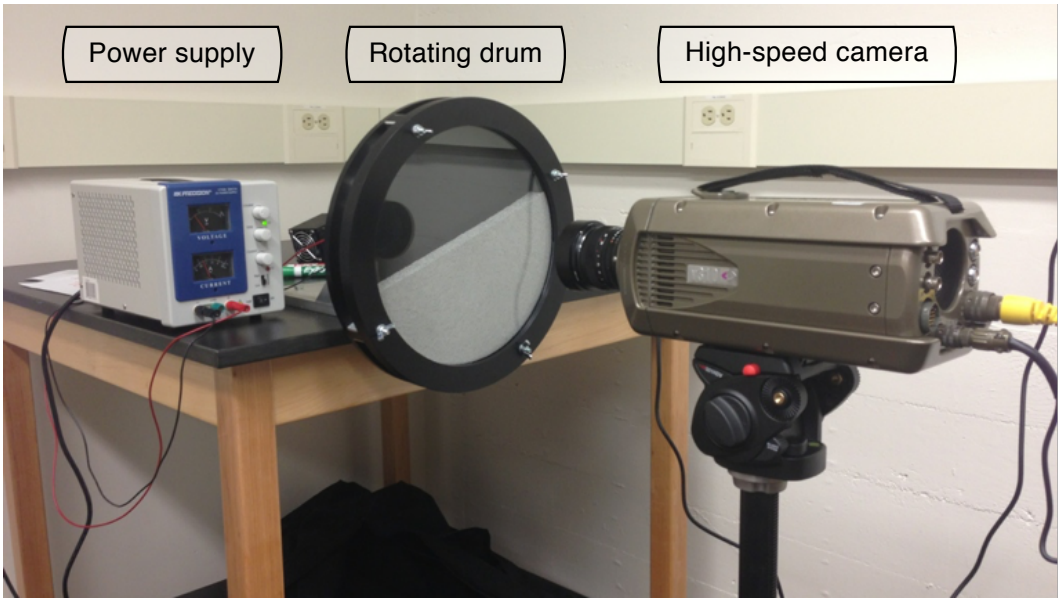

Figure 2.2: Experimental setup for studying granular flow in a rotating drum

carefully selected by observation alone to get the best representation of the grains in the images. After the binary conversion, we apply a morphological closing in order to selectively fill in particular regions of the binary images. We then obtain a binary image (see Figure 2.3c) where the background is colored black while the grains are white. We compute a least squares fit of the edge line defining the free surface boundary between the grains and the background. The slope of the best-fitting line corresponds to the value of the inclination angle θ.

The Digital Image Correlation (DIC) technique [61, 62] is applied to the images to extract the average shear strain ϵ_S, the average volumetric strain ϵ_V and the surface velocity v. The images are correlated using a subset (correlation window) size of 25×25 pixels and a step size of 1 pixel. The subset size is selected such that a trade-off between spatial resolution and measurement error can be found. We estimate the measurement error by correlating two subsequent images of the grains taken when the drum is not subjected to rotation. The values of the resulting displacements for different subset sizes are then compared in order to determine a subset size that minimizes measurement error. The surface velocity estimation technique involves the measurement of the surface displacement u using DIC. The surface displacement u is evaluated within a region of interest of width and height of respectively 30 grains and 2 grains, located at the center of drum close to the free surface (see Figure 2.3d). This resultant displacement, when combined with

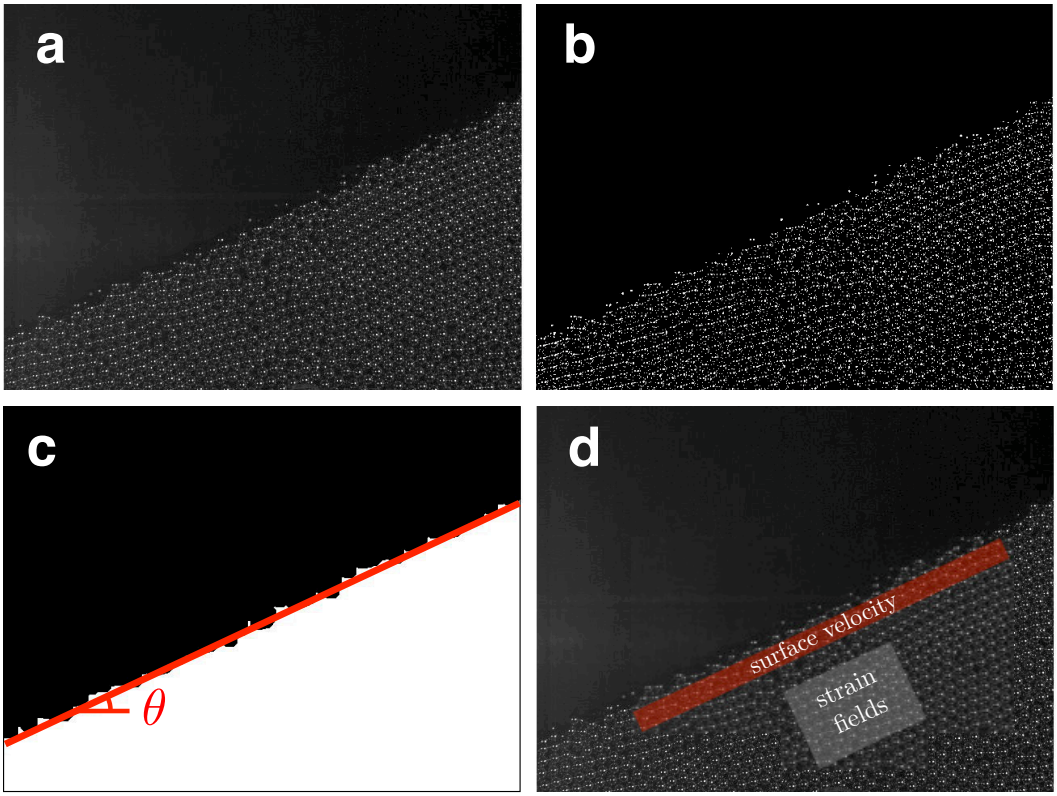

Figure 2.3: Step-by-step image processing technique. a. Original image. b. Thresholding. c. Binary image and least square fit of the free surface boundary. d. Regions of interest for DIC measurements of the surface velocity v and strain fields (shear strain ϵ_S and volumetric strain ϵ_V).

the known frame rate, gives a measure of the surface velocity v. An average value of the surface velocity v is then computed over the region of interest. In order to experimentally compute the dilatancy, we use the DIC method to measure the values of the average shear strain ϵ_S and the average volumetric strain ϵ_V. We select a region of interest of 12×8 grains centered about 6 grains below the free surface (see Figure 2.3d). By comparing pairs of consecutive images, the DIC method enables to determine in-plane displacement and thus full-filed strain. Given the strain components (ϵ_{xx}, ϵ_{yy} and ϵ_{xy}), we compute the principal strains ϵ_1 and ϵ_2 from which the shear strain ϵ_S and the volumetric strain ϵ_V are derived as follows:

$$\epsilon_V = \epsilon_1 + \epsilon_2 \quad \text{and} \quad \epsilon_S = \epsilon_1 - \epsilon_2 \tag{2.1}$$

Subsequently, the average values of each strain component are evaluated over the region of interest. We plot the resulting evolution of average volumetric strain ϵ_V

as a function of average shear strain ϵ_S (see Figure 2.4). In order to determine the maximum dilatancy β^*, the curve of average volumetric ϵ_V versus average shear strain ϵ_S is smoothed using a cubic spline interpolant [58] (not represented in Figure 2.4). The maximum dilatancy β^* (depicted in Figure 2.4) corresponds to the maximum slope value of the smoothed curve. In order to ensure repeatability and consistency of the results, the experimental procedure and data analysis described herein are repeated for three different runs.

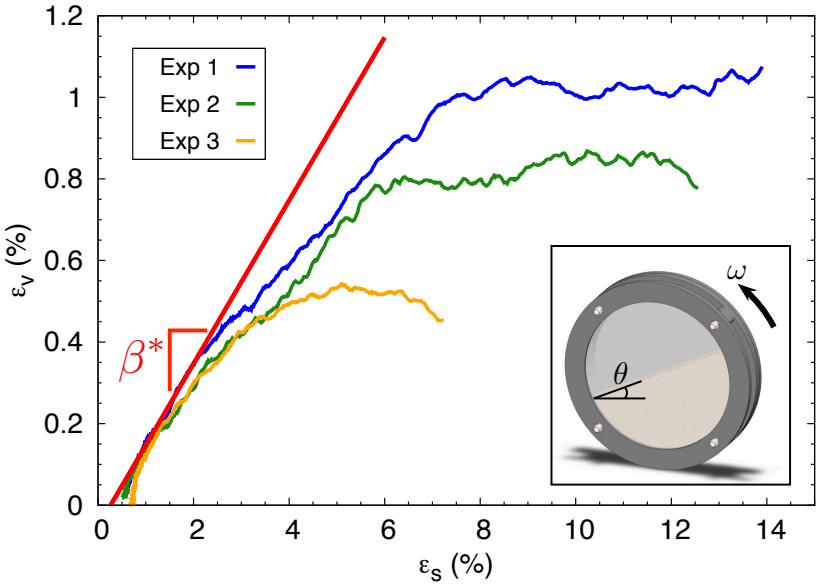

Figure 2.4: Evolution of the average volumetric strain as a function of the average shear strain measured using DIC for three different avalanche events. β^* denotes the maximum average value of dilatancy. Inset, sketch of the experimental rotating drum. Definition of the inclination angle and angular velocity ω.

2.3 Constitutive model

To help explain and reproduce the life-cycle of an avalanche observed in the experiments, we use a constitutive model recently postulated by Andrade et al. [52]. The key feature of this model is its ability to account for the transition from solid-like material behavior, which is well described by rate-independent plasticity theory [4], to fluid-like material behavior, in which the material behaves as a non-Newtonian fluid [25, 26]. The constitutive model is based on the Coulomb friction law that couples the shear stress τ to the normal stress σ by the mobilized friction coefficient μ, which describes the strength of the material. When the inequality $\tau < \mu\,\sigma$ holds, the material is at equilibrium and behaves as a rigid body. At the onset of flow, the force balance can be expressed in terms of the inclination angle θ, such that tan

$\theta = \mu$. Once the granular assembly flows, the driving force provided by gravity has overcome the critical threshold. By considering a uniform infinite flow, the governing equation of the granular flow can be derived from the linear momentum balance equation (see Appendix):

$$\frac{a}{g} = \cos\theta\,(\tan\theta - \mu) \tag{2.2}$$

where a is the surface acceleration, g is the gravitational acceleration, θ is the inclination angle, and μ is the mobilized friction coefficient. We assume that the mobilized frictional resistance is expressed as a function of dilatancy and residual resistance [4, 20], such that the following additive decomposition holds:

$$\mu = \beta + \bar{\mu} \tag{2.3}$$

In the previous equation, $\bar{\mu}$ is the residual resistance of the material. The Reynolds dilatancy [22, 63], expressed by β in equation (2.3), describes the change in volume associated with the shear distortion of compacted granular materials [4], and relates the volumetric and shear strain rates by $\dot{\epsilon}_V = \beta\,\dot{\epsilon}_S$. Assuming quasi-static conditions ($\dot{\epsilon}_S \approx 0$), classical soil mechanics has considered the residual resistance $\bar{\mu}$ constant. We postulate that, in the solid-like state, the residual resistance of the material is defined by a constant material parameter μ_l, making the total frictional resistance $\mu = \beta + \mu_l$. In the fluid-like state, the granular material reaches critical state [24] in which the dilatant effect no longer occurs ($\beta = 0$) and the material strength is only furnished by the residual resistance $\bar{\mu}$, so that $\mu = \mu_l$. Once the avalanche stops at $\theta = \theta_R$, the granular assembly is still at critical state ($\beta = 0$) but reassumes a solid-like state in which the total frictional resistance $\mu = \mu_l$. Hence, according to equation (2.2), the value of the parameter μ_l is given by $\mu_l = \tan\theta_R$. These assumptions are consistent with experimental observations [24–26] and theory [20], where the solid-like behavior is controlled by dilatancy and the residual resistance controls the fluid-like behavior. However, consolidating these views is critical in explaining the onset and life-cycle of granular avalanches. Further, laboratory experiments on steady flows [24, 25] have shown that the residual resistance $\bar{\mu}$ is distinctly rate-dependent. By reformulating the constitutive law proposed by Jop et al. [24, 25], we introduce a simpler expression taking into account the rate dependency that can be expressed as:

$$\bar{\mu} = \mu_l + \frac{\mu_u - \mu_l}{1 + \frac{\dot{\epsilon}_S^*}{\dot{\epsilon}_S}} \tag{2.4}$$

According to this empirical relation, the residual resistance $\bar{\mu}$ starts from a lower value $\mu_l = \tan\theta_R$ for zero shear rate and converges asymptotically to μ_u as the speed of shearing $\dot{\epsilon}_S$ increases. The upper bound μ_u would correspond to the transition between the flow regime and the gaseous regime [1, 25], where the constitutive law (2.4) no longer applies. In equation (2.4), $\dot{\epsilon}_S^*$ is set to be the value of the shear rate at which the surface velocity v reaches its peak value (and therefore at which the acceleration $a = 0$) and at which the inclination angle is equal to the angle of peak velocity θ_V. It is clear from equation (2.4) that $\dot{\epsilon}_S^*$ also corresponds to the shear rate at which the residual friction $\bar{\mu} = 1/2\,(\mu_u + \mu_l)$. Consequently, at $\dot{\epsilon}_S = \dot{\epsilon}_S^*$, as the acceleration $a = 0$ and the inclination angle $\theta = \theta_V$, equation (2.2) gives $\tan\theta_V = \bar{\mu} = 1/2\,(\mu_u + \mu_l)$, from which we can deduce the value of the parameter μ_u. This model unifies the solid-like and fluid-like behavior under a simple plasticity framework that is used to interpret experimental observations of transient granular avalanches.

2.4 Results and discussion

Typical volumetric versus shear strain curves (ϵ_V vs. ϵ_S) obtained in experiments are plotted in Figure 2.4. We observe that the granular sample initially expands (dilates) until it reaches a constant volume at large shear deformation. The measured dilatancy β, indicated by the slope of the volumetric strain-shear strain curve, reaches a maximum value β^* for small shear deformation. In Figure 2.4, even though the system for the three different runs stabilizes at different plateau values of the volumetric strain, the peak of dilatancy β^* obtained at small shear deformation is roughly the same. Measurements of the maximum dilatancy β^* give a mean value of $\beta^* = 0.20$ and a standard deviation of 0.007.

In Figure 2.5a, we report measurements of the inclination angle θ (black curve) and the proposed plasticity model predictions of the inclination angle θ_{MODEL} (blue dots) obtained by solving equation (2.2) using the Newton-Raphson method. In Figure 2.5a, we highlight the time interval at the onset of an avalanche in which the dilatancy measurements are carried out (red shade). Measurements of the surface velocity v as a function of time are depicted in Figure 2.5c. The time evolution of the surface velocity v initially increases from zero to a maximum value and later

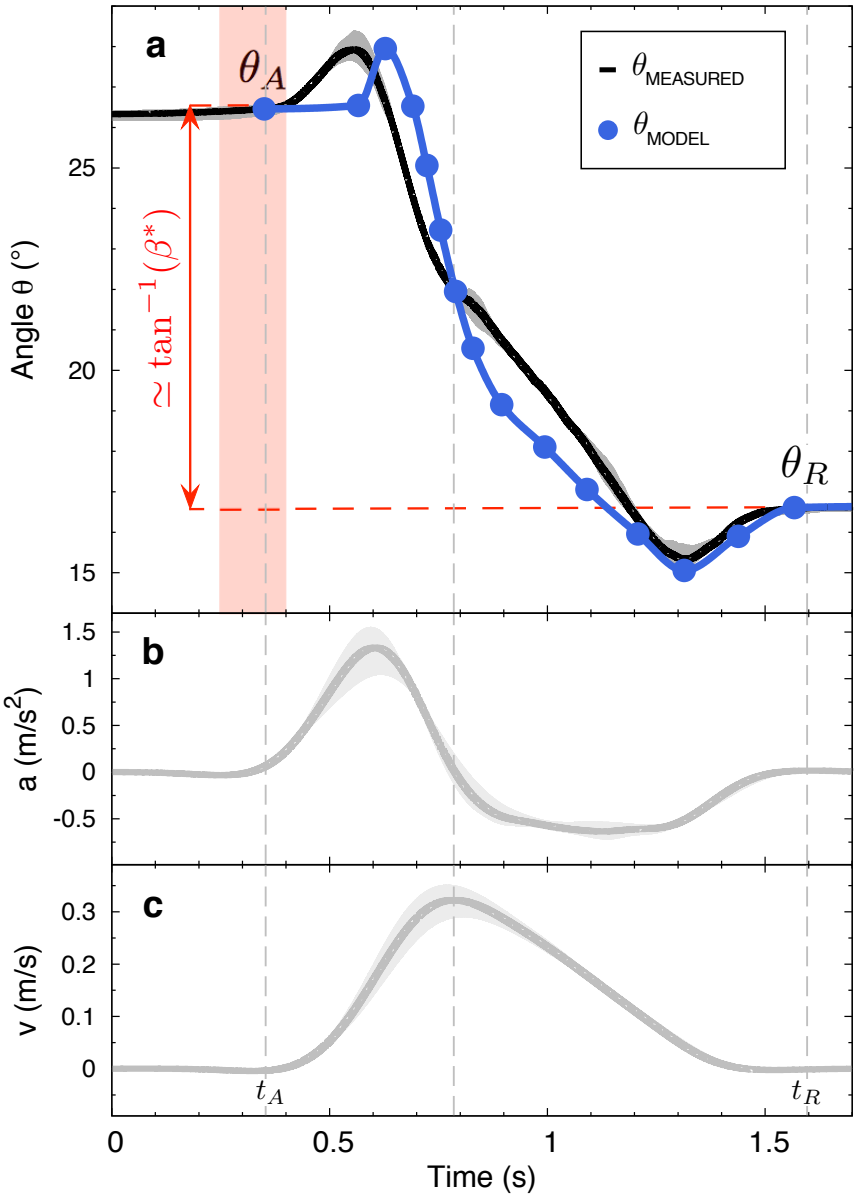

Figure 2.5: Evolution of the inclination angle θ and kinematics as a function of time and comparison with the theoretical model. The bold curves correspond to the mean value of the three experiments at every time step. The shades correspond the maximum and minimum value of the three runs. The red shade represents the time interval in which the dilatancy measurements are performed.

decreases at a slower rate towards zero (at rest) [64]. It is noteworthy that the peak of surface velocity v coincides with the angle of peak velocity θ_V (Figure 2.5). The surface acceleration a (Figure 2.5b) is obtained by differentiation of the surface velocity v. This kinematics are used as input in equation (2.2) to solve for the model predictions of the inclination angle θ_{MODEL}. As suspected by related work [64–67], the results presented here feature dilatancy as the key material parameter governing the onset of flow. Indeed, when the peak of dilatancy β^* occurs, the frictional resistance μ reaches the yield criterion $\mu = \tan\theta$, and an avalanche is triggered. Furthermore, our constitutive model (see Appendix) and statistics of dry granular avalanches [68] reveal that the angle at which an avalanche ends is correlated to the the angle at which an avalanche starts. In particular, our experimental results show that the difference in angles is fully explained by the peak of dilatancy such that $\tan^{-1}\beta^* \approx \Delta\theta$. Dilatancy seems to give the additional strength to the material that allows a transient avalanche to start at an angle θ_A, measurably higher than the angle of repose θ_R. It should be noted that each avalanche removes a layer of granular material and deposits it at the toe of the slope. A new avalanche occurs by mobilizing the layer of granular material that was just underneath the material in the previous slope. This helps explain the re-setting or availability of dilatancy at every avalanche cycle. This initial dilatancy is measured during the time interval shown in Figure 2.5a. The plasticity model (blue dots) captures the fluid-like behavior of the granular media observed in experiments (black curve) well. These results confirm a clear dependence of the residual resistance $\bar{\mu}$ on shear rate. Moreover, our experimental results reveal the existence of a peak and a trough in the inclination angle curve observed respectively at the beginning and at the end of the flow (Figure 2.5a). To our knowledge, such distinctive features have not been reported before in the literature on granular avalanches. Our constitutive model suggests that these features are induced by the rate of change of acceleration $\dot{a} = da/dt$. To justify this, we examine the sign of the rate of change of the inclination angle $\dot{\theta} = d\theta/dt$ near the angle of avalanche θ_A and the angle of repose θ_R. By taking the derivative of the governing equation (2.2) with respect to time, we derive an expression for $\dot{\theta}$:

$$\dot{\theta} = \frac{1}{\mu \sin\theta + \cos\theta}\left(\frac{\dot{a}}{g} + \cos\theta\, \dot{\mu}\right) \tag{2.5}$$

It can be seen from our constitutive framework, given in equation (2.3), that, for $\beta > 0$, the value of the mobilized friction resistance remains positive for all time. Furthermore, during an avalanche, $0 < \theta < \pi/2$ and $\forall$ t, $\cos\theta \geq 0$ and $\sin\theta \geq 0$.

Consequently,

$$\forall t, \quad \frac{1}{\mu \sin\theta + \cos\theta} > 0$$

We recall that, once the avalanche has been triggered, the granular assembly is in a fluid-like state and we have $\mu = \bar{\mu}$. In particular, as $\theta \to \theta_A$ and $\theta \to \theta_R$, the surface velocity $v \approx 0$ and the shear rate $\dot{\epsilon}_S^* = \frac{v}{h} \approx 0$ (where h is the average thickness of the moving grains). Using equation (2.4), we can conclude that, as θ approaches the angle of avalanche θ_A and the angle of repose θ_R, $\mu \to \mu_l$ and hence $\dot{\mu} \to 0$. It follows from equation (2.5) that $\mathrm{sgn}(\dot{\theta}) = \mathrm{sgn}(\dot{a})$, where sgn represents the sign function. From Figure 2.5b, it can be seen that, as t approaches t_A from the right ($t \to t_A^+$), the rate of change of the acceleration $\dot{a}$ is positive. Accordingly, we have $\dot{\theta} \geq 0$ hence the occurrence of a peak in the inclination angle θ curve after the triggering. Similarly, for $t \to t_R$, Figure 2.5b shows that the rate of change of the acceleration $\dot{a}$. It follows that $\dot{\theta} \geq 0$ which results in the formation of a trough in the inclination angle curve prior to the runout. We emphasize that, for the given experimental parameters (material properties, angular velocity, etc.), the peak and trough of inclination angle occur in each performed experiment. Finally, we highlight that important features of transient granular avalanches, such as triggering, evolution of the flow and runout [50] correspond to zero surface acceleration a (see Figure 2.5) and are quantitatively captured by the proposed model.

2.5 Conclusion

In conclusion, we employed a simple rate-dependent plasticity model that has been able to reproduce the key features of the life-cycle of an avalanche observed in drum experiments. In particular, our constitutive model, assuming uniform infinite flow, explains the formation of a peak and a trough observed in the inclination angle curve, respectively after triggering and during runout. Further studies (involving, in particular, the influence of the sample preparation and initial packing fraction) remain necessary, however, to fully understand the origin of these specific features. Dilative strength has a clear influence on the transition between the solid-like and fluid-like states and explains the difference between the angle of avalanche θ_A and the angle of repose θ_R. The remainder of the curve seems to be controlled by the residual strength of the material, which is clearly rate-dependent. Hence, both the dilative behavior and the residual strength together are able to explain the beginning, evolution, and end of the life-cycle of granular avalanches. The

comprehensive description of laboratory avalanches clarifies the physical origin of the phenomenon and may open the door for a deeper understanding of natural hazards such as landslides.

Chapter 3

THE GRANULAR ELEMENT METHOD: EXPERIMENTAL FORCE INFERENCE TECHNIQUE

3.1 Introduction

The mechanical behavior of granular materials is fundamentally encoded at the grain-scale. A major goal in the study of granular materials has therefore been to characterize grain-scale information. Advances in experimental techniques (e.g., X-ray Computed Tomography [7, 9, 69]) and computational methods (e.g., Discrete Element Method [14]) have enabled access to grain-scale fabric, kinematics and contact forces.

Contact forces have received extensive attention as there is a strong interest in understanding their role on the mechanical response of samples as well as on the microstructure of granular assemblies. Studies have investigated relations between contact forces and bulk properties [15, 70]. Extensive research has focused on evaluating the statistical distribution of contact forces [33, 71–77]. Many models have emerged to simulate the observed heterogeneities of force networks [73, 78, 79]. The progress and success of these studies is intimately linked to the ability to validate theories with experiments on real granular materials. To this end, experimental techniques for inferring contact forces are essential.

Several experimental techniques have historically provided powerful methods for inferring contact forces in granular materials. Contact forces in granular assemblies were first observed optically in packings of idealized photoelastic particles, which have the property to develop birefringence by the application of stress ([30, 38]). While photoelasticity has and will continue to occupy an important place in the study of granular materials, it has many limitations: it requires the use of birefringent grains with simple geometries, is difficult to implement in three dimensions, and it often requires knowledge of boundary forces for accurate results [31, 32]. Other methods proposed recently attempt to overcome some of these limitations but are also restricted to particular materials or grain shapes (see e.g., [80, 81]).

The methodology presented in this chapter leverages emerging experimental techniques to overcome many of these limitations. The Granular Element Method (GEM) [52, 82] combines a mathematical framework with experimental data to

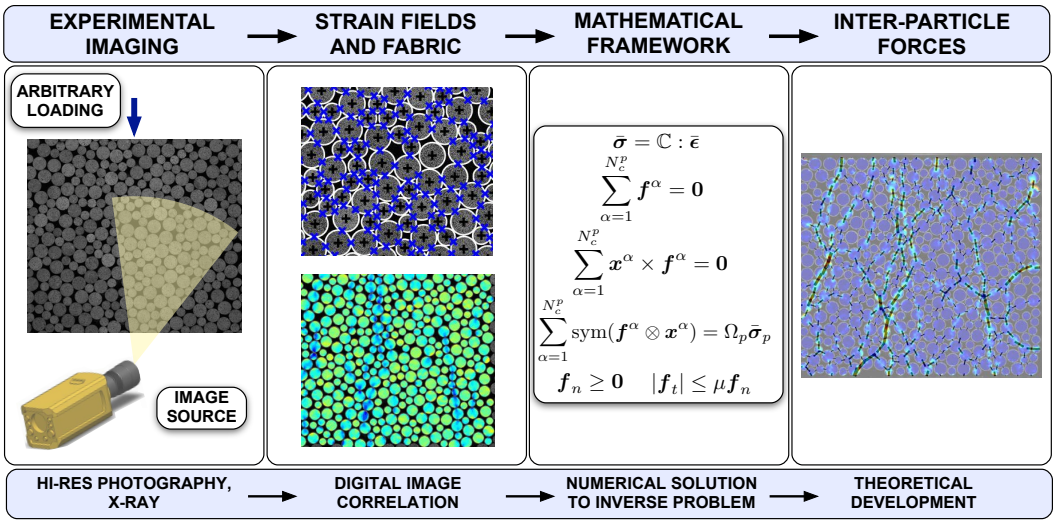

Figure 3.1: The GEM methodology for contact force-inference presented in this chapter. Experimental imagining techniques provide rich data sets for extracting grain strain fields and material fabric. These ingredients are input for a mathematical framework which yields contact forces by solving an appropriate inverse problem. Variables and equations in panel 3 are described in section 3.3

infer contact forces in granular assemblies with grains of arbitrary shape, texture and opacity. The method has been successfully applied to two-dimensional systems under quasi-static conditions [82], dynamic load [83] and, more recently, to a three-dimensional system [10]. While the number of grains involved in the first experimental example of applying 2D-GEM under quasi-static conditions [82] was relatively small, we demonstrate in this chapter that the force inference technique works for larger granular systems.

The GEM methodology can be visualized in Figure 3.1 and consists of two main stages. First, experimental imaging techniques are used to extract information about the geometric arrangement of the granular assembly and the average grain stresses. Secondly, this information is taken as input for the constrained optimization problem, whose solution is the desired contact forces. The subsequent sections give a thorough and general description of the experimental measurements required by 2D-GEM and the constrained optimization problem.

3.2 Experimental measurements

The first step of the GEM methodology consists of acquiring a set of digital images of a granular assembly under arbitrary loading conditions. The second step of the method involves extracting information about the fabric (grain shape, contact, and

centroid locations) and average grain stresses at each time step. These measurements constitute the inputs for GEM and, once experimentally extracted, provide enough information to infer contact forces. It is worth noting that GEM does not require prior knowledge of the grain-to-grain contact law and can be applied to assemblies of arbitrarily-shaped grains. Grain contours and centroids are obtained from digital images by means of segmentation algorithms. Typically, the Circular Hough Transform algorithm [84, 85] is used for circular grains and the Watershed Segmentation algorithm [86–88] for arbitrarily-shaped grains. Knowing the contour of each grain, contact point locations are deduced by computing the Euclidean distance between contour nodes of grains.

Measurement of grain displacements, rotations, and strains are extracted using 2D-Digital Image Correlation (DIC) [61, 62]. Digital Image Correlation is an optical tool based on digital image processing and numerical computing which provides full-field displacements and strains by comparing the gray intensity changes of the object surface before and after deformation. The DIC procedure consists of tracking the same pixels between reference and deformed images. To perform this tracking, a correlation window, or subset, is chosen and deformed until the pattern in the deformed image matches the pattern in the reference image as closely as possible. To determine an adequate subset size, a compromise between resolution and measurement error needs to be found. The error is evaluated by correlating two subsequent images of the specimen, without applying any deformation to it. The values of the resulting strain components (ϵ_{xx}, ϵ_{yy} and ϵ_{xy}) for different subset sizes are then compared in order to identify suitable configurations. The degree of similarity between the reference and deformed subsets is computed using a correlation coefficient and the best fit is achieved when the correlation coefficient reaches its maximum. The position of the deformed subset is determined and the in-plane displacement is obtained by calculating the difference between the position of each point in the reference subset and the position of the corresponding point in the deformed subset. The strain field is then computed by numerical differentiation of the displacement field. The 2D-DIC analysis presented in this paper was carried out with the software VIC-2D (Correlated Solutions Inc.) [89, 90].

A constitutive law is required to obtain average grain stresses $\bar{\boldsymbol{\sigma}}$ from average grain strain $\bar{\boldsymbol{\epsilon}}$. In this thesis, assuming a linear elastic material, we compute the average grain stresses $\bar{\boldsymbol{\sigma}}_p$ from the average grain strains $\bar{\boldsymbol{\epsilon}}_p$ using generalized Hooke's law such that, $\bar{\boldsymbol{\sigma}}_p = \mathbb{C} : \bar{\boldsymbol{\epsilon}}_p$, where $\mathbb{C}$ is the elastic stiffness of the grain.

3.3 Mathematical framework

The constrained optimization problem employed by GEM to infer contact forces from experimental measurements involves three sets of governing equations: momentum balance, a force-stress relationship, and constraint equations. Underlying the formulation of all governing equations is the assumption of point contact. This assumption is valid for many stiff particles of interest in granular physics, including, for instance, sands, powders, and many pharmaceuticals. In the case of more compliant particles, this approximation may remain accurate for moderate load levels.

Consider the p^{th} particle in a static granular material, interacting with other particles through N_c^p contact points labeled with index α (see Figure 3.2). Balance of forces and moments reads as follows:

$$\sum_{\alpha=1}^{N_c^p} \boldsymbol{f}^\alpha = \mathbf{0} \tag{3.1}$$

$$\sum_{\alpha=1}^{N_c^p} \boldsymbol{x}^\alpha \times \boldsymbol{f}^\alpha = \mathbf{0} \tag{3.2}$$

where, as show in Figure 3.2, $\boldsymbol{x}^\alpha$ is a vector which represents the position of the contact point α relative to a reference frame, $\boldsymbol{f}^\alpha$ is a force vector acting at α, and N_c^p is the total number of contact points for grain p.

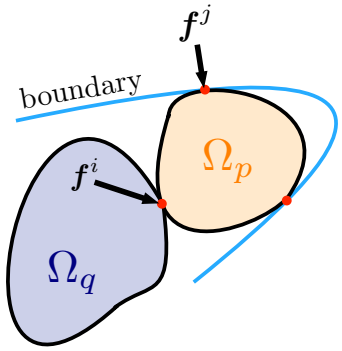

Figure 3.2: Illustration of particle-particle and particle-boundary contacts.

Equations (3.1) and (3.2) can be combined into a single matrix expression for an entire assembly of particles: $\boldsymbol{K}_{eq}\boldsymbol{f} = \mathbf{0}$. In two dimensions, the system takes the

form:

$$\begin{array}{c} \\ p \\ \\ q \\ \\ \end{array} \begin{array}{c} \begin{array}{ccccc} & & i & & j & \\ \end{array} \\ \begin{pmatrix} \ddots & \mathbf{0} & \cdots & \mathbf{0} & \cdots \\ \mathbf{0} & \boldsymbol{K}^i_{eq} & \mathbf{0} & \boldsymbol{K}^j_{eq} & \mathbf{0} \\ \vdots & \mathbf{0} & \ddots & \mathbf{0} & \vdots \\ \mathbf{0} & -\boldsymbol{K}^i_{eq} & \mathbf{0} & \mathbf{0} & \mathbf{0} \\ \vdots & \mathbf{0} & \vdots & \mathbf{0} & \ddots \end{pmatrix} \end{array} \begin{pmatrix} \vdots \\ \boldsymbol{f}^i \\ \vdots \\ \boldsymbol{f}^j \\ \vdots \end{pmatrix} = \begin{bmatrix} \vdots \\ \mathbf{0} \\ \vdots \\ \mathbf{0} \\ \vdots \end{bmatrix} \tag{3.3}$$

with

$$\boldsymbol{K}^i_{eq} = \begin{bmatrix} 1 & 0 \\ 0 & 1 \\ -x^i_2 & x^i_1 \end{bmatrix}; \quad \boldsymbol{f}^i = \begin{pmatrix} f^i_1 \\ f^i_2 \end{pmatrix} \tag{3.4}$$

where p and q represent particles, i and j represent particle-particle and particle-boundary contacts as shown in Figure 3.2. In general, $\boldsymbol{K}_{eq}$ will have $N_p\, d\,(d+1)/2$ rows and $N_c\, d$ columns where d is the dimension (e.g., $d = 2$ for 2D), N_p is the total number of particles in the assembly, and N_c is the total number of contact points in the assembly.

The average Cauchy stress for a particle in equilibrium under the action of discrete boundary forces can be derived by considering the volume averaged stress equation for a particle p:

$$\bar{\boldsymbol{\sigma}}^p = \frac{1}{\Omega_p} \int_{\Omega_p} \boldsymbol{\sigma}^{\boldsymbol{p}}\, \mathrm{d}v \tag{3.5}$$

where Ω_p indicates integration over the deformed volume (in 3D) or area (in 2D) of the particle p. By considering balance of linear momentum, the divergence theorem, and the symmetry of the Cauchy stress tensor, this expression takes the form (see [52] for more details):

$$\bar{\boldsymbol{\sigma}}^p = \frac{1}{\Omega_p} \sum_{\alpha=1}^{N^p_c} \mathrm{sym}(\boldsymbol{f}^\alpha \otimes \boldsymbol{x}^\alpha) \tag{3.6}$$

Equation (3.6) can be written in matrix form for an entire assembly of particles as

$\boldsymbol{K}_{st}\boldsymbol{f} = \boldsymbol{b}_{st}$. In two dimensions, the system takes the form:

$$
\begin{array}{c} \\ p \\ \\ q \\ \\ \end{array}
\begin{array}{c}
\begin{array}{ccccc} & & i & & j & \end{array} \\
\begin{pmatrix}
\ddots & \mathbf{0} & \cdots & \mathbf{0} & \cdots \\
\mathbf{0} & \boldsymbol{K}^i_{st} & \mathbf{0} & \boldsymbol{K}^j_{st} & \mathbf{0} \\
\vdots & \mathbf{0} & \ddots & \mathbf{0} & \vdots \\
\mathbf{0} & -\boldsymbol{K}^i_{st} & \mathbf{0} & \mathbf{0} & \mathbf{0} \\
\vdots & \mathbf{0} & \vdots & \mathbf{0} & \ddots
\end{pmatrix}
\end{array}
\begin{pmatrix} \vdots \\ \boldsymbol{f}^i \\ \vdots \\ \boldsymbol{f}^j \\ \vdots \end{pmatrix}
=
\begin{bmatrix} \vdots \\ \boldsymbol{b}^p_{st} \\ \vdots \\ \boldsymbol{b}^q_{st} \\ \vdots \end{bmatrix}
\tag{3.7}
$$

with

$$
\boldsymbol{K}^i_{st} = \begin{bmatrix} x^i_1 & 0 \\ 0 & x^i_2 \\ x^i_2 & x^i_1 \end{bmatrix}; \quad \boldsymbol{b}^p_{st} = \begin{bmatrix} \Omega_p \bar{\sigma}^p_{11} \\ \Omega_p \bar{\sigma}^p_{22} \\ 2\Omega_p \bar{\sigma}^p_{12} \end{bmatrix}
\tag{3.8}
$$

Similar to $\boldsymbol{K}_{eq}$, the matrix $\boldsymbol{K}_{st}$ has $N_p\ d\ (d+1)/2$ rows and $N_c\ d$ columns, where d is the dimension (e.g., $d = 2$ for 2D), N_p is the total number of particles in the assembly and N_c is the total number of contact points in the assembly.

Equations (3.1), (3.2), and (3.6) can be combined into single matrix equations for an entire assembly of grains that is given by:

$$
\boldsymbol{K}_{eq}\boldsymbol{f} = \mathbf{0} \tag{3.9a}
$$

$$
\boldsymbol{K}_{st}\boldsymbol{f} = \boldsymbol{b}_{st} \tag{3.9b}
$$

where $\boldsymbol{K}_{eq}$ encompasses position measurements in Equations (3.1) and (3.2), $\boldsymbol{K}_{st}$ encompasses position measurements in Equation (3.6) and $\boldsymbol{b}_{st}$ encompasses the experimental measurements on the right-hand side of Equation (3.6).

Finally, cohesion-less granular materials in equilibrium obey two additional laws: normal forces are repulsive and tangential forces are governed by a Coulomb type friction law. The latter constraint requires that $|f_t| \leq \mu |f_n|$, where f_t is a tangential force magnitude, f_n is a corresponding normal force magnitude, and μ is the inter-particle coefficient of friction. These two constraints can be written for any contact

point acting on the p^{th} particle as:

$$-\boldsymbol{e}^i \cdot \boldsymbol{f}^i \geq 0 \tag{3.10}$$

$$-(\boldsymbol{e}^i + \frac{1}{\mu}\boldsymbol{t}^i) \cdot \boldsymbol{f}^i \geq 0 \tag{3.11}$$

$$-(\boldsymbol{e}^i - \frac{1}{\mu}\boldsymbol{t}^i) \cdot \boldsymbol{f}^i \geq 0 \tag{3.12}$$

where $\boldsymbol{e}^i$ and $\boldsymbol{t}^i$ represent normal and tangential unit vectors at the contact point i for a particular particle Ω_p, as shown in Figure 3.3.

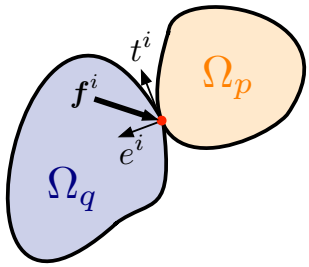

Figure 3.3: Unit vectors for contact i.

Equations (3.10), (3.11), and (3.12) can be combined into a single matrix expression for an entire assembly of particles: $\boldsymbol{B}\boldsymbol{f} \geq \boldsymbol{0}$. In 2D, the system takes the form:

$$\begin{array}{c} \\ i \\ \vdots \\ j \\ i \\ \vdots \\ j \\ i \\ \vdots \\ j \end{array}
\begin{array}{c}
\begin{array}{ccccc} i & i & & j & j \end{array} \\
\begin{pmatrix}
-e_1^i & -e_2^i & 0 & 0 & 0 \\
0 & 0 & \ddots & 0 & 0 \\
0 & 0 & 0 & -e_1^j & -e_2^j \\
-e_1^i - \frac{1}{\mu}t_1^i & -e_2^i - \frac{1}{\mu}t_2^i & 0 & 0 & 0 \\
0 & 0 & \ddots & 0 & 0 \\
0 & 0 & 0 & -e_1^j - \frac{1}{\mu}t_1^j & -e_2^j - \frac{1}{\mu}t_2^j \\
-e_1^i + \frac{1}{\mu}t_1^i & -e_2^i + \frac{1}{\mu}t_2^i & 0 & 0 & 0 \\
0 & 0 & \ddots & 0 & 0 \\
0 & 0 & 0 & -e_1^j + \frac{1}{\mu}t_1^j & -e_2^j + \frac{1}{\mu}t_2^j
\end{pmatrix}
\end{array}
\begin{pmatrix} f_1^i \\ f_2^i \\ \vdots \\ f_1^j \\ f_2^j \end{pmatrix} \geq \begin{bmatrix} 0 \\ \vdots \\ \vdots \\ \vdots \\ 0 \end{bmatrix} \tag{3.13}$$

where subscripts refer to vector components and superscripts refer to particular contact points. In general, $\boldsymbol{B} \in \mathbb{R}^{3N_c \times dN_c}$.

The mechanics of an assembly of contacting grains is fully governed by the three matrices given in Equations (3.9a), (3.9b), and (3.13). Every term in these equations,

except for the force vector $\boldsymbol{f}$, is experimentally extracted as explained in section 3.2. To find the force vector $\boldsymbol{f}$ that best fits the measured data, we combine equations (3.9a), (3.9b), and (3.13) to formulate a constrained optimization problem that can be expressed as:

$$\boldsymbol{f} = \underset{f}{\operatorname{argmin}}(\lambda||\boldsymbol{K}_{eq}\boldsymbol{f}||_2 + (1-\lambda)||\boldsymbol{K}_{st}\boldsymbol{f} - \boldsymbol{b}_{st}||_2) \tag{3.14a}$$

$$\text{subjected to: } \boldsymbol{B}\boldsymbol{f} \geq \boldsymbol{0} \tag{3.14b}$$

The previous multi-objective optimization problem is solved using CVX [91], a Matlab-based optimization solver. The parameter λ sets the relative weight between the equilibrium objective function $||\boldsymbol{K}_{eq}\boldsymbol{f}||_2$ and the stress objective function $||\boldsymbol{K}_{st}\boldsymbol{f} - \boldsymbol{b}_{st}||_2$. Due to the conflicting nature of the objective functions $||\boldsymbol{K}_{eq}\boldsymbol{f}||_2$ and $||\boldsymbol{K}_{st}\boldsymbol{f} - \boldsymbol{b}_{st}||_2$, no single optimal solution exists; instead, a set of trade-off solutions, known as Pareto optimal solutions, can be found [92]. The set of all Pareto optimal solutions forms a curve known as a Pareto front. The Pareto front represented in Figure 3.4 is obtained by solving equation (3.14) with many values of λ. A methodology which determine the *knee point* of the Pareto front is then used to systematically choose a single preferred solution [93]. At any such *knee point*, an improvement in one objective (e.g., equilibrium or stress) will result in a severe degradation in the other one. Once the knee point is identified, the set of forces $\boldsymbol{f}$ that best fits the measured data is obtained.

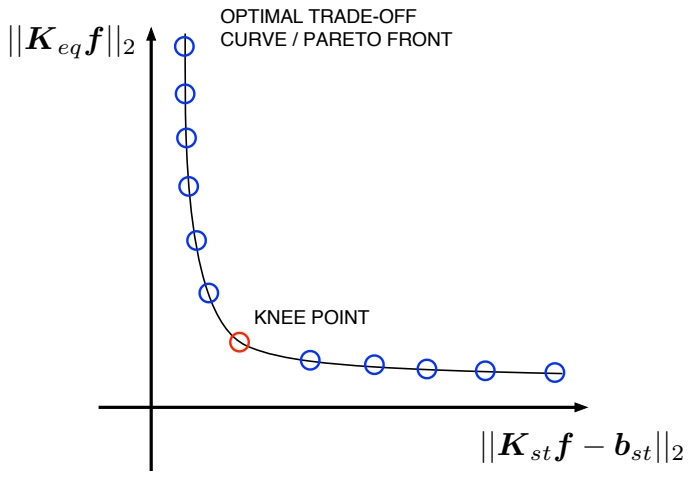

Figure 3.4: Schematic view of the Pareto front and knee point

To summarize, we describe the GEM algorithm in a pseudo-code format. Let i_p and i_α denote the storage indices for, respectively, the p-th particle and the α-th contact, for $\alpha \in \{1, \cdots, N_c\}$ and $p \in \{1, \cdots, N_p\}$. We recall that N_p is the total number of grains and N_c is the total number of contact.

Inputs: Position of contact points $\boldsymbol{x} = [\boldsymbol{x}^1, \boldsymbol{x}^2, \cdots, \boldsymbol{x}^{N_c}]^T$ where $\boldsymbol{x}^\alpha = \{x^\alpha, y^\alpha\}$
Average grain stress $\bar{\boldsymbol{\sigma}} = [\bar{\boldsymbol{\sigma}}^1, \bar{\boldsymbol{\sigma}}^2, \cdots, \bar{\boldsymbol{\sigma}}^{N_p}]^T$ where $\bar{\boldsymbol{\sigma}}^p = \{\bar{\sigma}^p_{xx}, \bar{\sigma}^p_{yy}, \bar{\sigma}^p_{xy}\}$
Surface of grains $\Omega = [\Omega_1, \Omega_2, \cdots, \Omega_{N_p}]^T$
Normal unit contact vector $\boldsymbol{e} = [\boldsymbol{e}^1, \boldsymbol{e}^2, \cdots, \boldsymbol{e}^{N_c}]^T$ where $\boldsymbol{e}^\alpha = \{e^\alpha_x, e^\alpha_y\}$
Tangential unit contact vector $\boldsymbol{t} = [\boldsymbol{t}^1, \boldsymbol{t}^2, \cdots, \boldsymbol{t}^{N_c}]^T$ where $\boldsymbol{t}^\alpha = \{t^\alpha_x, t^\alpha_y\}$
Inter-particle friction coefficient μ
Boundary of granular assembly Γ

Output: Force vector $\boldsymbol{f} = [\boldsymbol{f}^1, \boldsymbol{f}^2, \cdots, \boldsymbol{f}^{N_c}]^T$ where $\boldsymbol{f}^\alpha = \{f^\alpha_x, f^\alpha_y\}$

Algorithm 1 The Granular Element Method (GEM)

Initialize
Construct vector $\boldsymbol{b}_{st} = [\boldsymbol{b}_{st}^1, \boldsymbol{b}_{st}^2, \cdots, \boldsymbol{b}_{st}^{N_p}]^T$
for `p = 1 to` N_p **do**
    Compute $\boldsymbol{b}_{st}^p = \{\Omega_p \bar{\sigma}_{xx}^p, \Omega_p \bar{\sigma}_{yy}^p, 2\Omega_p \bar{\sigma}_{xy}^p\}$
    Assemble $\boldsymbol{b}_{st}(i_p) = \boldsymbol{b}_{st}^p$
end for
Construct matrices $\boldsymbol{K}_{eq}$, $\boldsymbol{K}_{st}$ and $\boldsymbol{B}$
for α `= 1 to` N_c **do**
    Identify master grain p
    Compute $\boldsymbol{K}_{eq}^{\alpha} = [\{1, 0\}, \{0, 1\}, \{y^{\alpha}, -x^{\alpha}\}]$
    Assemble $\boldsymbol{K}_{eq}(i_p, i_{\alpha}) = \boldsymbol{K}_{eq}^{\alpha}$
    Compute $\boldsymbol{K}_{st}^{\alpha} = [\{x^{\alpha}, 0\}, \{0, y^{\alpha}\}, \{x^{\alpha}, y^{\alpha}\}]$
    Assemble $\boldsymbol{K}_{st}(i_p, i_{\alpha}) = \boldsymbol{K}_{st}^{\alpha}$
    if $\alpha \notin \Gamma$ **then**
        Identify slave grain q
        Assemble $\boldsymbol{K}_{eq}(i_q, i_{\alpha}) = -\boldsymbol{K}_{eq}^{\alpha}$
        Assemble $\boldsymbol{K}_{st}(i_q, i_{\alpha}) = -\boldsymbol{K}_{st}^{\alpha}$
    end if
    Compute $\boldsymbol{B}_1(\alpha, i_{\alpha}) = [-e_x^{\alpha}, -e_y^{\alpha}]$
    Compute $\boldsymbol{B}_2(\alpha, i_{\alpha}) = [-e_x^{\alpha} - t_x^{\alpha}/\mu, -e_y^{\alpha} - t_y^{\alpha}/\mu]$
    Compute $\boldsymbol{B}_3(\alpha, i_{\alpha}) = [-e_x^{\alpha} + t_x^{\alpha}/\mu, -e_y^{\alpha} + t_y^{\alpha}/\mu]$
    Assemble $\boldsymbol{B} = [\boldsymbol{B}_1, \boldsymbol{B}_2, \boldsymbol{B}_3]^T$
end for
Solve optimization problem
for $\lambda \in [0, 1]$ **do**
    Minimize $(\lambda||\boldsymbol{K}_{eq}\boldsymbol{f}|| + (1-\lambda)||\boldsymbol{K}_{st}\boldsymbol{f} - \boldsymbol{b}_{st}||)$ with respect to $\boldsymbol{f}$ subjected to $\boldsymbol{B}\boldsymbol{f} \geq 0$
    Store $||\boldsymbol{K}_{eq}\boldsymbol{f}||, ||\boldsymbol{K}_{st}\boldsymbol{f} - \boldsymbol{b}_{st}||$ and $\boldsymbol{f}$
end for
Find the preferred solution $\boldsymbol{f}^*$ corresponding to the knee point of the $(||\boldsymbol{K}_{eq}\boldsymbol{f}||, ||\boldsymbol{K}_{st}\boldsymbol{f} - \boldsymbol{b}_{st}||)$ curve
Return $\boldsymbol{f} = \boldsymbol{f}^*$

3.4 Experimental validation and application of GEM

This section presents an example of GEM applied to a real experiment. The current experiment uses 2D-DIC to measure full-field particle strains from which stresses are deduced. Information about the location of contact points and particle shapes are obtained from digital images using segmentation algorithms. This data is then passed to the GEM algorithm, which reconstructs the force distribution. The results of this experiment showcase the applicability of GEM to real materials and its potential to be combined with advanced experimental techniques.

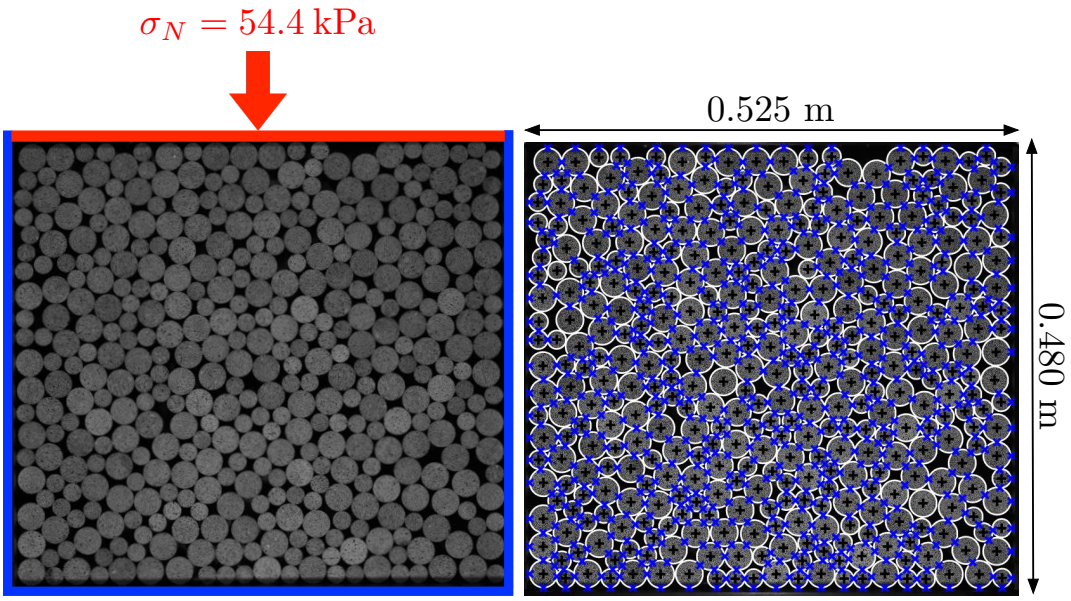

Figure 3.5: (a) Sample under macroscopic loading. Top face (red) was prescribed a vertical load of σ_N = -54.4 kPa using a smooth, rigid wall. Bottom and lateral faces (blue) were smooth, stationary walls. (b) Sample dimensions in meters. Results of segmentation process (white contours) and contact detection (blue crosses).

A uniaxial compression test is carried out on the apparatus described in Section 4.2. The specimen shown in Figure 3.5 was compressed with a $\sigma_N = -54.4$ kPa vertical load on the top wall, while the side walls were held rigid. The granular assembly used in this test was composed of 400 cylinders. Grain diameters were 20 mm and 30 mm and the grains out-of-plane length was 25 mm. The grain diameters correspond to, respectively, 116 pixels and 172 pixels on the 4864×3232 pixels digital images captured at each time step. We emphasize that discs were used due to the simplicity of their manufacturing process. However, as it will be shown in Section 5, experiments can be carried out on arbitrary-shaped grains since the force inference method (GEM) does not make any assumption about grain shape [52, 82]. The grains are made of polyurethane that has a Young's modulus E = 50 MPa, a Poisson's ratio ν of approximately 0.5, and an inter-particle friction coefficient μ = 0.6. For an optimal use of 2D-DIC, the top face of each cylinder is covered with suitable speckle patterns that are achieved by spraying black and white paints.

Segmentation algorithms were used to extract the material's fabric: grain contact points, centroids, and areas. Circular Hough transform [84, 85] was first performed to determine the grain contours. A simple algorithm based on measuring the

euclidean distance between centroids was then used to determine the position of the contact points. The results of this algorithm are shown in Figure 3.5b, where it can be seen that the 400 grains share a total of 791 contact points.

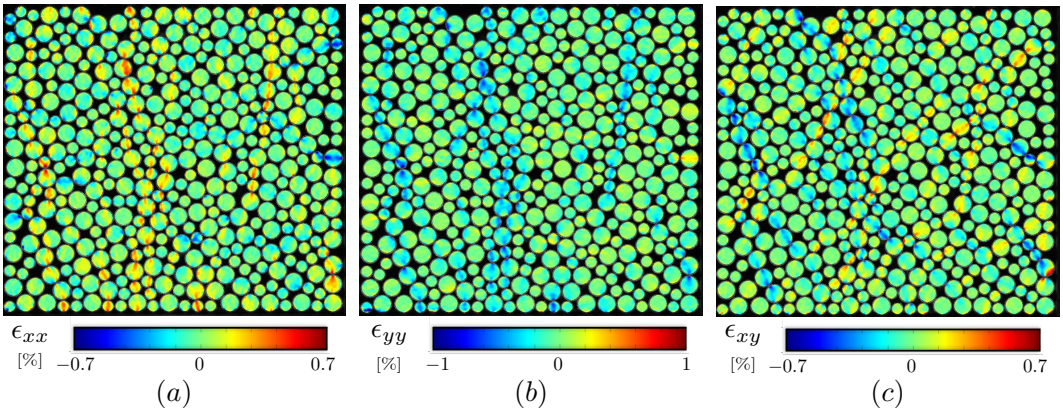

Figure 3.6: Full-field strain measurements obtained using DIC during a uniaxial compression test (σ_N = -54.4 kPa) (a). Strain component ϵ_{xx} (b). Strain component ϵ_{yy} (c). Strain component ϵ_{xy}.

The 2D-DIC technique [61, 62] is applied to the images to extract full-field displacement, strain and grain rotations. To perform this tracking, a correlation window (also called subset) of 15x15 pixels is chosen and a step size (i.e., the distance between neighboring calculation points) is set to 3 pixels. With a 15 × 15 pixels correlation window, a border of 7 pixels around the edge of the grains are not correlated. However, since the force inference method (GEM) takes the average grain stresses as input [52, 82], this data loss adjacent to the edges is not sufficient to compromise an accurate force calculation. Figure 3.6 shows the full-field strain distribution (ϵ_{xx}, ϵ_{yy} and ϵ_{xy}) obtained from 2D-DIC at the final load step where the granular assembly is subjected to a uniaxial compressive load of σ_N = -54.4 kPa (hanging mass of 160 lbs). The full-field stress distribution (σ_{xx}, σ_{yy} and σ_{xy}) is obtained by using the full-field strains in a linear elastic plane stress formulation. The corresponding principal stresses and are calculated at each pixel. Contour plot of difference of principal stresses are presented in Figure 3.7 for the final load step (σ_N = -54.4 kPa, hanging mass of 160 lbs). The stress contour distribution gives us a direct comparison with stresses measured with photoelasticity [30–33]. Indeed, the isochromatic pattern obtained when a birefringent material is placed under stress is directly proportional to the difference of principal stresses $\sigma_1 - \sigma_2$ [94]. It can be seen from Figure 3.6 and Figure 3.7a that DIC measurements provide a qualitative information of the force distribution in an opaque granular assembly. Given that the position of the contact

points and the average grain stresses are known, force inference is performed with GEM [52, 82] by solving the inverse problem given in Equation (3.14). The resulting contact forces for the uniaxial test are depicted in Figure 3.7b. Figure 3.7b shows that the force magnitude is consistent with the stress contour distribution and that force chains are clearly seen to develop. GEM provides a quantitative assessment of force network.

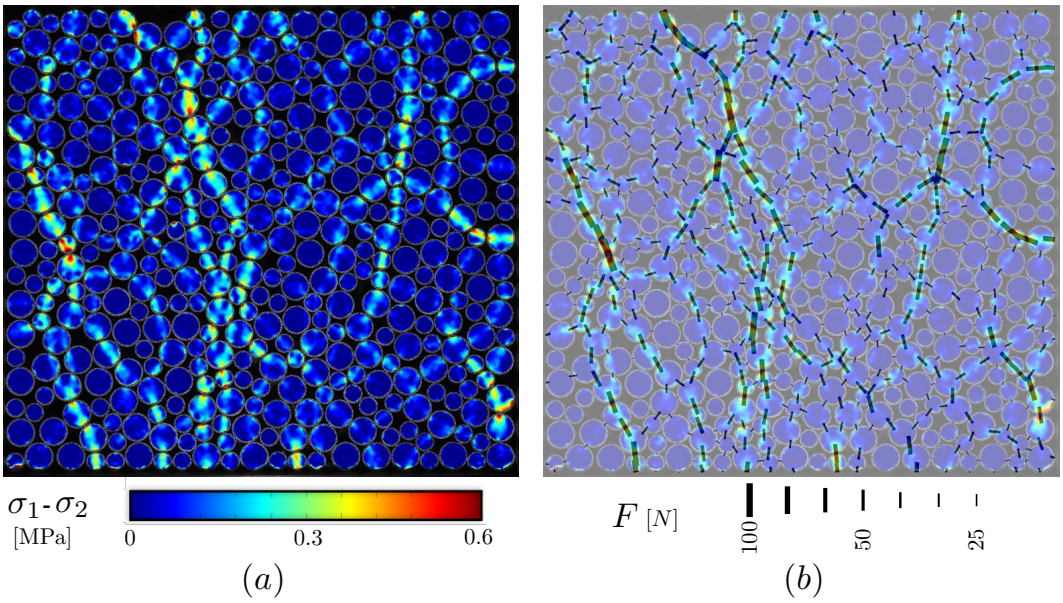

Figure 3.7: (a). Contour distribution of difference in principal stresses $\sigma_1 - \sigma_2$ (b). Contact force magnitudes f obtained with GEM superimposed on contour distribution of difference in principal stresses $\sigma_1 - \sigma_2$.

The average macroscopic stress in the array was also computed using the expression [95]:

$$\langle \boldsymbol{\sigma} \rangle = \frac{1}{\Omega} \sum_{\alpha=1}^{N_c} \text{sym}(\boldsymbol{f}^{\alpha} \otimes \boldsymbol{d}^{\alpha}) \tag{3.15}$$

where Ω is the volume of the assembly, N_c is the number of inter-particle contacts in the assembly, $\langle \boldsymbol{\sigma} \rangle$ is the macroscopic average stress, $\boldsymbol{f}^{\alpha}$ is the inter-particle contact force, and $\boldsymbol{d}^{\alpha}$ is the branch vector between particles. The resulting macroscopic stress was computed to be:

$$\langle \boldsymbol{\sigma} \rangle = \begin{bmatrix} -26.4 & -5.1 \\ -4.8 & -52.6 \end{bmatrix} \text{(kPa)} \tag{3.16}$$

where compressional stresses are negative. The $\langle \boldsymbol{\sigma} \rangle_{yy}$ component of this result corresponds well with the applied stress of $\sigma_N = -54.4\,\text{kPa}$, a motivational re-

sult considering that equation (3.15) is approximate since branch vectors between particles and walls were not included.

The result of this experiment underscores the power of GEM for inferring contact forces in real opaque materials. The experiment also illustrates the versatility of GEM: it is adaptable to any experimental technique able to furnish the required input.

3.5 Conclusion

The improved formulation of GEM presented in this chapter provides a powerful methodology for investigating contact forces in granular materials with unprecedented resolution. The first experimental example using GEM has been showcased to demonstrate that the method can and has been applied to real materials. The presentation of the mathematical framework illustrates its simplicity and versatility, and offers many possibilities of extending the framework to incorporate additional experimental measurements such as boundary forces. With progress in experimental imaging and intra-particle strain field extraction (e.g., [9, 96]), GEM will soon be able to extract contact forces in materials with smaller grains like sands, providing the first chance to validate many theories regarding force networks in natural granular media. GEM will also advance the boundaries of the micromechanical understanding of granular materials by offering a characterization tool for a new class of opaque complex assemblies.

Chapter 4

A NOVEL EXPERIMENTAL DEVICE FOR INVESTIGATING THE MULTISCALE BEHAVIOR OF GRANULAR MATERIALS UNDER SHEAR

4.1 Introduction

The macro-mechanical response of granular materials subjected to shear conditions has been extensively investigated by means of laboratory testing such as triaxial tests [97, 98] and direct shear tests [99, 100]. It is well-known that dense samples exhibit a peak in shear stress followed by a strain softening behavior, whereas in loose samples no peak is observed. However, at large shear deformation, both dense and loose samples show a tendency to stabilize around an asymptotic shear stress value that is uniquely related to the normal stress and void ratio. In terms of volumetric deformations, dense samples initially contract and later dilate while loose samples only contract. For large shear strain values, the volumetric deformation of both systems reaches a constant value. This equilibrium state where no further changes in volume or stress state occur with increased shear deformation is conceptually defined as the critical state of a granular material. The critical state concept, first introduced by Casagrande [101] and considerably developed by Roscoe et al. [2], has provided a unifying approach to the fundamental understanding of the mechanical behavior of granular materials. The existence of a critical state has furnished a basis for the development of continuum constitutive models within the framework of plasticity theory [3–5]. Such models, known as the critical state soil mechanics framework, constitute one of the keystones of soil mechanics and have allowed practitioners to solve complex geomechanical engineering problems.

However, this modelling paradigm still has many limitations. Critical state plasticity models have been developed under the assumption that granular materials deform as isotropic continua despite their discrete nature. Moreover, existing models have been derived from macroscopic observations obtained in the laboratory. Therefore, they heavily rely on the calibration of several state variables, which often lack a clear physical meaning. Phenomenological approaches also influence the predictive capabilities of most constitutive models when applied outside of their predetermined realm. As a consequence, there is currently a need to develop more physic-based

constitutive models to better understand and accurately describe the continuum behavior of granular materials by embedding micromechanics. Significant efforts have been made in constructing multiscale analysis that provide a link between grain and continuum scale. Some of the most prominent examples include the stress-dilatancy theory, originally developed by Rowe [20], the stress-induced anisotropy [33, 102, 103], and the stress-strain-fabric relationship [15, 104].

Many of these studies have been conducted using the discrete element method (DEM) [14] that has emerged as an important numerical technique to access grain-scale information such as contact forces and kinematics. In the recent past, DEM has been employed to micromechanically study the shear behavior of granular materials [18, 105–107]. Nonetheless, DEM still has many limitations: it has a high computational cost, is generally constrained to simple grain shapes, and remains mainly qualitative.

Meanwhile, experimental testing remains an irreplaceable approach for investigating the fundamental response of granular materials. Shear tests performed on quasi-2D granular assemblies have proved their ability to provide key insights into the micromechanics of granular materials [11, 38, 108–110]. Such progress made in the field of experimental geomechanics are intimately linked to the development of grain-scale characterization techniques. In recent years, Digital Image Correlation (DIC) has been widely used to capture kinematics in granular assemblies [43, 44, 111, 112]. By defining the best mapping function that relates two images, DIC provides full-field displacements, strains, and rotation [61, 62]. Force inference has been made possible by use of photoelasticity in assembly of birefringent disks [30, 33] and recently in assembly of opaque, real granular materials in 2D [52, 82, 83] and 3D [10] by means of the Granular Element Method (GEM), as described in Chapter 3.

This chapter presents an experimental capability that furnishes unique data on the mechanics of granular materials at different scales including continuum measures of stresses and strains and discrete measures of grain kinematics and contact forces. A key aspect of this experimental method is a novel apparatus allowing shear deformation at constant normal pressure of a 2D analogue granular assembly. At the grain scale, kinematics are extracted using DIC and normal and tangential contact forces are inferred with GEM, provided that average grain strains and contact point locations are known. We show that macroscopic results of stresses and strains reproduce typical features of the shear response of dense granular materials. To

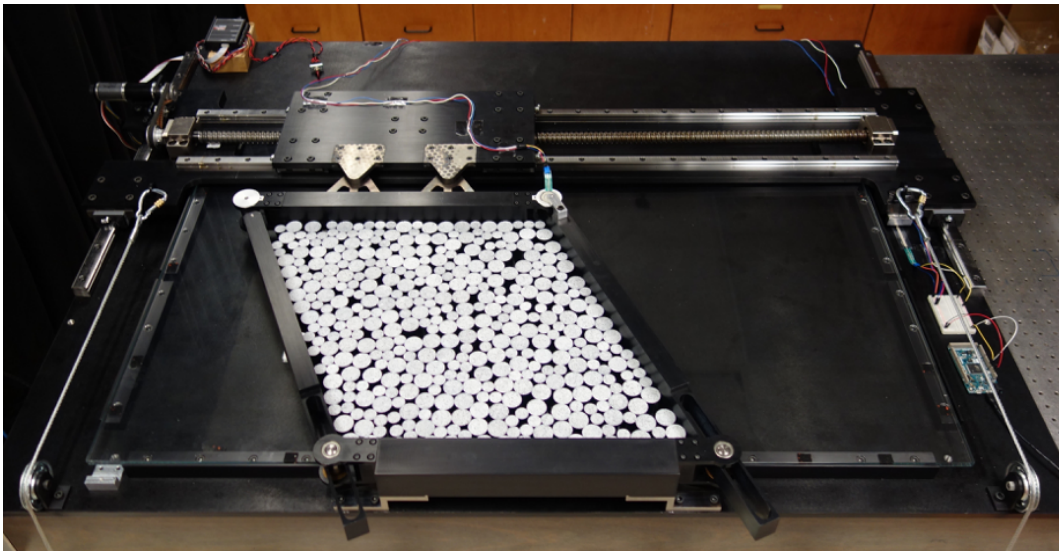

Figure 4.1: Picture of the experimental setup

provide a validation process of the experimental method, we performed a uniaxial compression. This simpler loading condition gives us a direct comparison between applied load and results of normal stress computed from grain-scale quantities. In this study, we aim to improve our knowledge of the multiscale behavior of granular materials, which is essential for developing more physics-based constitutive models and for comparing laboratory tests with numerical simulations such as those performed with DEM.

For completeness, the chapter is organized as follows. First, Section 4.2 presents the experimental setup and experimental procedure. Section 4.3 showcases the validation process of the experimental method. Finally, Section 4.5 offers concluding remarks.

4.2 Experimental setup

Description of the apparatus

We have designed and built a novel experimental device capable of reproducing (quasi-static) simple shear conditions over large deformation on a two-dimensional analogue granular assembly. A general view of our apparatus is given in Figures 4.2 and 4.1. In particular, Figure 4.2 shows an exploded-view drawing of the device where the three main elements are showcased: (1) the support structure, (2) the shear cell, and (3) the linear actuator system.

The support structure is made of a 1630 mm x 1270 mm x 16 mm aluminum

mounting plate and is directly placed onto a stationary steel table. Z-shaped members supporting the shear cell, L-shaped members supporting the glass plate, pulleys and y-axis linear guide rails are screwed to the aluminum plate. The shear cell consists of a horizontal deformable parallelogram (ABCD) that can undergo shear strain and normal strain in the y-direction (tilting and elongation of faces BC and AD). The points A and B are fixed to the Z-shaped members, which themselves are fixed to the support structure. The sides AB and CD are solid members that always remain horizontal and of constant length L_x = 525 mm while the lateral sides (BC and AD) consist of slotted members of variable length L_y. At the corners of the parallelogram ABCD, bearing arrangements mounted on rotary shafts allow the sides AD and BC to rotate at a constant angular velocity about the point A and the point B respectively. The shear angle γ between the vertical and the sides AD and BC can be positive or negative, allowing application of cyclic shear. The face CD of the shear cell remains parallel to the face AB and is mounted to the linear actuator system using bolted connections and a connector plate.

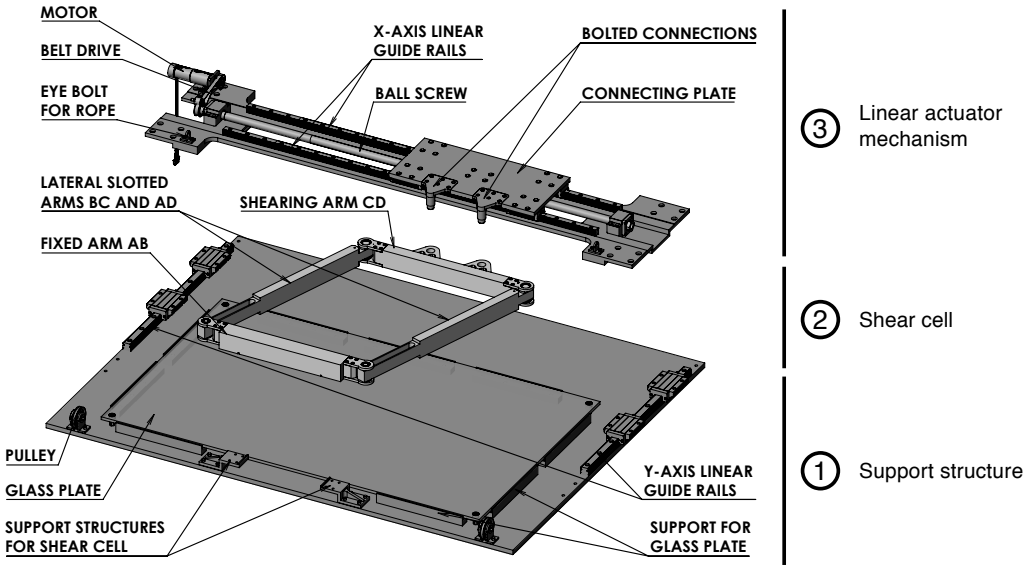

Figure 4.2: Exploded view drawing of the experimental shear apparatus

The linear actuator system is composed of a brushless DC electric motor (MAXON Motor), belt drive, linear guide rails positioned in the x-direction, and a ball screw, mounted onto an aluminum x-drive plate. A linear motion in the x-direction is

generated at the connector plate when the ball screw is rotated. This linear motion is transferred to the side CD of the shear cell and therefore provides the shear mechanism. Kinematic control of the shear mechanism is achieved by direct command of the speed of the DC motor using a speed controller (MAXON Motor) in closed loop. Thus, during a test, the velocity of the side CD and the shear rate are kept constant. Furthermore, as shown in Figures 4.2 and 4.1, the linear actuator system is screwed on two y-axis linear guide rails fixed to the mounting plate. The y-axis linear guide mechanism enables movement of the linear actuator system in the y-direction and thus allows the faces BC and AD of the shear cell to elongate (or shorten). A constant normal stress σ_N is applied to the face CD of the shear cell and transmitted to the granular assembly using two pulley systems. On each side of the mounting plate, a hanging mass is suspended over a pulley while the other end of the rope is attached to the linear actuator system. Finally, the granular assembly stands on a glass plate and is tracked by an optical imaging system (Allied Vision Prosilica GT4907 15.7 Megapixel CCD camera attached to a Nikkor AF 105mm f/2.8 lens) that sits at 1.6 m above the apparatus. Image sequences are typically acquired at a frame rate of 7 images per second.

Measurements

Figure 4.3 displays the general state of deformation of the shear cell subjected to a prescribed tilting angle γ and external load σ_N. The angle γ between the vertical and the sides AD or BC and the length in the y-direction $L_y = L_{y0} + \Delta L_y$ constitute the two degrees of freedom that define the configuration of the shear cell.

Figure 4.3c displays the general state of deformation of the shear cell subjected to a prescribed tilting angle γ and external load σ_N. The angle γ between the vertical and the sides AD or BC and the length in the y-direction $L_y = L_{y0} + \Delta L_y$ constitute the two degrees of freedom that define the configuration of the shear cell. As illustrated in Figure 4.3c, the length L_{y0} corresponds to the length of the sides AD and BC in the initial configuration (dashed lines) where the shear cell is a rectangle ($\gamma = 0$) and the length ΔL_y is the change in length in the y-direction. Measurements of the angle γ and the length L_y are performed using image processing. The limits on the dimensions of the shear cell are:

$$-35^\circ < \gamma < 35^\circ$$

$$450\text{mm} < L_y < 630\text{mm}$$

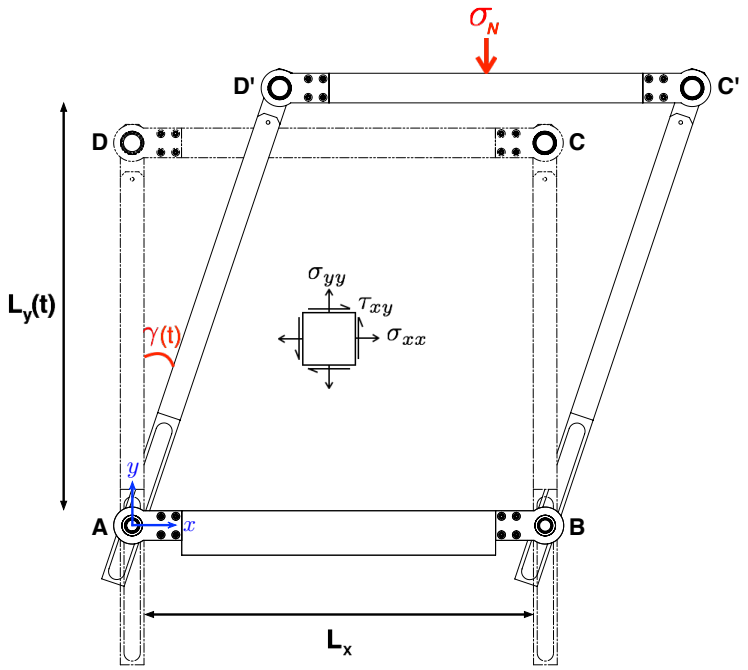

Figure 4.3: Schematic depicting the state of deformation and imposed boundary conditions on the shear cell.

Given that the length in the x-direction is constant (L_x = 525 mm), the component ϵ_{xx} of the strain tensor is equal to zero. Therefore, the macroscopic strain state is given by the following tensor:

$$\boldsymbol{\epsilon} = \begin{bmatrix} 0 & \epsilon_{xy} \\ \epsilon_{xy} & \epsilon_{yy} \end{bmatrix}$$

where the normal strain $\epsilon_{yy} = \Delta L_y / L_y$ and the shear strain $\epsilon_{xy} = \tan\gamma/2$. Owing to the precise kinematic control of the shear mechanism, the macroscopic strain state is known at all time. The volumetric strain is defined as $\epsilon_V = \mathrm{tr}(\boldsymbol{\epsilon}) = \epsilon_{yy}$. Simple shear tests are performed in quasi-static conditions with a shear rate $\dot{\gamma} = 0.12\ ^\circ/\mathrm{s}$. In two dimensions, the macroscopic stress state in the granular assembly is defined by the following tensor (see Figure 4.3):

$$\boldsymbol{\sigma} = \begin{bmatrix} \sigma_{xx} & \tau_{xy} \\ \tau_{xy} & \sigma_{yy} \end{bmatrix}$$

Material

We perform experiments on a two-dimensional analogue opaque granular assembly composed of 400 cylinders of height of 25 mm and of two different diameters, d_1 = 20 mm and d_2 = 30 mm. The grain diameters correspond to, respectively, 116 pixels and 172 pixels on the 4864×3232 pixels digital images captured at each time step. We emphasize that discs were used due to the simplicity of their manufacturing process. However, experiments can be carried out on arbitrary-shaped grains since the force inference method (GEM) does not make any assumption about grain shape [52, 82]. The grains are made of polyurethane that has a Young's modulus E = 50 MPa, a Poisson's ratio ν of approximately 0.5, and an inter-particle friction coefficient $\mu = 0.6$. For an optimal use of 2D-DIC, the top face of each cylinder is covered with suitable speckle patterns that are achieved by spraying black and white paints. Moreover, in order to minimize side and end friction between shear cell and the granular assembly, PTFE dry lubricant is sprayed onto the aluminum members of the shear cell. We point out that, since the shear apparatus lays horizontally, the assembly preparation is not under gravity, which does not influence the grain orientation and the force distributions.

4.3 Experimental method validation

To investigate the validity of the experimental capability presented in this paper, we performed a simple uniaxial compression test. In Section 4.3, we compare the results of macroscopic normal stress measured from the applied loads and the normal stress computed from grain-scale quantities, i.e., average grain stresses and contact forces. In Section 4.3, the contact forces inferred from GEM are used as input to compute an analytical stress contour distribution of $\sigma_1 - \sigma_2$ that is directly compared with measured 2D-DIC results.

Average macroscopic normal stress

A uniaxial compression test is carried out on the apparatus described in Section 4.2. In this test, the shear cell remains rectangular, such that the sides BC and AD can only elongate or shorten. It follows that the shear angle γ and the only non-zero component of the macroscopic strain tensor is $\epsilon_{yy} = \Delta L_y / L_y$. A normal stress σ_N is gradually applied to the granular assembly by linearly increasing the mass hanging over the pulley. The granular assembly is initially confined with a 20 lbs hanging mass, equal to an initial normal stress σ_N^0 = -6.8 kPa. At each load step, a 10 lbs weight is added which corresponds to a normal stress increment of $\Delta\, \sigma_N$ = -3.4

kPa. Sequence of images is collected with the image acquisition system detailed in Section 4.2 during the uniaxial compression test. Captured images are processed with image processing algorithm (i.e., Circular Hough Transform [84]) that perform circle detections from which the contact point locations are determined.

The 2D-DIC technique [61, 62] is applied to the images to extract full-field displacement, strain and grain rotations. The full-field stress distribution (σ_{xx}, σ_{yy} and σ_{xy}) is obtained by using the full-field strains in a linear elastic plane stress formulation. Given that the position of the contact points and the average grain stress are known, force inference is performed with GEM [52, 82]. The macroscopic stress response of the granular assembly subjected to external compressive loads is studied by incorporating grain-scale experimental information in two different ways.

A first approach consists of computing the average Cauchy stress tensor $\bar{\boldsymbol{\sigma}}$ by simply taking the arithmetic mean of the average grain stresses $\bar{\boldsymbol{\sigma}}^p$, such that:

$$\bar{\boldsymbol{\sigma}} = \frac{1}{N_p} \sum_{p=1}^{N_p} \bar{\boldsymbol{\sigma}}^p \tag{4.1}$$

where N_p is the total number of grains. The average grain stresses $\bar{\boldsymbol{\sigma}}^p$ is obtained from average grain strains $\bar{\boldsymbol{\epsilon}}^p$ via $\bar{\boldsymbol{\sigma}}^p = \mathbb{C} : \bar{\boldsymbol{\epsilon}}^p$. Equation (4.1) links the DIC grain measurements with the macroscopic stress tensor $\bar{\boldsymbol{\sigma}}$. An alternative approach is to derive an expression for the average Cauchy stress tensor $\bar{\boldsymbol{\sigma}}$ in terms of fabric and contact forces and has been presented by Christoffersen et al [95]:

$$\bar{\boldsymbol{\sigma}} = \frac{1}{\Omega} \sum_{\alpha=1}^{N_c} \mathrm{sym}(\boldsymbol{f}^\alpha \otimes \boldsymbol{d}^\alpha) \tag{4.2}$$

where N_c is the total number of contact points, Ω is the total volume of the granular assembly, $\boldsymbol{f}^\alpha$ is the contact force, and $\boldsymbol{d}^\alpha$ is the branch vector at the contact α. The previous expression provides a relationship between the macroscopic stress tensor and the distribution of contact forces inferred with GEM. In Fig. 4.4, we present results of average macroscopic stress in the y-direction $\bar{\sigma}_{yy}$ for the uniaxial compression test obtained from Equation (4.1) (blue dots) and Equation (4.2) (red plus sign) that are compared with the values of applied normal stress σ_N (black cross). Additionally, the relative error (in percent) between the applied normal stress σ_N and the measured average macroscopic stress $\bar{\sigma}_{yy}$ is presented in Fig. 4.4b. Potential error sources are versatile and include errors inherent to the optical measurement

system, the mechanical device, and the material property measurements, as well as intrinsic uncertainties of the DIC and GEM algorithms. Fig. 4.4b demonstrates that the relative error remains below ±15% for all load steps and that measurements obtained from DIC (Equation (4.1)) does not yield more accurate results than those obtained from the micromechanics (Equation (4.2)). This comparison indicates that there is an excellent agreement between the macroscopic applied stress and stress measurements obtained from grain quantities. In other words, the stress state evaluated inside the granular assembly can reliably represent the stress measured at the boundary. These results give a direct link between macroscopic stress and evolution of fabric and contact forces and, therefore, between micro and macro scales.

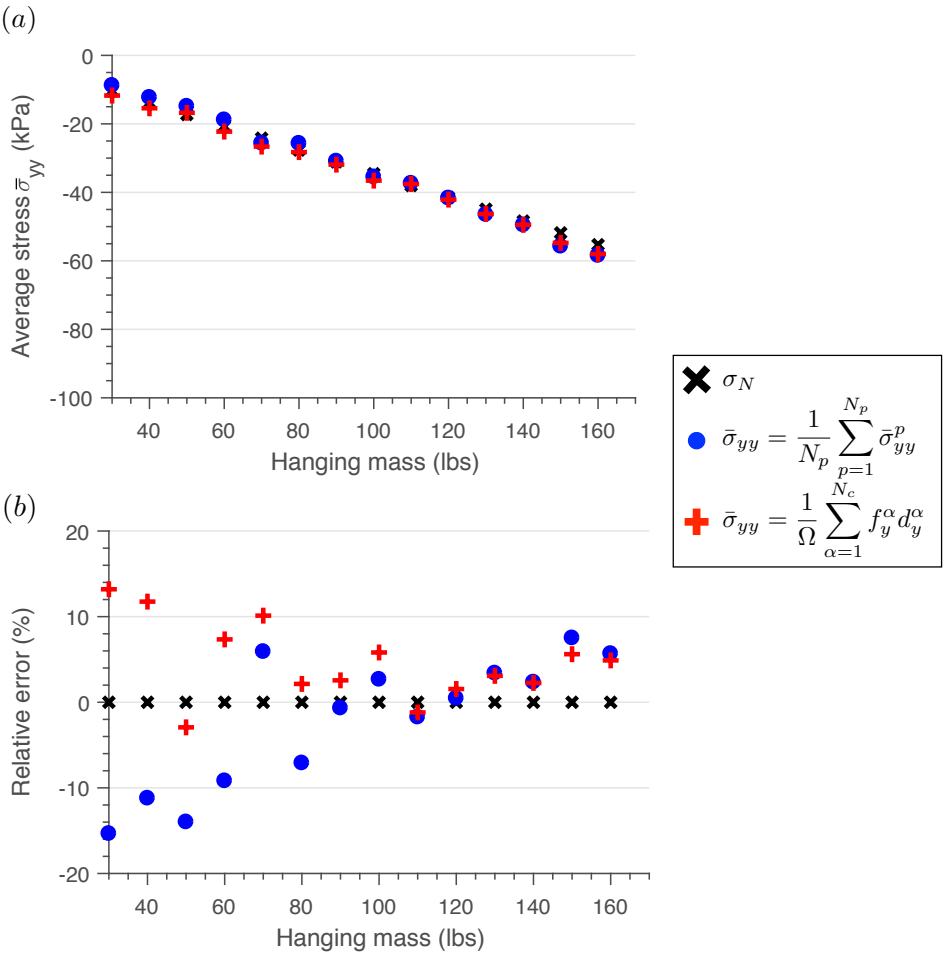

Figure 4.4: (a). Comparison of applied normal stress σ_N with macroscopic average stress $\bar{\sigma}_{yy}$ inferred from DIC measurements and GEM results. (b). Relative error (in percent) between applied normal stress σ_N (black cross) and the measurements of macroscopic average stress $\bar{\sigma}_{yy}$ obtained from Equations (4.1) (blue dots) and (4.2) (red plus sign).

Analytical stress contour distribution

By modeling the grains in the granular assembly as circular disks under in-plane loading, the stress distribution can be derived from an analytical solution based on the classical elasticity theory [31, 32, 113]. Analytical solution of stresses within a disk taken together with stress contour distribution visualized using photoelasticity techniques have been previously used to infer contact forces in birefringent granular material [30, 33, 34]. Grains used with photoelasticity in [33, 34] are less stiff (Young's modulus E = 5 MPa) than the grains tested in this work (E = 50 MPa). However, both force inference methods, photoelasticity and GEM, can be used with materials of various stiffness as long as the optical imaging system has a sufficient spatial resolution to accurately detect deformation.

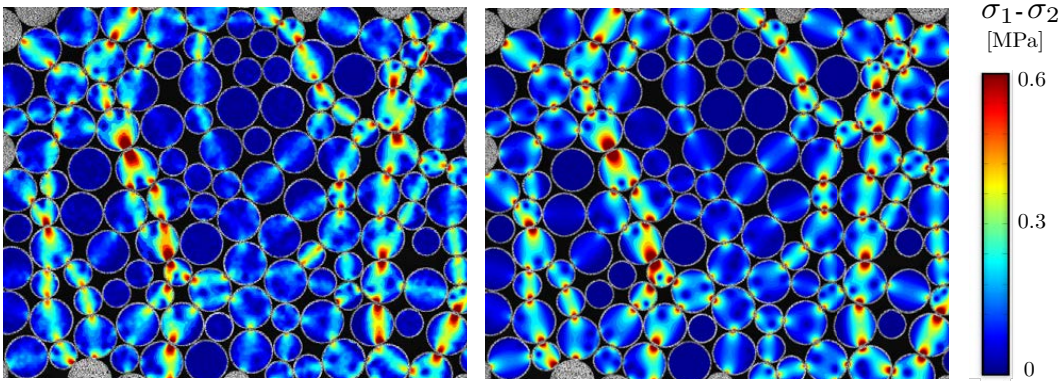

Figure 4.5: Contour distribution of difference in principal stresses $\sigma_1 - \sigma_2$ (a). obtained from 2D-DIC (b). derived from analytical solutions.

A detailed derivation of the analytical solution for a circular disk loaded by oblique concentrated forces at its boundary can be found in [114]. Hence, given the closed-form solution and knowing the value of the applied forces and the geometrical arrangement of the assembly (position of contact points), the analytical stress contour distribution within a disk is completely known. In this section, aiming to further validate our experimental procedure, we take the contact forces obtained from GEM as input to the analytical solution. In Fig. 4.5, the stress distribution derived from analytical formulations is compared with laboratory test results obtained from 2D-DIC where a uniaxial compression of -85 kPa is applied to the granular assembly. It can be seen from Figure 4.5 that there is an excellent correlation between the patterns of principal stress contours as plotted from the analytical solutions and the contours observed with 2D-DIC. This grain to grain comparison gives us an indication of the

accuracy of the magnitude and direction of the contact forces obtained with GEM.

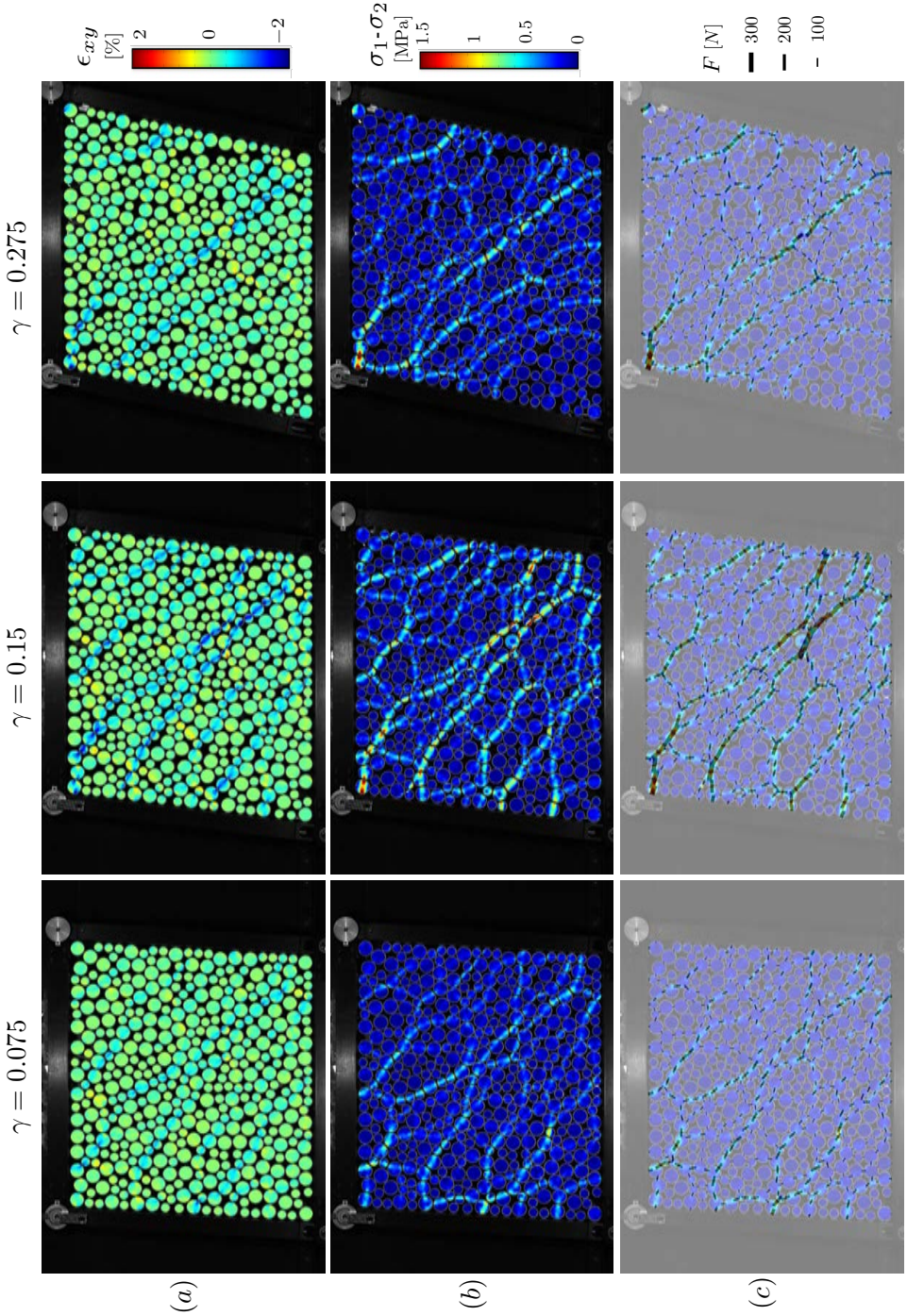

Figure 4.6: Contour distribution of DIC measurements and GEM results for shear test (σ_N = -28.5 kPa) at $\gamma = 0.075$, 0.15 and 0.275 (a). Strain field ϵ_{xy} (b). Difference of principal stresses $\sigma_1 - \sigma_2$ (c). Contact forces inferred with GEM superimposed on difference of principal stresses $\sigma_1 - \sigma_2$.

4.4 Micro- to macroscopic response of granular materials under shear

Simple shear tests are carried out in order to characterize the micro- to macroscopic response of the granular assembly under shear. Each simple shear test begins by applying a constant normal stress σ_N to the granular assembly. We present here results of shear tests performed with three three different values of σ_N: -14.25 KPa, -28.5 kPa and -42.75 kPa. The granular assembly is then sheared at a shear rate $\dot{\gamma} = 0.12\ ^\circ/\text{s}$. As in the uniaxial compression test, DIC measurements are performed to extract strain fields from which stress fields is deduced. MATLAB's image processing toolbox is used to determined grain positions and contact locations for each acquired image, so that the fabric evolution within the assembly is known at each time step. The contact forces are obtained by solving the GEM constrained optimization problem [52, 82]. Fig. 4.6 presents snapshots of the DIC results and contact forces distribution of the shear test performed at σ_N = -28.5 kPa for three different values of shear angle (γ = 0.075, 0.15 and 0.275). In Fig. 4.6, it can be seen that different force chain patterns form at different shear strain.

The macroscopic behavior of the granular assembly under shear is then investigated. First, macroscopic shear stress τ_{xy} is computed using Equation (4.2) given the branch vector and contact force distributions. The results of such calculation for σ_N = -14.25 KPa, -28.5 kPa and -42.75 kPa as a function of shear strain are shown in Fig. 4.7a. For all σ_N values, the granular material exhibits a linear elastic behavior followed by a peak in shear stress and subsequent strain softening. The observed stress-strain behavior is characteristic of a dense assembly subjected to shear deformation. In Fig. 4.7, vertical dashed lines indicate four distinct states of the shear behavior: (1) initial state (γ = 0); (2) linear elastic state (γ = 0.075); (3) peak state (γ = 0.15); and (4) critical state (γ = 0.275). It is worth noting that Fig. 4.6 shows snapshots of the granular assembly in linear elastic state (γ = 0.075), peak state (γ = 0.15) and critical state (γ = 0.275). In contrary to traditional laboratory experiments (such as triaxial and direct shear tests), our experimental procedure does not rely on boundary measurements of macroscopic stress obtained from load cells, which are typically used to study the constitutive behavior of granular materials [3–5]. As showcased by Equation (4.2), micromechanical quantities involving branch vectors and contact forces are used as input to compute the macroscopic stresses. Such data incorporating micromechanics are generally not available in 3D experiments in which stress measurements are restricted to measurements at the boundary of the granular assembly. Volumetric versus shear strain curves obtained in experiments for three different value of applied normal stress σ_N are plotted in Fig. 4.7b. In

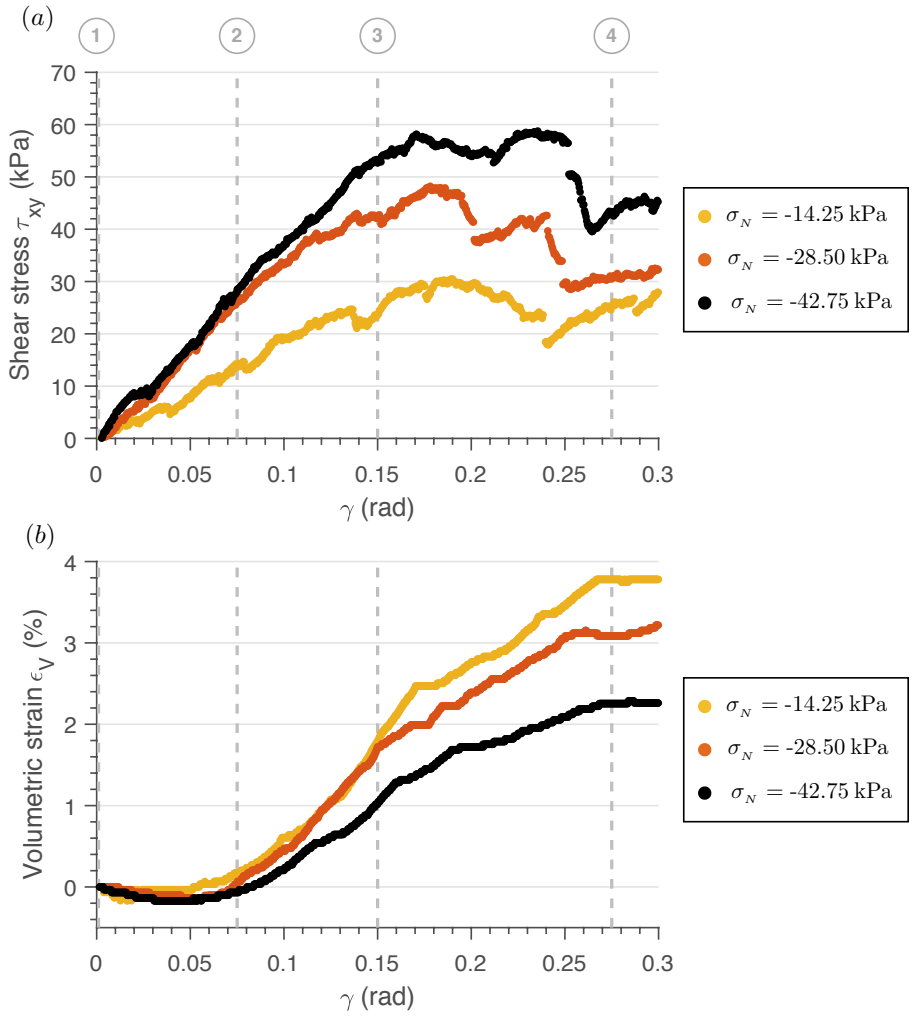

Figure 4.7: Macroscopic behavior of the granular sample subjected to shear (a). Shear stress τ_{xy} and (b). volumetric strain ϵ_V as a function of shear strain γ for applied normal stress σ_N = -14.25 KPa, -28.5 kPa and -42.75 kPa. Dashed vertical lines highlight four distinct states of the shear behavior: (1) initial state (γ = 0); (2) linear elastic state (γ = 0.075); (3) peak state (γ = 0.15); and (4) critical state (γ = 0.275).

Fig. 4.7b, we observe, once again, a typical behavior of a dense sample where the granular assembly initially contracts and then expands (dilates) until it reaches a constant volume at large shear deformation. The state in which the samples undergo large shear deformations without further changes in shear stress and volumetric strain corresponds to the critical state of the material. These results establish a link between grain-scale information, such as branch vectors and contact forces, and macroscopic laboratory observations.

The stress state of the granular assembly can also be visualized by looking at the

magnitude of the normal stress $\sigma_A = \hat{\boldsymbol{n}}_A \cdot \bar{\boldsymbol{\sigma}} \cdot \hat{\boldsymbol{n}}_A$ acting on a plane of orientation θ, defined by the unit vector $\hat{\boldsymbol{n}}_A = (\cos\theta, \sin\theta)$. Starting from Equation (Eq:Christofferson), the magnitude of normal stress σ_A can be expressed in terms of the micromechanics as follows:

$$\sigma_A = \frac{1}{\Omega} \sum_{\alpha=1}^{N_c} f_A^\alpha d_A^\alpha \tag{4.3}$$

where f_A^α and d_A^α are the scalar projections of, respectively, the force vector and the branch vector at the contact α onto the unit vector $\hat{\boldsymbol{n}}_A$, i.e., $f_A^\alpha = \boldsymbol{f}^\alpha \cdot \hat{\boldsymbol{n}}_A$ and $d_A^\alpha = \boldsymbol{d}^\alpha \cdot \hat{\boldsymbol{n}}_A$.

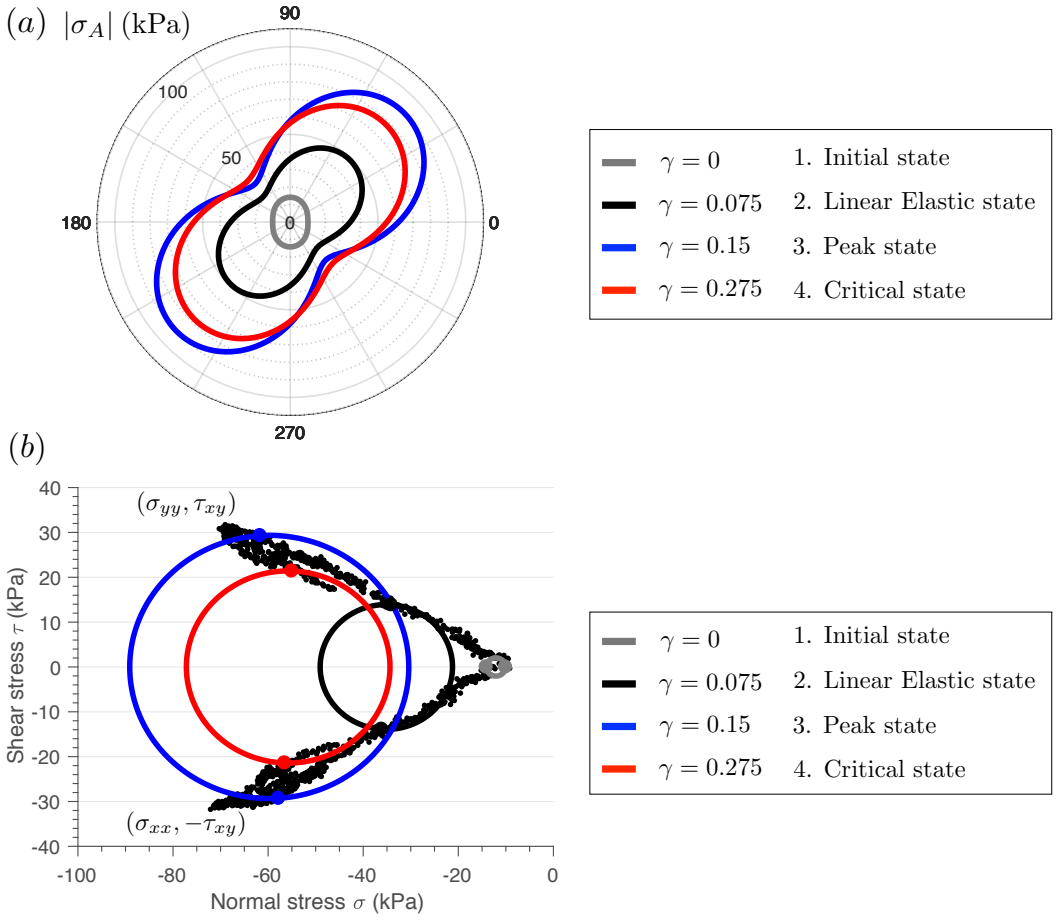

Figure 4.8: (a). Polar distribution of normal stress σ_A in kPa for shear test (σ_N = -14.25 kPa) at γ = 0, 0.075, 0.15 and 0.275. σ_A is computed from grain-scale data (force and branch vectors) using Equation (4.3). (b). Evolution of stress states (σ_{yy},τ_{xy}) and (σ_{xx},$-\tau_{xy}$) in kPa on a Mohr diagram (normal stress σ - shear stress τ plane). Mohr circles at γ = 0, 0.075, 0.15 and 0.275.

The polar representation of the normal stress for the shear test performed at σ_N = -14.25 kPa is shown in Fig. 4.8a. For each value of the angle $\theta \in [0, 2\pi]$, the magnitude of the normal stress $\sigma_A(\theta)$ is computed from the grain-scale quantities, i.e., the force vectors $\boldsymbol{f}^\alpha$ and the branch vectors $\boldsymbol{d}^\alpha$, according to Equation (4.3). In this figure, σ_A is plotted for different values of shear angle γ that correspond to distinct states of the shear behavior: initial state (γ = 0, gray curve), linear elastic state (γ = 0.075, black curve), peak state (γ = 0.15, blue curve) and critical state (γ = 0.275, red curve). The polar representation of the normal stress σ_A given in Fig. 4.8a enables a clear visualization of the evolution of principal stress values (σ_1 and σ_2) and principal stress orientation, defined as the angle θ_p between the vertical axis and the major principal stress σ_1 axis. In the initial state (γ = 0), where the granular sample is subjected to uniaxial compression with σ_N = -14.25 kPa, we report that $\sigma_1 \approx \sigma_N$ and that the principal stress is oriented towards the vertical axis (direction of loading), such that θ_p = 0. As the granular sample is sheared, the maximum principal stress value σ_1 increases until the peak and slightly decreases at critical state whereas the minimum principal stress value σ_2 only increases. Concurrently, as qualitatively reported in [115, 116], Fig. 4.8a reveals that the principal stresses rotate clockwise (increase of θ_p) during shear. Fig. 4.8b complements Fig. 4.8a as it depicts the evolution of the stress state (σ_{yy},τ_{xy}) and (σ_{xx},$-\tau_{xy}$) obtained from micromechanical quantities using Equation (4.2) on a Mohr diagram (normal stress σ - shear stress τ plane). In this figure, stress states (colored circle markers) for the four distinct states (initial, linear elastic, peak, and critical states) are highlighted and the corresponding Mohr circles are plotted. The stress state representation given in Fig. 4.8b shows stress continuity as the granular assembly is sheared. Initially, as γ = 0, the only stress applied to the granular assembly is a compressive stress in the vertical direction σ_N and the shear stress τ = 0. It follows that the principal stresses $\sigma_1 = \sigma_{yy} \approx \sigma_N$ and $\sigma_2 = \sigma_{xx}$ (see Fig. 4.8b). As the shear angle γ increases, Fig. 4.8b shows that the stress components σ_{xx} and σ_{yy} increase until the peak state is reached. For a dense sample, we have seen that shear causes dilation. The top boundary of the shear cell (side CD) tends to obstruct this dilation from happening, such that the normal stress acting on the top boundary $\sigma_{CD} = \sigma_{yy}$ increases. Simultaneously, given the boundary conditions, an increase of σ_{yy} and τ_{xy} results in an increase of σ_{xx}. In particular, as the principal stress direction is rotated at an angle $\theta_p = 45°$ from the vertical axis, we have $\sigma_{xx} = \sigma_{yy}$. In this case, as showcased in Fig. 4.8b, the stress path presents a symmetry with respect to the τ = 0 axis. Additionally, Mohr circle offers a useful graphical technique for

finding principal stresses, i.e., in the plane where $\tau_{xy} = 0$. Comparison between the principal stress values obtained from the polar representation given in Fig. 4.8a and from the Mohr circles in Fig. 4.8b demonstrates the validity of Equation (4.3) to compute principal stress values.

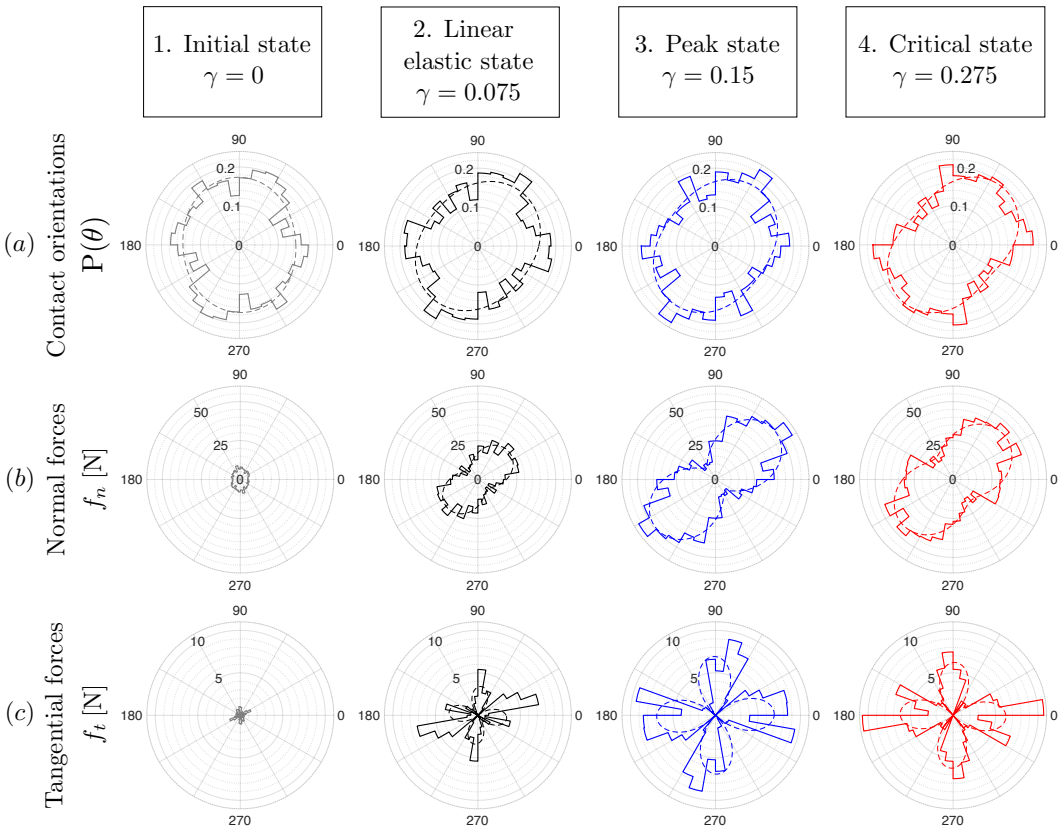

Figure 4.9: Polar distribution for shear test (σ_N = -14.25 kPa) at γ = 0, 0.075, 0.15 and 0.275 (a). Probability density function of contact orientations P(θ) (b). Average normal forces $\bar{f_n}(\theta)$ (c). Average tangential forces $\bar{f_t}(\theta)$

It can be seen from Equations (4.2) and (4.3) that the macroscopic stress tensor $\bar{\boldsymbol{\sigma}}$ and the magnitude of normal stress σ_A is linked to the contact forces and fabric. In order to gain a better understanding of the macroscopic behavior of granular materials during shear, it is therefore necessary to characterize the distribution of contact forces and contact orientations at the grain scale. We emphasize that for spherical grains, contact orientations are coincident with contact normal. Fig. 4.9a shows a polar histogram of the probability density function (pdf) of contact orientations P(θ), i.e., number of contacts within an interval $\Delta\theta$ divided by the total number of contact N_c times $\Delta\theta$. Polar histograms of average normal forces $\bar{f_n}(\theta)$ and average tangential forces $\bar{f_t}(\theta)$ for different values of shear angle are depicted in Fig. 4.9b

and Fig. 4.9c. Second order Fourier harmonic functions, as defined by [15, 76], are used to approximate the polar distributions and are represented as dashed lines in Fig. 4.9. The polar histograms shown in Fig. 4.9 confirm that shear stress applied to the granular assembly creates structural (fabric) anisotropy and mechanical (force) anisotropy.

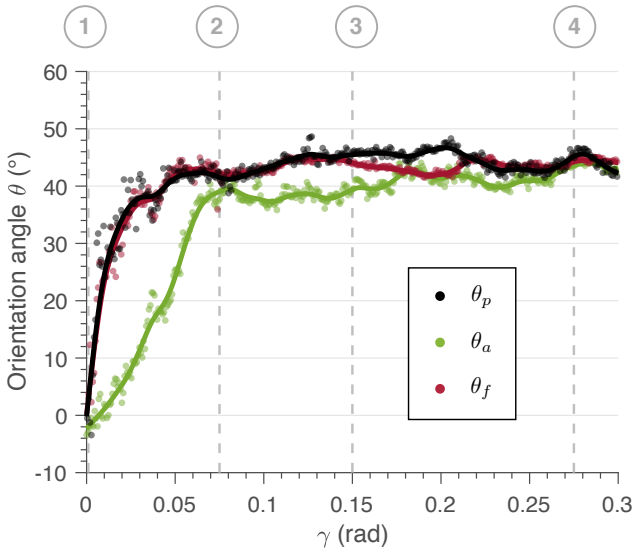

Figure 4.10: Principal stress orientation (black), contact orientation (green), and average normal forces orientation (red) as a function of shear strain . The curves are obtained by smoothing the data (shaded circle marker) using a smoothing spline [58].

From the grain-scale statistics and the Fourier expansions, we compute the angles θ_a and θ_f that correspond to the angles between the vertical axis and, respectively, the maximum value of contact orientation axis and the maximum value of average normal forces axis. In Fig. 4.10, principal stress orientation θ_p (black), contact orientation θ_a (green), and average normal force orientation θ_f (red) are plotted as a function of the shear strain γ. In this figure, the shaded circle markers represent the value of the different orientation angles θ obtained experimentally. The experimental data are then fitted using a smoothing spline [58]. The smoothed data is represented by the curves. Fig. 4.10 shows that the rotation of principal stress occurs in the early stage of the shearing process; for $\gamma > 0.05$, the principal stress orientation θ_p remains nearly constant and $\theta_p \approx 45°$. Throughout the shear deformation, principal stress orientation θ_p and average normal force orientation θ_f are coaxial. On the other hand, we experimentally demonstrate that the contact orientation θ_a does not generally coincide with the principal stress orientation θ_p except once critical state

is achieved ($\gamma > 0.225$) and at which $\theta_p \approx \theta_a \approx \theta_f$, as previously assumed in [15].

4.5 Closure

In this paper, we have described an experimental method that furnishes a complete description of the micro-mechanical state of granular materials: description of fabric (position of contact points and centroids), description of grain kinematics (displacements, rotations and strains) obtained using 2D-DIC and description of contact forces (normal and tangential components) obtained through GEM. We have introduced a novel experimental apparatus capable of reproducing the mechanical features of granular materials under shear loading. In particular, it has been shown that the so-called critical state is achieved at large shear strain. A uniaxial compression test was proposed as a benchmark test and has been successfully used to verify and validate the proposed experimental method. Under different loading conditions, force chains have been evidenced in an opaque granular assembly by means of 2D-DIC and quantified by GEM. We have connected macroscopic stresses to the microstructure through evolution of fabric and contact forces. Principal stress, contact, and average normal force orientations during shear have been studied and results show coaxiality between principal stress and average normal forces orientations while contact orientation is lagging behind until critical state is reached. These results may serve as a validation of DEM simulations and enhance our understanding of the multiscale behavior of granular materials.

Chapter 5

DO FORCE CHAINS EXIST? EFFECT OF GRAIN SHAPE ON FORCE TRANSMISSION AND MOBILIZED STRENGTH OF GRANULAR MATERIALS

5.1 Introduction

Granular materials are abundant in nature and highly manipulated in industries. Examples range from grains of sand to kernels of corn to pharmaceutical pills. Despite the seeming simplicity of the laws governing their individual constituents - grains -, granular assemblies exhibit rich and complex mechanical behavior arising from the interplay between grains [1]. Striking features observed in granular materials are intimately linked to the discrete and heterogeneous character of the media [117, 118]. Among these features, there has been a long-standing interest in studying the self-organization of contact forces into an anisotropic and heterogeneous network [33, 70, 119]. Under external loading, contact forces tend to align along the direction of maximum compression, eventually forming chain-like structures that serve as preferential pathways for force transmission. Such a phenomenon has become known as force chains [119].

Evidence of force chains was first furnished by photoelastic experiments performed on quasi-2D granular assemblies composed of birefringent disks [30, 33]. By providing a direct visualization of stress distributions, photoelasticity has shown that grains participating in force chains are highly engaged in load-bearing whereas, between chains, most grains carry little or no load. These strong spatial fluctuations are revealed by the probability density function of contact forces, which typically decays exponentially for forces greater than the mean [75, 120]. Numerical simulations performed with the Discrete Element Method (DEM) [14] confirmed the prevalence of force chains in granular materials subjected to external loadings [75, 119]. Force chains have been regarded as a key signature of granular materials and considered of central importance in coupling grain-scale processes to their overall constitutive behavior.

Photoelastic and DEM analysis have provided insights into the force transmission in highly idealized granular assemblies with simple geometries. Nevertheless, granular materials are composed of grains that come in a broad variety of shapes.

Experimental results quantifying contact forces and characterizing their properties in arbitrarily-shaped granular samples have yet to be collected. As a result, our understanding of the effect of grain shape on the force transmission is still very limited. Although force chains are widely believed to prevail in all granular materials, their existence in granular assemblies that yields realistic shape representation remains to be confirmed.

At the macroscopic scale, laboratory tests have revealed the crucial role of grain shape on the behavior of granular materials [121–127]. Material characteristics intimately affected by grain shape include the mobilized shear strength, volume change, and permeability. In particular, as grain shapes deviate from idealized circles (in 2D) and spheres (in 3D), an increase in mobilized shear strength is observed [128, 129]. It has been established that the mobilized shear strength of granular materials depends on the geometrical arrangement of the grains and on the force transmission [70]. Nonetheless, the grain-scale origin of the increased mobilized shear strength in arbitrarily-shaped assemblies has yet to be identified.

In this Chapter, we raise the following questions: to which extent do the well-known features of force chains evidenced in idealized granular materials apply to assemblies of arbitrarily-shaped grains? What is the influence of grain shape on the force transmission in granular materials? What are the underlying grain-scale mechanisms that contribute to an enhanced mobilized shear strength in assemblies of arbitrarily-shaped grains?

In an attempt to answer these questions, we present experimental results of shear tests performed on 2D analogue opaque granular assemblies. The role of shape is investigated by comparing data gathered from circular- and arbitrarily-shaped granular assemblies having the same grain size distribution and mechanical properties. Of particular interest are the contact forces, inferred in both assemblies by means of the Granular Element Method (GEM) [52, 82], from which the force chains are identified, the force transmission is studied, and strength-related quantities are derived.

For completeness, the Chapter is organized as follows. We first introduce in section 5.2 the experimental procedure that utilizes the custom-built shear apparatus presented in Chapter 4 We describe the design and manufacturing process of the granular assemblies as well as the measurements that are performed. In section 5.3, we present the grain- to continuum-scale results obtained from shear tests performed at different initial packing densities. We conclude in section 5.4 with a summary of

our findings.

5.2 Experimental procedure

Granular assemblies

Experimental tests are conducted on granular assemblies composed of either circular-shaped grains or arbitrarily-shaped grains. While the circular- and arbitrarily-shaped granular assemblies differ in shape, both assemblies have the same mechanical properties and grain size distribution. Details on the design and manufacturing, morphology, and grain size distribution of the assemblies are presented below.

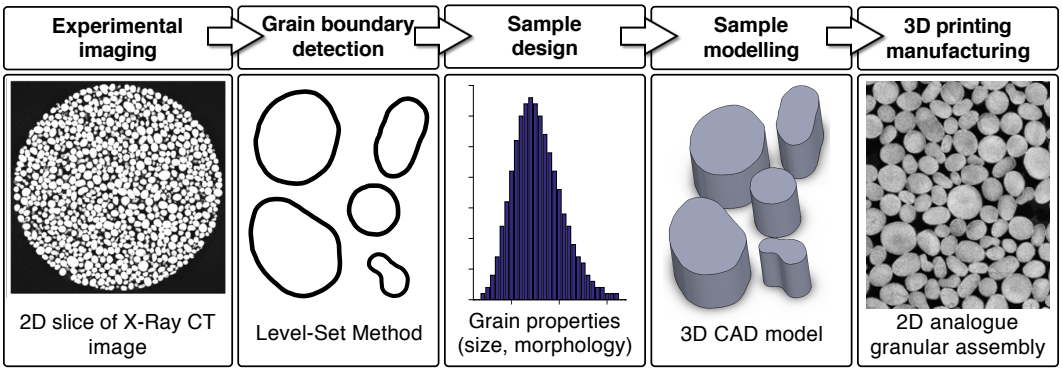

Figure 5.1: X-Ray Computed Tomography (XRCT)-to-3D printing process. The reader is referred to Section 5.2 for a detailed discussion of the steps involved.

A visual schematic of the development process for the arbitrarily-shaped granular assembly is depicted in Figure 5.1. The arbitrarily-shaped granular assembly is devised based on a real sample of a rounded natural sand (Caicos ooids). We start from three-dimensional volume data of sand grains obtained directly from X-Ray Computed Tomography (XRCT) [7, 130]. A typical 2D slice image of the specimen obtained with XRCT is shown in the left panel of Figure 5.1. Individual sand grain boundaries in the sample are detected using a 2D level set representation as obtained by Lim et al. [130], following the characterization methodology proposed by Vlahinic at al. [131]. From this characterization technique of the grain boundaries, 11 grain shapes are retained for their different morphological properties. Sphericity and roundness (or angularity) are chosen as morphological descriptors due to their widespread use in the fields of geomechanics and geology [132, 133]. Figure 5.2 depicts the selected grain contours as a function of sphericity and roundness. Grain shapes range from elongated to nearly spherical and from rounded to well rounded.

The selected grain shapes are duplicated and scaled to follow a log-normal distribu-

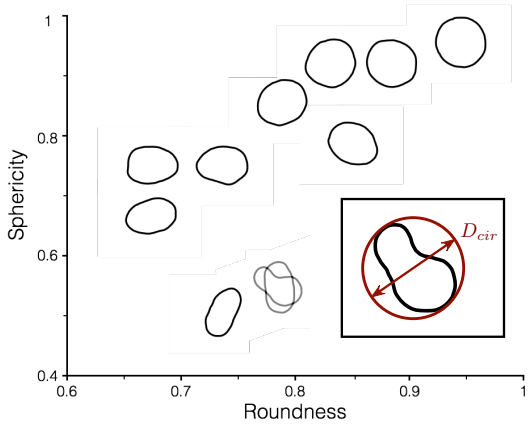

Figure 5.2: Selected grain shapes of real sand (Caicos ooids) as a function of sphericity and roundness. Sphericity and roundness are computed using the numerical method developed in [134]. Inset: Definition of circumscribed circle and diameter.

tion. Computer-aided design (CAD) models are created by extending the 2D grain contours into 3D with an extrusion depth set to 20 mm. The generated 3D CAD models are used as input files for 3D printing. The XRCT-to-3D printing process introduced in Figure 5.1 enables the fabrication of a 2D analogue granular assembly that captures the complexity of grain shapes found in real sand.

Both assemblies, circular- and arbitrarily-shaped, were fabricated using the same manufacturing process. Grains were 3D printed using Stratasys Objet500 Connex3 printer [135]. This printer uses inkjet 3D printing technology with a microscopic layer resolution and accuracy of 16 μm [136]. Printing material is a rubber-like material (Stratasys FLX9895DM) that is obtained by mixing a rigid plastic (Stratasys VeroWhitePlus RGD835) with a flexible elastomer (Stratasys TangoBlackPlus FLX980). Factors such as the orientation of the print, printing mode, support material composition and removal, and environmental conditions of storage of raw materials were kept constant for all 3D-print jobs. Hence, the printed grains constituting the circular- and arbitrarily-shaped assemblies have identical mechanical properties [137, 138]. In particular, the grains have a Young's modulus $E = 63$ MPa and a Poisson's ratio ν of approximately 0.5.

For both assemblies, the distribution of grain diameters D is fitted to a log-normal distribution with mean μ and standard deviation σ, such that $\ln(D) \sim \mathcal{N}(\mu, \sigma^2)$. The distribution parameters were chosen to be $\sigma = 0.2$ and $\mu = \ln(25)$. For the arbitrarily-shaped granular assembly, the grain diameter D is defined as the diameter

of the smallest circumscribed circle D_{cir}, as illustrated in the inset of Figure 5.2. The circular-shaped sample is composed of 313 grains while the arbitrarily-shaped one has a total of 398 grains. In both assemblies, grain diameters D ranges between 14 mm $< D <$ 42 mm.

Measurements

The mechanical apparatus presented in Chapter 4 allows for simultaneous measurements from the grain to the continuum scale. A full characterization of the grain-scale quantities that controls the mechanical behavior of granular materials is extracted throughout the shear deformation. First, a description of the geometrical arrangement, or fabric, of the granular assembly is obtained using image processing techniques. The watershed segmentation algorithm [86–88] from Matlab Image Processing toolbox is employed in combination with a priori knowledge of the true grain contours (as seen in Figure 5.2) to determine grain and contact positions. Second, a description of grain kinematics, i.e., displacement, rotation and strain field, is extracted using the Digital Image Correlation (DIC) technique [61, 62]. Third, a description of contact forces is obtained using the Granular Element Method (GEM) [52, 82, 139]. GEM provides a mathematical framework that, when combined with fabric information and average grain strains, allows for the inference of the contact forces. Unlike photoelasticity, the GEM methodology enables reconstruction of the force network in opaque, arbitrarily-shaped granular assemblies.

At the continuum scale, the stress state $(\sigma_{xx}, \sigma_{yy}, \tau_{xy})$ of the granular assembly subjected to shear deformation is computed. The Cauchy stress tensor $\bar{\boldsymbol{\sigma}}$ is linked to grain-scale quantities and expressed in terms of contact forces and fabric according to the following well-established equation [95]:

$$\bar{\boldsymbol{\sigma}} = \frac{1}{\Omega} \sum_{\alpha=1}^{N_c} \mathrm{sym}(\boldsymbol{f}^{\alpha} \otimes \boldsymbol{d}^{\alpha}) \tag{5.1}$$

where N_c is the total number of contact points, Ω is the total volume of the granular assembly, $\boldsymbol{f}^{\alpha}$ is the contact force, and $\boldsymbol{d}^{\alpha}$ is the branch vector at the contact α. GEM associated with Eq. (5.1) enables the connection between contact forces in realistic-shaped granular materials and macroscopic stresses.

5.3 Experimental results

Quasi-static simple shear tests are performed to investigate how grain shapes affect the force transmission and grain-scale mechanics that ultimately controls the mobilized shear strength. The subsequent sections provide experimental results of a series of four shear tests. Two tests are conducted on the circular-shaped assembly while two other tests are conducted on the arbitrarily-shaped assembly. At the beginning of each test, the grains are randomly arranged into the shear cell, so that the sample is initially isotropic with no preferred contact orientation. For both circular- and arbitrarily-shaped assemblies, one dense and one loose sample are created by varying the initial packing density. Prior to starting the shearing stage, a normal stress of σ_N = 26.3 kPa is applied. The granular assembly is then sheared at a constant rate $\dot{\gamma}$ = 0.002 s^{-1} and image sequences are acquired at a frame rate of 7 images per second. During the shear deformation, measurements described in Section 5.2 are performed.

Macroscopic measurements

Figure 5.3 compares the macroscopic mechanical response of circular- and arbitrarily-shaped samples with initial dense and loose packing densities. In this figure, stress ratio μ, volumetric strain ϵ_V, void ratio e, and dilatancy β is plotted as a function of shear strain γ with each curve corresponding to a different assembly.

The stress ratio μ represents the mobilized shear strength of cohesionless granular materials and is defined as the ratio of shear stress τ_{xy} to normal stress σ_{yy}. The stress components τ_{xy} and σ_{yy} are computed from grain-scale quantities according to Eq. (5.1). In Figure 5.3a, the observed stress-strain behaviors are characteristic of dense and loose samples under shear deformation [4, 97, 98]. Dense samples (red and blue lines) exhibit a linear elastic behavior followed by a peak in shear stress and subsequent strain softening, whereas in loose samples (gray and black dashed lines) no peak is observed. At large shear strain values, circular- (circle markers) and arbitrarily-shaped (asterisk markers) assemblies show a tendency to stabilize around an asymptotic stress ratio value μ_c that is independent on the initial packing density (dense or loose).

Evolution of volumetric strain ϵ_V as a function of shear strain γ is presented in Figure 5.3b. The volumetric strain is simply related to the normal strain, such that $\epsilon_V = \text{tr}(\boldsymbol{\epsilon}) = \epsilon_{yy}$. In terms of volumetric deformations, we once again observe typical behaviors of dense and loose samples subjected to shear. Dense samples

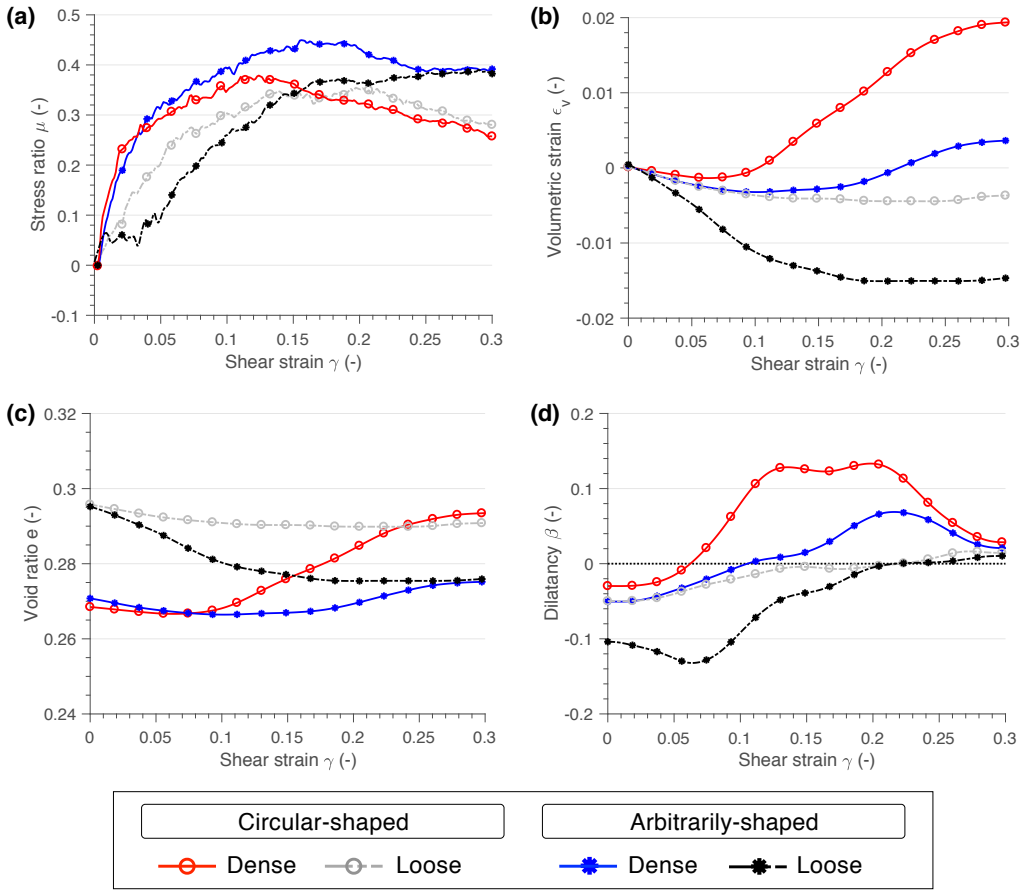

Figure 5.3: Macroscopic results. (a). Stress ratio μ (b). Volumetric strain ϵ_v (c). Void ratio e (d). Dilatancy β as a function of shear strain γ

dilate after an initial contraction while loose samples only contract. For large shear deformations, the volumetric strain of both dense and loose samples reaches a constant value.

As the grains are considered incompressible, the change in volume observed in Figure 5.3b occurs due to change in the volume of voids, measured by the void ratio e. The void ratio e is defined as the ratio of the volume of voids to the volume of solid particles and is plotted as a function of the shear strain γ in Figure 5.3c. Loose samples (gray and black dashed lines) start at an initial void ratio $e_0 = 0.295$ while dense samples (red and blue lines) start at a lower value of $e_0 = 0.27$. At large shear strain values, loose and dense samples evolve towards an identical and constant value of void ratio e_c that is different for arbitrarily-shaped (asterisk markers) and the circular-shaped (circle markers) assemblies.

The Reynolds dilatancy β [22] describes the change in volume associated with the

shear deformation of granular materials, and relates the volumetric and shear strain rates by $\dot{\epsilon}_v = \beta\,\dot{\gamma}$. Figure 5.3d displays the evolution of dilatancy β as a function of the shear strain γ. It can be seen that, for all samples, dilatancy β vanishes for $\gamma > 0.25$.

These macroscopic results show that, for shear strains $\gamma > 0.25$, all samples reach critical state, conceptually defined as the equilibrium state in which no further change in volume and stress state occur with increased shear deformation. Nevertheless, the critical state values of stress ratio μ_c and void ratio e_c are different for the circular- and the arbitrarily-shaped assemblies. The arbitrarily-shaped assembly exhibits a significantly higher mobilized stress ratio of $\mu_c \approx 0.38$, and thus higher shear strength, than the circular-shaped assembly for which $\mu_c \approx 0.27$. The arbitrarily-shaped assembly reaches a critical void ratio $e_c \approx 0.275$ that is lower than that of the circular-shaped assembly ($e_c \approx 0.293$).

The macroscopic results presented in Figure 5.3 are consistent with previous studies that investigated the effect of shape on the bulk properties of granular materials [121–127]. The overall mechanical behavior of real granular materials (e.g., sand) subjected to shear deformations is reproduced by the conducted tests. This qualitative agreement confirms the validity of the proposed experimental capability to investigate the effect of shape on the force transmission and grain-scale mechanics of realistic granular materials.

Grain-scale measurements

By examining the response of granular assemblies with different grain shapes and initial packing densities under shear deformation, differences in the macroscopic mechanical behavior have been revealed. As the mechanical behavior of granular materials is fundamentally encoded at the grain scale, in this section, we gain insights into the grain-scale properties of the different granular assemblies (dense and loose, circular- and arbitrarily-shaped) from the measurements described in Section 5.2. Figures 5.4 to 5.7 present snapshots of 2D-DIC results and contact force networks obtained with GEM for the four different assemblies at a shear strain $\gamma = 0.25$. We emphasize that, as shown in Figure 5.3, all samples have reached critical state at $\gamma = 0.25$.

Average grain rotations $\bar{\theta}$ obtained from 2D-DIC are plotted in Figure 5.4. Dark and light blue contours correspond to counterclockwise (positive) rotations, red and orange contours to clockwise (negative) rotations while green contours depict

nearly zero rotation (-0.5° < $\bar{\theta}$ < 0.5°). It can be observed that, for all samples, the grain rotations are in majority counterclockwise, which is consistent with the imposed (counterclockwise) shear angle γ. Grains with counterclockwise rotation (dark and light blue) form random clusters whereas grains with clockwise rotation (red and orange) are more isolated. The intra-grain strain field ϵ_{xy} measured using 2D-DIC is represented in Figure 5.5. Strain fields ϵ_{xx} and ϵ_{yy} are also measured but not depicted in this Chapter. The full-field intra-particle stress distribution (σ_{xx}, σ_{yy} and σ_{xy}) and associated principal stresses (σ_1 and σ_2) is then deduced from the full-field intra-particle strain measurements (ϵ_{xx}, ϵ_{yy} and ϵ_{xy}) assuming linear elasticity. The difference in principal stresses $\sigma_1 - \sigma_2$ is plotted in Figure 5.6. Figures 5.5 and 5.6 show that 2D-DIC measurements of strains and stresses provide qualitative assessments and insights into the force distribution in circular- and arbitrarily-shaped granular assemblies under shear. Full-field stresses (σ_{xx}, σ_{yy} and σ_{xy}) and fabric information are used as inputs into GEM mathematical framework to infer normal and tangential contact forces. The reconstructed force network is plotted in Figure 5.7. Figures 5.7b and d offer the first visualization of contact forces in a granular assembly composed of grains whose shapes are directly extracted from a real sand sample. As one can see in Figures 5.7b and d, in the arbitrarily-shaped assembly, we observe the formation of chain-like structures that resemble force chains. Furthermore, at first glance, the force transmission is different in each assembly. Grain shape appears to play a role in the development of force chains as the pattern of force transmission looks less heterogeneous and more uniformly spread in the arbitrarily-shaped samples (Figures 5.7b and d) when compared to the circular-shaped samples of similar initial packing density (Figures 5.7a and c). We report two notable differences between the force transmission in circular- and arbitrarily-shaped assemblies. First, in the circular-shaped assemblies, most grains carry little or no load, whereas, in the arbitrarily-shaped assemblies, a larger proportion of grains belongs to the load-bearing network. Second, the more localized force chains in the circular-shaped samples lead to significantly higher contact forces. These aspects are analyzed in more detailed in the following section.

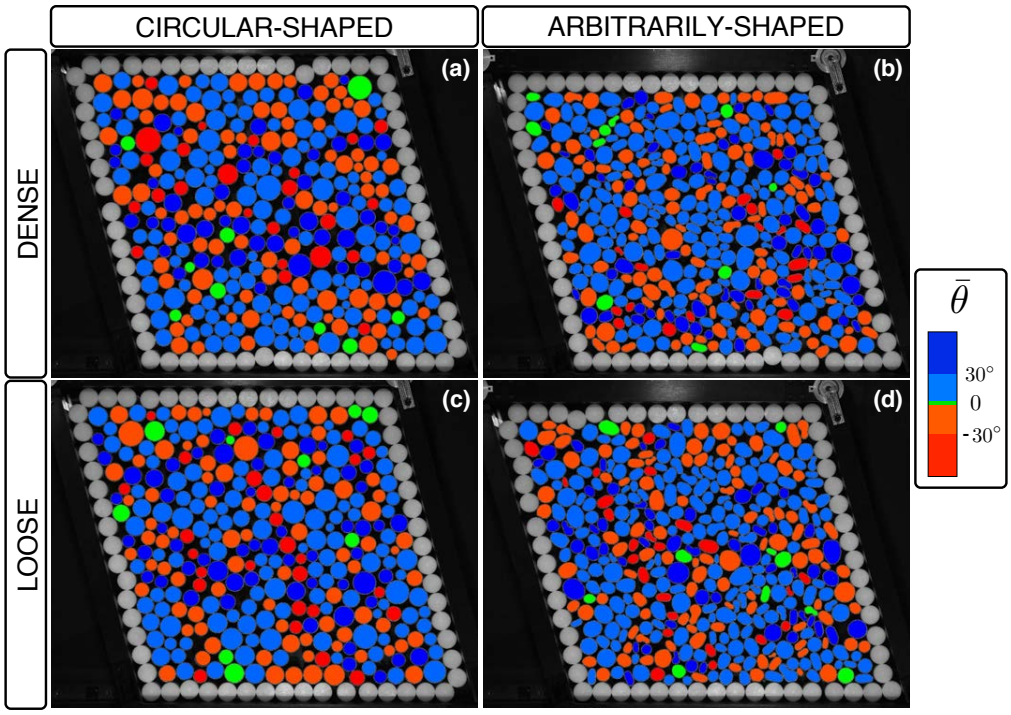

Figure 5.4: Average total grain rotation at $\gamma = 0.25$.

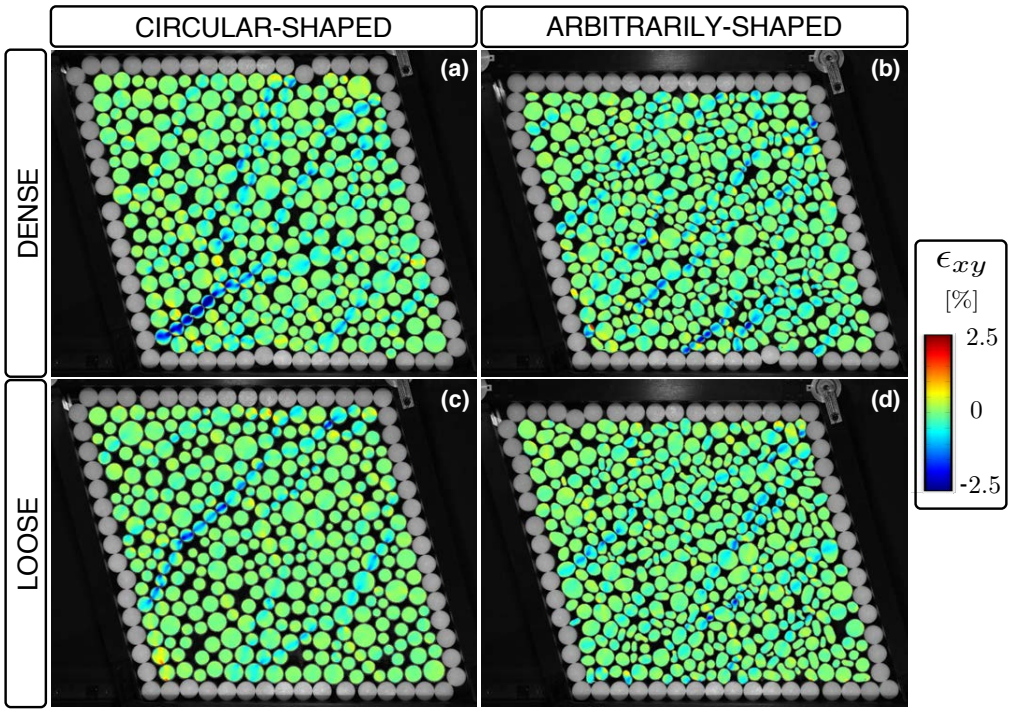

Figure 5.5: Contour distribution of strain component ϵ_{xy} at $\gamma = 0.25$ obtained from DIC measurements.

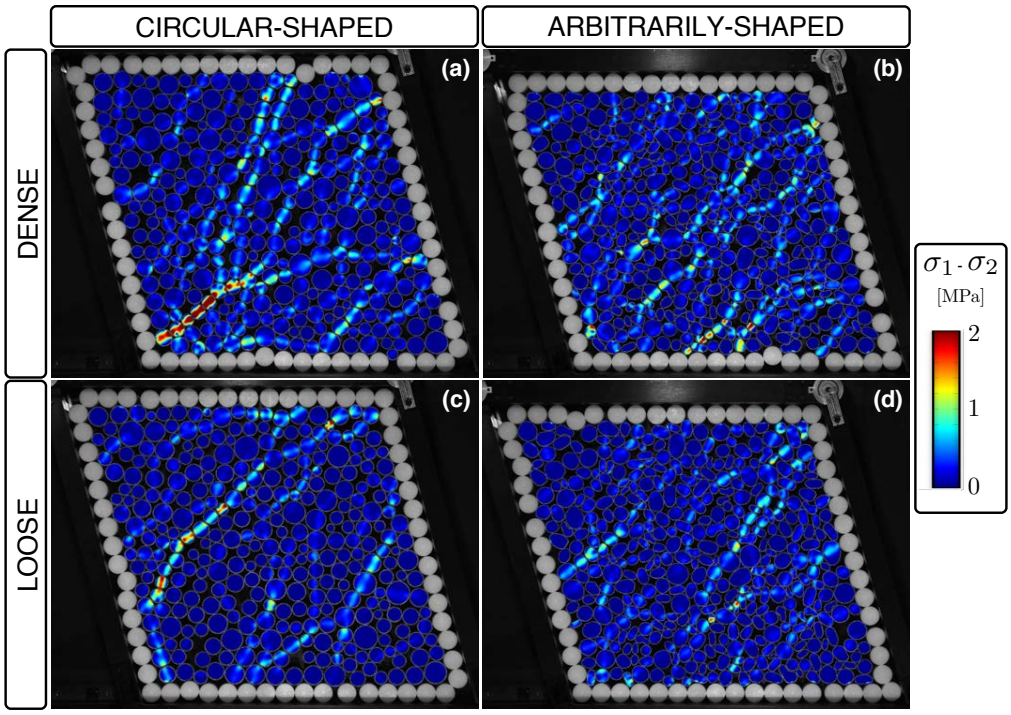

Figure 5.6: Contour distribution of difference in principal stresses $\sigma_1 - \sigma_2$ at $\gamma = 0.25$.

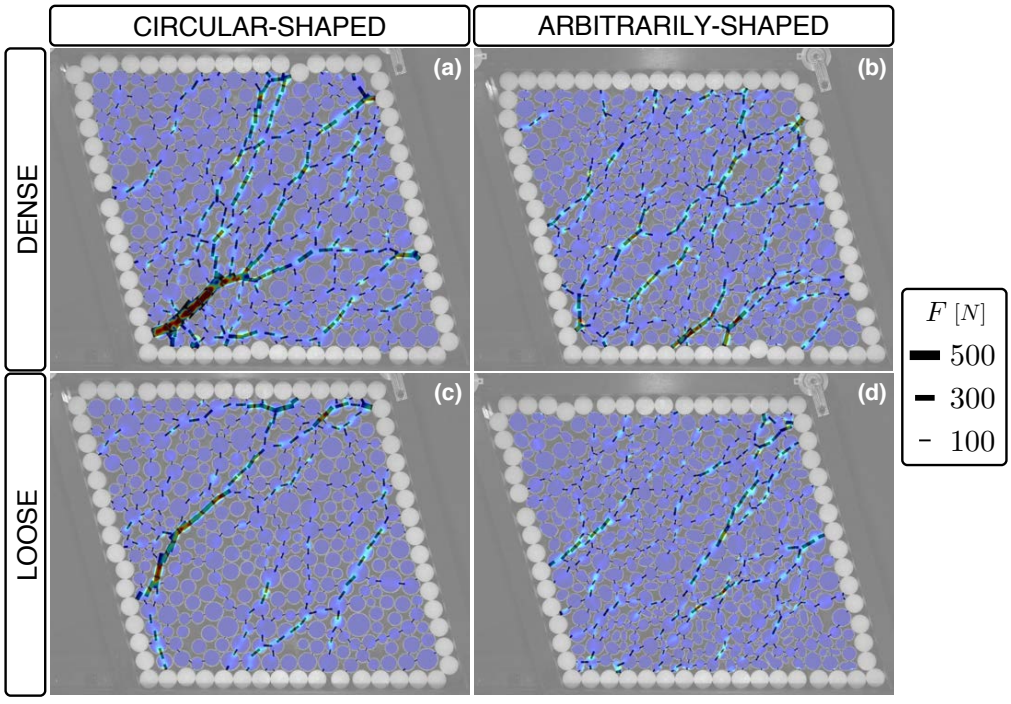

Figure 5.7: Contact forces inferred with GEM superimposed on difference of principal stresses $\sigma_1 - \sigma_2$ at $\gamma = 0.25$.

Evolution of grain-scale mechanics

Grain rotations

The evolution of mean and standard deviation (std) of grain rotations $\bar{\theta}$ as a function of the shear strain γ for the four different assemblies is plotted in Figure 5.8. Figure 5.8 shows that the mean value of grain rotation $\bar{\theta}$ linearly increases as the granular assembly is sheared and is equal for all samples. Hence, the mean value of grain rotation $\bar{\theta}$ is independent of grain shape and initial packing fraction. Additionally, the mean rotation is compared with the rigid rotation angle Ω associated with the simple shear deformation of the cell. For any given deformation, the deformation gradient $\boldsymbol{F}$ can be decomposed into the product of a stretch tensor $\boldsymbol{U}$ and a rotation matrix $\boldsymbol{R}$ using the polar decomposition concept, such that $\boldsymbol{F} = \boldsymbol{U} \cdot \boldsymbol{R}$. The previous expression separates deformation (described by $\boldsymbol{U}$) and rigid body rotation (described by $\boldsymbol{R}$). The rigid rotation Ω corresponds to the angle of the rotation matrix $\boldsymbol{R}$. In Figure 5.8, we observe that the mean value of grain rotation $\bar{\theta}$ agrees with the non-zero rigid body rotation Ω associated with the macroscopic deformation of the shear cell. Thus, the mean value of grain rotation $\bar{\theta}$ is dependent on the imposed rotational component of deformation. In other words, the essence of grain rotation is related to the macroscopic rigid rotation. It can be seen in Figure 5.8 that the standard deviation (std) of grain rotation $\bar{\theta}$ also increases linearly as the granular assembly is sheared. Nevertheless, at the end of the shearing process, the standard deviation is significantly larger for the circular samples than for the arbitrarily-shaped samples, indicating more variations from the mean value. This wider rotation distribution suggests that the circular assemblies are more disordered. Under the same conditions, a circular grain can rotate more easily compared to an arbitrarily-shaped grain inside their respective assemblies. Hence, as it has been previously reported [133], a decrease in sphericity (e.g., more elongated grains) increases the tendency of rotational frustration. Figure 5.8 shows that the standard deviation is the same for dense and loose circular-shaped assemblies and dense and loose arbitrarily-shaped assemblies. Hence, the ability of grains to rotate is independent of the initial packing density (dense or loose) but depends on the grain shape.

Coordination number

The average number of contacts per grain, defined as the coordination number z, is an important grain-scale quantity that influences the stability and force transmission

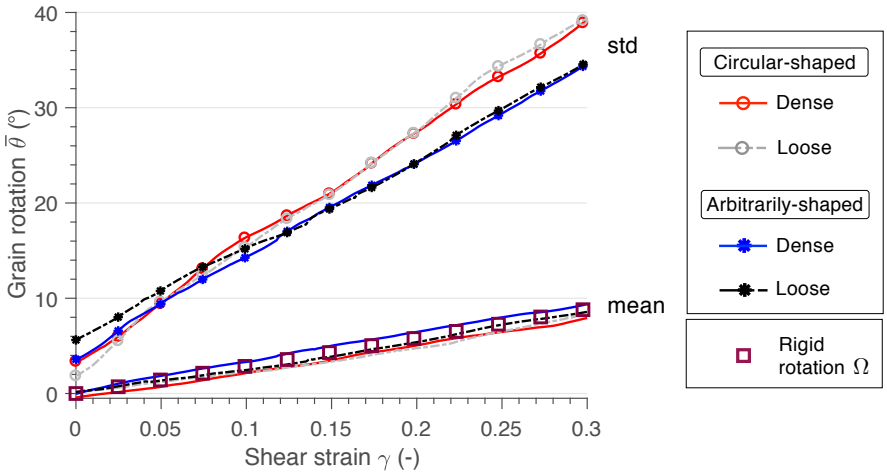

Figure 5.8: Mean and standard deviation of grain rotations $\bar{\theta}$ as a function of shear strain γ for the four different samples.

of a granular assembly [140]. In Figure 5.9, the coordination number z, is plotted as a function of the shear strain γ. The coordination number z provides information on the creation and loss of contacts. Initially (at $\gamma = 0$), as expected, the coordination number z of loose samples (gray and black dashed curves) is smaller than the one of dense samples (red and blue curves). As the granular assemblies are sheared, the coordination number z of dense samples decreases, corresponding to a loss of contacts. Simultaneously, the coordination number z of loose samples increases, owing to the creation of new contacts. We emphasize that the samples with initial void ratio e_0 far from their critical void ratio e_c, i.e., the dense circular-shaped and loose arbitrarily-shaped loose samples (respectively, red line and black dashed line), manifest larger variation of coordination number z. Once critical state is reached, for $\gamma > 0.25$, the coordination number z stabilizes to a constant value that is larger for the arbitrarily-shaped assemblies than for the circular assemblies. This constant value of coordination number z is an indication that the contact network has evolved towards a steady structure. The fact that the coordination number z at critical state is higher for the arbitrarily-shaped assemblies than for the circular-shaped assemblies has many implications for the grain-scale mechanics of granular materials. A higher coordination number z suggests that more paths are available for force propagation, which ultimately influences the distribution of forces towards strongly less heterogeneous force networks. A higher coordination number z also increases the stability of the contact network structure as there are more mechanical constraints.

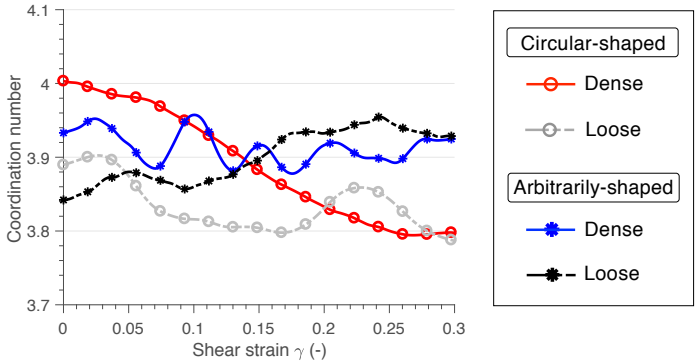

Figure 5.9: Evolution of coordination number as a function of shear strain γ

Force distribution

Although the force networks of both the circular- and arbitrarily-shaped assemblies are heterogeneous and characterized by the formation of force chains, Figure 5.7 suggests that the distribution of contact forces is affected by grain shape. In this section, the force transmission is studied by computing the probability density function of normalized forces $f_n/\langle f_n \rangle$, where $\langle f_n \rangle$ is the mean value of normal forces. Figure 5.10 shows the probability density function $P(f_n)$ of normal forces f_n at critical state in the dense and loose samples in log-linear scale. The data are averaged from several snapshots at critical state, i.e., for $\gamma > 0.25$. Following Radjaï et al. [76], we designate the forces below the mean normal force ($f_n < \langle f_n \rangle$) as the 'weak' network and the forces above the mean normal force ($f_n > \langle f_n \rangle$) as the 'strong' network. The concept of 'weak' and 'strong' networks provides a quantitative description of force network that will be used in the remaining of this Chapter. As is often reported in the literature on granular materials [75, 120, 141, 142], we find that the probability density function is characterized by an exponential decay for the forces above the mean force $\langle f_n \rangle$ (i.e., in the 'strong' network), such that:

$$P(f_n) \propto \exp(-\beta_n f_n) \tag{5.2}$$

where β_n is a positive constant. The results presented in Figure 5.10 clearly show a broader uniformity of the normal force distribution in the assemblies composed of arbitrarily-shaped grains than in the circular-shaped assemblies. In other words, there is a significantly lower chance of an individual contact force largely exceeding the mean force in the arbitrarily-shaped samples. This broader uniformity is

consistent with the higher coordination number z measured in the arbitrarily-shaped assemblies, as it provides more pathways for force transmission. In the circular-shaped assemblies, while the number of 'strong' contacts declines, stronger force chains occur. In close connection with the shear strength, the force transmission is strongly influenced by grain shapes.

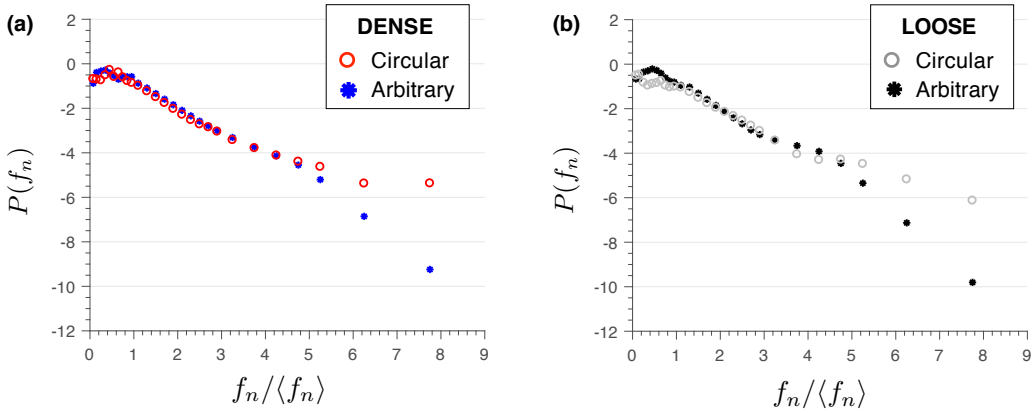

Figure 5.10: Probability density function $P(f_n)$ of normal forces f_n in log-linear scale at critical state ($\gamma > 0.25$) for the (a). dense and (b). loose samples.

Contact deformation mechanisms

In order to accommodate an imposed shear deformation, the granular structure must rearrange through grain-to-grain interactions at contact points [143]. We identify three possible rearrangement mechanisms at a contact point α between two grains p and q. As illustrated in Figure 5.11, grains can interlock or move past each other by rolling or sliding. Definitions, solely based on geometrical criteria, are provided for each contact mechanism.

Interlocking occurs when two grains rotate (or translate) together as a single rigid body. The distance between any arbitrary chosen points on the two grains remain constant during the motion and rotate by the same amount $\Delta\theta$. Hence, there is no relative movement between the two grains. Rolling occurs when two grains rotate over each other in a gear-like manner such that the contact point changes its relative location from the grains centroid. When grains are rolling, the arc lengths representing the displacement of the contact point α have opposite signs. In other words, while one grain rotates clockwise, the other one rotates counterclockwise. Sliding occurs when both grains rotate through the same angle $\Delta\theta$ and the arcs

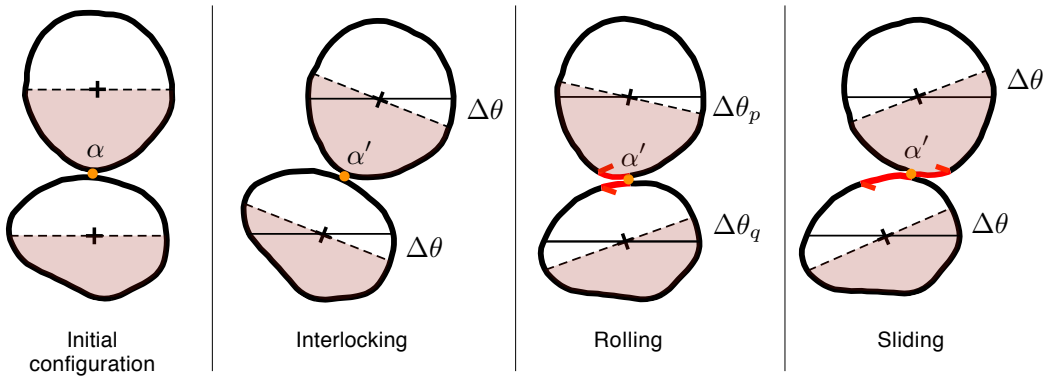

Figure 5.11: Possible mechanisms that can occur at a contact α

representing the displacement of the contact point α have the same signs. When sliding, the grains rotate both clockwise or counterclockwise. A fourth category is defined as a combination of these mechanisms and occurs when one contact mechanism is not prevalent. Given these definitions, we identify the population of contacts for which each mechanism is dominant. The total number of contacts can be decomposed as follows:

$$N_{tot} = N_I + N_R + N_S + N_* \tag{5.3}$$

where N_{tot} is the total number of contacts in the assembly and N_I, N_R and N_S are the number of contacts where, respectively, interlocking, rolling, and sliding are the dominant mechanism. N_* corresponds to the number of contacts for which the mechanism is not clearly identified (e.g., combination of contact mechanisms, creation or destruction of contact). The contact contribution of each mechanism is simply obtained by dividing each population by the total number of contacts N_{tot} and is plotted in Figure 5.12 as a function of the shear strain γ. In this figure, it can be seen that rolling (gold shade) is the prevalent grain-scale deformation mechanism for the circular-shaped granular assembly with about 50% of N_{tot} throughout shear deformation. Interlocking contribution (black shade) is 20-25% for the circular-shaped samples and about 40% for the arbitrarily-shaped samples. In the arbitrarily-shaped assembly, no dominant deformation mechanism is identified as rolling and interlocking have approximately the same contribution. An assembly composed of arbitrarily-shaped grains exhibits less rolling and more interlocking than one composed of circular-shaped grains. The difference in rolling contribution between the circular- and arbitrarily-shaped assemblies is consistent with the results obtained

from standard deviation of grain rotation $\bar{\theta}$ presented in Figure 5.8. Owing to the prevalence of the rolling mechanism, circular-shaped grains experience a wider range of grain rotation. Correspondingly, grain shape induces a resistance to grain rotation that results in a lower contribution from rolling contacts. For all samples, relatively few contacts are sliding (red shade), accounting for 12-15% of N_{tot}. The white shade corresponds to the contacts for which a mechanism is not clearly identified, which is composed of approximately 10% of N_{tot}.

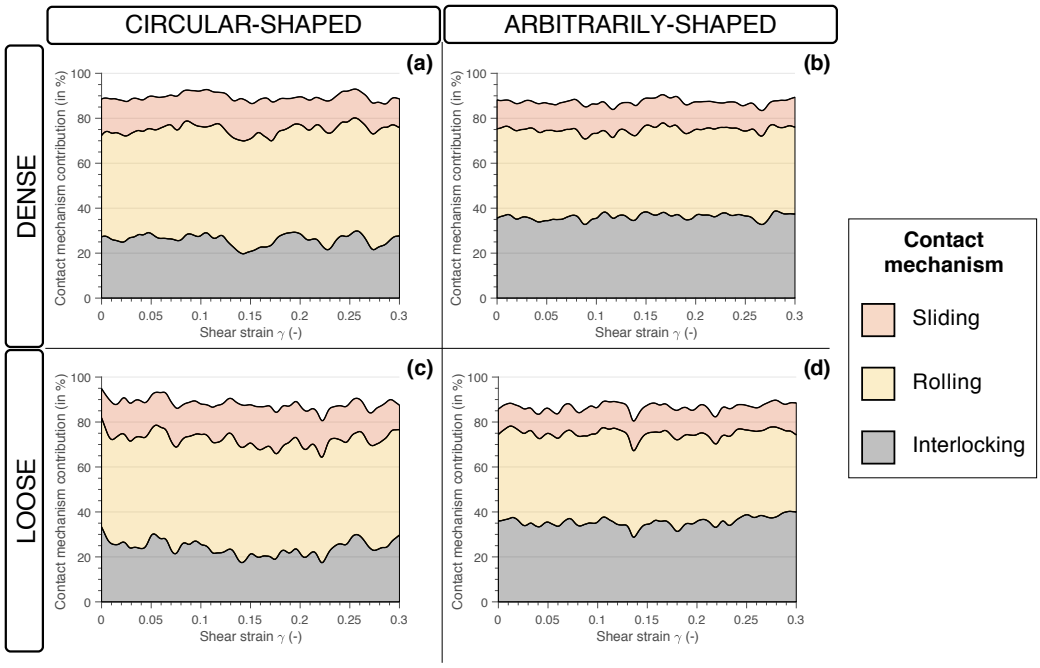

Figure 5.12: Contribution of contact mechanisms to the total number of contacts N_{tot}. Contact mechanisms are identified as interlocking, rolling and sliding.

Figure 5.13 offers another visualization of the force network in the dense circular- and arbitrarily-shaped assemblies at $\gamma = 0.25$. In this figure, the normal component of forces is categorized according to its dominant contact mechanism: sliding (red), rolling (gold), or interlocking (black). The thickness of the segments joining the grain centroids is proportional to the magnitude of the normal forces. Figure 5.13 shows that, at interlocking contacts (black lines), relatively large forces are transmitted, even more so in the circular-shaped assembly (see Figure 5.13a).

In an attempt to connect grain-scale processes to the continuum behavior of granular materials, we investigate the contribution of each contact mechanism to the shear strength μ that is described by the stress ratio $\mu = \tau_{xy}/\sigma_{yy}$. The contribution of each contact mechanism to the total shear stress τ_{xy} is obtained from the general equation

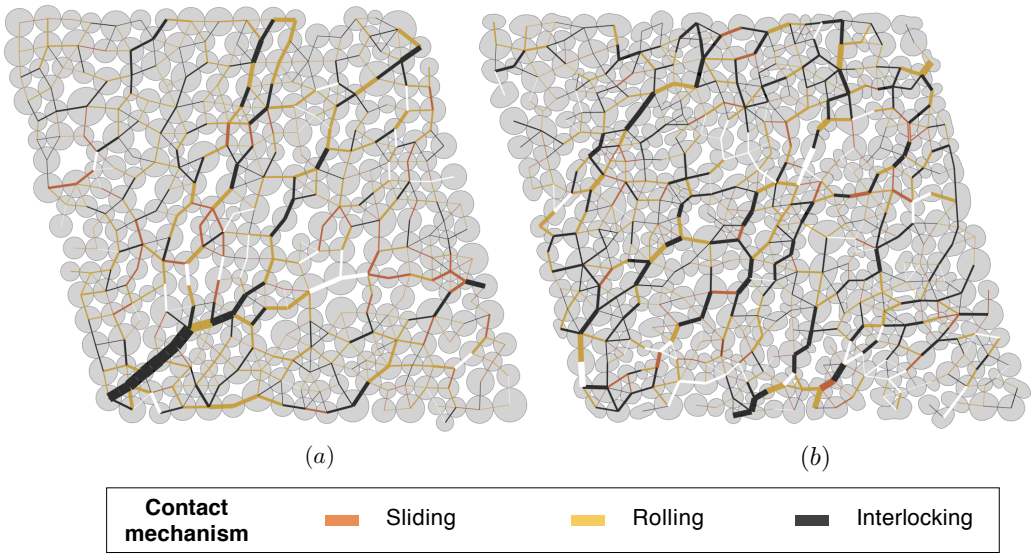

Figure 5.13: Normal component of contact forces at $\gamma = 0.25$ for the dense (a). circular- and (b). arbitrarily-shaped assemblies. Forces are categorized according to their dominant contact mechanism: sliding (red), rolling (gold), and interlocking (black).

of the stress tensor (Eq. 5.1) by limiting the summation to the contacts belonging to each deformation mechanism [144]. Accordingly, partial shear strength μ_I, μ_R, μ_S, and μ_* are calculated for each deformation mechanism, such that the following additive decomposition holds:

$$\mu = \mu_I + \mu_R + \mu_S + \mu_* \tag{5.4}$$

The contribution of each deformation mechanism to the shear strength μ as a function of shear strain γ is presented in Figure 5.14. This figure reveals that the additional shear strength measured in the arbitrarily-shaped assembly is furnished by the interlocking mechanism. It can be seen that, at critical state ($\gamma > 0.25$), the partial shear strength μ_I due to the interlocking in the arbitrarily-shaped assembly is almost double the value of μ_I in the circular-shaped assembly. In the circular-shaped assembly, even though rolling is the prevailing deformation mechanism in terms of contact contribution, the shear strength μ_R associated with rolling is similar to the shear strength μ_I associated with interlocking. Correspondingly, in the arbitrarily-shaped assembly, although rolling and interlocking have approximately the same contribution to N_{tot}, rolling does not provide as much shear strength as interlocking. These results alongside the force networks depicted in Figure 5.13

suggest that interlocking is a stable mechanism for larger contact forces to develop, which accordingly enhances the load bearing capacity of the granular assembly. Moreover, as shown in Figure 5.14, the shear strength gain associated with sliding is relatively small. Sliding occurs when the tangential force f_t reaches a critical value governed by the Coulomb friction law, such that $|f_t| = \mu_p |f_n|$, where μ_p is the inter-particle friction coefficient. A visual inspection of Figure 5.13 reveals that most sliding contacts belong to the 'weak' network ($f_n < \langle f_n \rangle$), which results in a small value of the partial shear strength μ_S. Finally, by adding the shear strength of non-identified contacts μ_*, the macroscopic stress-strain curve is reconstructed. Figure 5.14 offers insights into the grain-scale origin of shear strength in granular materials.

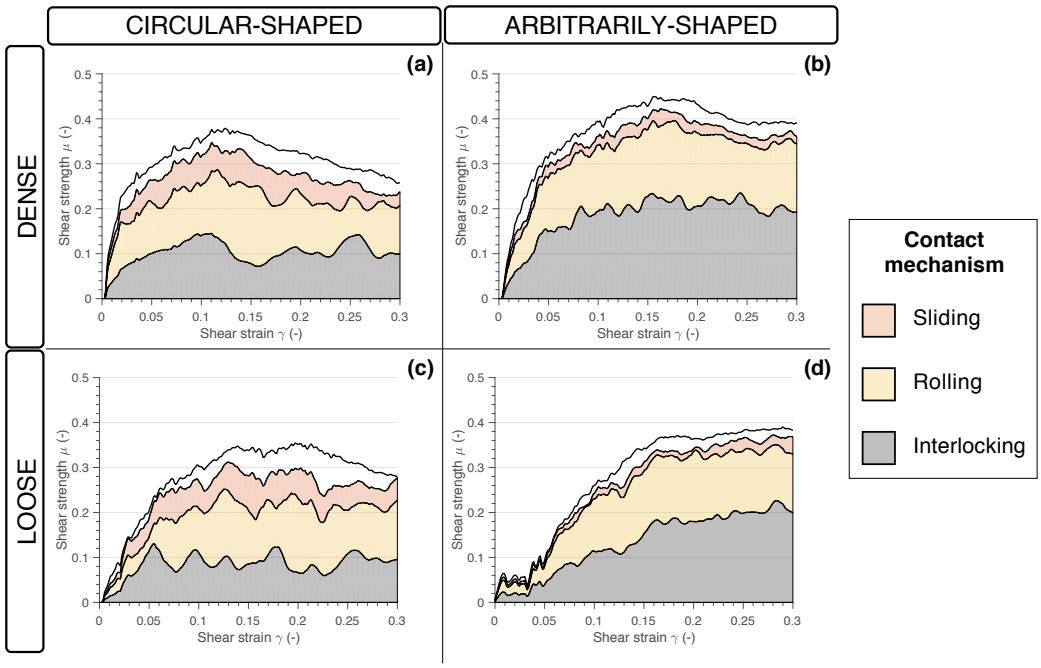

Figure 5.14: Contribution of contact mechanisms to the total shear strength μ.

5.4 Summary and closure

In this Chapter, we carried out a detailed study of the effect of grain shape on the mechanical behavior of sheared granular materials across scales. Grain shapes were directly extracted from a real sand sample to engineer a 2D analogue granular assembly. At the grain-scale, we provided unprecedented visualizations and quantitative descriptions of the force network in assemblies composed of arbitrarily-shaped grains. Particular attention was given to the influence of grain shape on grain-scale

quantities that are known to control the mechanical response of granular materials, i.e., the average grain rotation, the coordination number and the distribution of contact forces. At the macroscopic scale, experimental results of mobilized shear strength and volumetric strain exhibit a typical shear response of dense and loose samples. Once critical state is reached, we report an enhanced mobilized shear strength and a reduced void ratio in arbitrarily-shaped assemblies when compared to corresponding results obtained from circular-shaped assemblies.

The proposed experimental approach lead to significant new insights into the force transmission and shear strength of granular materials. We addressed one of the central question of the Chapter: to what degree do the force chains observed in idealized granular assemblies pertain to assemblies with arbitrary and complex grain shapes? The results showcased that, in the arbitrarily-shaped assembly, the contact forces tend to form heterogeneous chain-like structures that are characteristic signatures of the emergence of force chains. Nonetheless, as grain shapes derive from idealized circles, contact forces are more uniformly distributed and have a significantly lower chance to reach large values. As a result, force chains seem to be less prevalent in arbitrarily-shaped assemblies. This finding raises the interesting possibility that this trend may be even more accentuated in 3D granular samples and that the existence of force chains may be biased by the technique used to observe them (e.g., photoelasticity in 2D circular-shaped assemblies).

The force transmission in the circular- and arbitrarily-shaped assemblies was further investigated by categorizing the contacts depending on their rolling, sliding and interlocking mechanisms. In circular-shaped assemblies, there seems to be a clear structuring of interlocking contact forces into filaments, which favors the emergence of force chains. Our experimental results suggest that force chains travel through interlocking contacts which seem to drive strength. The enhanced mobilized shear strength in arbitrarily-shaped assemblies was elucidated by analyzing the relative contribution of rolling, sliding and interlocking contacts to the total shear strength. We report that, while the fraction of interlocking contacts remains fairly constant, their contribution to mobilized strength increases as shear deformation progresses. Interlocking contacts enable the development of a stable force network which results in greater shear strength. Rolling and sliding are not as favorable contact mechanisms to driving mobilized strength.

Our findings demonstrate that a simplified model of circular-shaped grains cannot reflect the complex interactions between grains in real arbitrarily-shaped granular

assemblies. By extracting and understanding realistic grain-scale data, this research lays the groundwork to develop general, physic-based constitutive models for effectively capturing the behavior of granular materials.

Chapter 6

CONCLUSIONS AND FUTURE WORK

6.1 Conclusions

In this thesis, we employed novel laboratory experiments to shed light into the shear behavior and shear strength of granular materials. We presented a multiscale approach in which grain-scale mechanics are experimentally measured and homogenized to obtain enriched macroscopic quantities. A crucial aspect of this work is the ability to extract key grain-scale quantities, such as grain kinematics and contact forces, using image-based techniques.

In Chapter 2, measurements of dilatancy and grain kinematics were used as input into a rate-dependent plasticity model. Our results demonstrated that the proposed theoretical framework accurately captures the triggering, evolution of the flow and runout of transient avalanches in a rotating drum. This work has advanced our understanding of the mechanism governing the solid-fluid-like transition observed in granular avalanches.

Chapter 3 outlines a force inference technique (GEM) that provides a mathematical framework for studying the force network in granular materials. The strength of GEM lies in its applicability to grains of arbitrary shapes and opacity, various loading conditions (e.g., quasi-static or dynamic), and non-Hertzian contacts. We took advantage of GEM capabilities to conduct the research presented in Chapters 4 and 5.

In Chapter 4, we introduced a custom-built mechanical apparatus generating shear deformations while simultaneously applying a constant normal stress on a 2D-analogue granular assembly. When combined with DIC and GEM, this novel experimental capability furnishes unique data on the mechanics of granular materials at different scales, including continuum measures of stresses and discrete measures of grain kinematics and contact forces. Uniaxial compression and shear tests, where a typical macroscopic behavior of dense samples was observed, served as benchmark tests and highlighted the validity of the experimental procedure. The results show that the shear strength of the granular assembly depends on its geometrical (fabric) and mechanical (force) anisotropy.

In Chapter 5, utilizing the designed experimental apparatus, we visualized and quantitatively characterized force networks in an arbitrarily-shaped granular assembly, derived from a real sand sample. A comparison with a circular-shape assembly provided insights into the influence of grain shapes on the force distribution and shear strength of granular materials. We reported that strong force chains are less likely to develop in non-circular assemblies. Our results showcased that interlocking is the dominant grain-scale mechanism responsible for an increase in shear strength in non-circular assemblies. This work illuminates the grain-scale origin of macroscopic shear strength and demonstrates the potential of the proposed tools for constructing physic-based constitutive models.

6.2 Future work

Our experimental work on granular avalanches opens up interesting avenues to explore. A natural extension of the presented work is to study the effect of grain characteristics, (e.g., grain shape and grain size distribution) on the mechanical behavior of granular avalanches in a rotating drum. The proposed experimental approach allows to measure grain kinematics, such as the velocity distribution with depth, shear and volumetric strains and dilatancy evolution, for various grain characteristics. The wealth of knowledge amassed from these kinematics could ultimately be used to grasp the physics behind granular avalanches.

The shear apparatus combined with advanced grain-scale characterization techniques constitute important resources for future studies. Building on these achievements, we are currently using grain-scale data obtained from shear tests on circular- and arbitrarily-shaped assemblies to quantitatively validate DEM and LS-DEM simulations. This validation procedure is a critical step in ensuring that discrete element simulations produce faithful micromechanical behavior.

Moreover, the experimental technique has a great potential to investigate various experimental configurations. For instance, the role of inter-particle friction on the grain-scale contact mechanisms, e.g., interlocking, remains elusive and could be explored by coating individual grains with materials of varying frictional properties. Another promising feature of the shear apparatus is its capability to perform cyclic loading at different shear rates, which is of great interest to geotechnical engineers. The proposed experimental procedure could be employed to deepen our understanding of the micro- to macroscopic response of granular materials under cyclic loading and its dependence on shear rate.

As grain breakage is of particular importance to many applications including geotechnical, defense and bio-medical, the experimental setup could be used to investigate the redistribution of force networks upon grain breakage. Grains could be engineered such that breakage occurs at pre-determined planes at an easily achievable level of stress. Such tests could also serve as a validation of fracture models implemented into DEM codes.

This work provided unique data on the evolution of force chains during uniaxial compression and shear loading. Further analysis of the obtained data could enrich our knowledge of the conditions conducive to the formation, perpetuation, and breakage of force chains. Identifying the criteria associated with the life-cycle of a force chain would enable the prediction of the force network in realistic granular assemblies.

More broadly, given the rich data sets of grain-scale quantities obtained during the aforementioned shear tests, machine learning algorithms could be applied to identify connections between grain-scale characteristics and mechanical properties of granular assemblies.

Appendix A

GRANULAR AVALANCHES

A.1 Determination of the governing equation of the flow

In this appendix, we show how the governing equation of the granular flow (A.1) is derived from the linear momentum balance equation.

$$\frac{a}{g} = \cos\theta\,(\tan\theta - \mu) \tag{A.1}$$

Let us consider a granular flow along an inclined infinite slope. The position in the flow direction and in the flow depth direction are labeled x and y, respectively. The free surface of the flow makes an angle θ with the horizontal.

The local statement of linear momentum balance expressed in full gives:

$$\frac{\partial \sigma_{xx}}{\partial x} + \frac{\partial \sigma_{xy}}{\partial y} + \rho\, g\, \sin\theta = \rho\, a_x \tag{A.2a}$$

$$\frac{\partial \sigma_{yx}}{\partial x} + \frac{\partial \sigma_{yy}}{\partial y} + \rho\, g\, \cos\theta = \rho\, a_y \tag{A.2b}$$

Exploiting the infinite character of the problem, we assume that the stress components do not vary in the x-direction, such that: $\frac{\partial \sigma_{xx}}{\partial x} = \frac{\partial \sigma_{yx}}{\partial x} = 0$. Hence, by writing $\sigma_{yy} = \sigma$ and $\sigma_{xy} = \tau$, we obtain:

$$\frac{\partial \tau}{\partial y} + \rho\, g\, \sin\theta = \rho\, a_x \tag{A.3a}$$

$$\frac{\partial \sigma}{\partial y} + \rho\, g\, \cos\theta = \rho\, a_y \tag{A.3b}$$

The definition of dilatancy β is given by:

$$\beta = \frac{d\epsilon_{yy}}{d\epsilon_{xy}} = \frac{dy}{dx} = \frac{v_y}{v_x} \quad \Rightarrow \quad v_y = \beta\, v_x \tag{A.4}$$

We know that in the fluid-like state the granular material reaches critical state so that $\beta = 0$. Therefore, we must have $v_y = 0$ and $a_y = 0$. Equation (A.3b) can be rewritten as:

$$\frac{\partial \sigma}{\partial y} = -\rho\, g \cos\theta \tag{A.5}$$

Recalling Coulomb friction law and using the previous expression, we have:

$$\frac{\partial \tau}{\partial y} = \mu\, \frac{\partial \sigma}{\partial y} = -\mu\, \rho\, g \cos\theta \tag{A.6}$$

Combining equation (A.3a) with equation (A.6) further gives:

$$-\mu\, g \cos\theta + g \sin\theta = a_x \tag{A.7}$$

By denoting the surface acceleration in the flow direction a_x by a, we finally obtain the governing equation of the granular flow from (A.7):

$$\frac{a}{g} = \cos\theta\, (\tan\theta - \mu) \tag{A.8}$$

A.2 Determination of the difference between the angle of avalanche θ_A and angle of repose θ_R

Knowing that in the solid-like state the surface acceleration $a = 0$ and the mobilized friction $\mu = \beta + \mu_l$, equation (2.2) can be expressed as:

$$\sin\theta = \beta \cos\theta + \mu_l \cos\theta \tag{A.9}$$

Multiplying each side of equation (A.9) by $\cos\theta_R$, we have:

$$\sin\theta \cos\theta_R = \beta \cos\theta \cos\theta_R + \mu_l \cos\theta \cos\theta_R \tag{A.10}$$

Using the formula $\sin(x - y) = \sin x \cos y - \cos x \sin y$, we obtain:

$$\sin(\theta - \theta_R) + \cos\theta \sin\theta_R = \beta \cos\theta \cos\theta_R + \mu_l \cos\theta \cos\theta_R \tag{A.11}$$

Moreover, we defined the parameter μ_l to be $\mu_l = \tan\theta_R$, such that:

$$\sin(\theta - \theta_R) + \cos\theta \sin\theta_R = \beta \cos\theta \cos\theta_R + \cos\theta \sin\theta_R \tag{A.12}$$

$$\Leftrightarrow \sin(\theta - \theta_R) = \beta \cos\theta \cos\theta_R \tag{A.13}$$

$$\Leftrightarrow \tan(\theta - \theta_R) = \beta\, \frac{\cos\theta \cos\theta_R}{\cos(\theta - \theta_R)} \tag{A.14}$$

Once the inclination angle is equal to the angle of avalanche θ_A, the dilatancy reaches its peak value β^*. Therefore, the previous equation can be rewritten as:

$$\tan\Delta\theta = \beta^*\, \frac{\cos\theta_A \cos\theta_R}{\cos\Delta\theta} \tag{A.15}$$

BIBLIOGRAPHY

[1] H. M. Jaeger, S. R. Nagel, and R.P. Behringer. "Granular solids, liquids, and gases". In: *Reviews of Modern Physics* 68 (1996), p. 1259.

[2] K.H. Roscoe, A.N. Schofield, and C.P. Wroth. "On the Yielding of Soils". In: *Géotechnique* 8 (1958), pp. 22–53.

[3] A.N. Schofield and P. Wroth. *Critical State Soil Mechanics*. McGraw-Hill Book Co., London, England, 1968.

[4] D.M. Wood. *Soil Behavior and Critical State Soil Mechanics*. Cambridge University Press, Cambridge, England, 1991.

[5] R.H.G. Parry. *Stress-Strain Behavior of Soils*. G.T. Foulis and Co., Henley, England, 1972.

[6] K. Alshibli et al. "Assessment of Localized Deformations in Sand Using X-Ray Computed Tomography". In: *Geotechnical Testing Journal* 23 (2000), pp. 274–299.

[7] S.A. Hall et al. "Discrete and continuum analysis of localized deformation in sand using X-ray micro CT and volumetric digital image correlation". In: *Géotechnique* 60 (2010), pp. 315–322.

[8] V. Cnudde and M.N. Boone. "High-resolution X-ray computed tomography in geosciences: A review of the current technology and applications". In: *Earth-Science Reviews* 123 (2013), pp. 1–17.

[9] S.A. Hall et al. "Can intergranular force transmission be identified in sand?" In: *Granular Matter* 13 (2011), pp. 251–254.

[10] R.C. Hurley et al. "Quantifying Interparticle Forces and Heterogeneity in 3D Granular Materials". In: *Phys Rev Lett* 117 (2016), p. 098005.

[11] F. Calvetti, G. Combe, and J. Lanier. "Experimental Micromechanical Analysis of a 2D Granular Material: Relation between Structure Evolution and Loading Path". In: *Mech of Cohesive Frictional Material* 2 (1997), pp. 121–163.

[12] J. Ren, J.A. Dijksman, and R.P. Behringer. "Reynolds pressure and relaxation in a sheared granular system". In: *Phys Rev Lett* 110 (2013), p. 018302.

[13] T. Miller et al. "Eddy Viscosity in Dense Granular Flows". In: *Phys Rev Lett* 111.229902 (2013).

[14] P.A. Cundall and O.D.L. Strack. "A Discrete Numerical Model for Granular Assemblies". In: *Géotechnique* 29 (1979), pp. 47–65.

[15] L. Rothenburg and R.J. Bathurst. "Analytical Study of Induced Anisotropy in Idealized Granular Materials". In: *Geotechnique* 39 (1989), pp. 601–614.

[16] A.A. Peña, P.G. Lind, and H.J. Herrmann. “Modeling slow deformation of polygonal particles using DEM”. In: *Particuology* 6 (2008), pp. 506–514.

[17] *Evaluating the influence of particle shape on liquefaction behavior using discrete element method*. Proceedings of the thirteenth international offshore and polar engineering conference (ISOPE 2003), Honolulu, Hawaii. 2003.

[18] C. Thornton. “Numerical Simulations of Deviatoric Shear Deformation of Granular Media”. In: *Géotechnique* 50 (2000), pp. 43–53.

[19] D. Zhao et al. “Three-dimensional discrete element simulation for granular materials”. In: *Engineering Computations* 23 (2006), pp. 749–770.

[20] P.W. Rowe. “The Stress-Dilatancy Relation for Static Equilibrium of an Assembly of Particle in Contact”. In: *Proc R. Soc A* 269 (1962), pp. 500–527.

[21] D.W. Taylor. *Fundamentals of Soil Mechanics*. John Wiley and Sons, 1948.

[22] O Reynolds. “On the dilatancy of media composed of rigid particle in contact”. In: *Philos. Mag. Ser.5* 20 (1885), pp. 469–481.

[23] G.D.R. Midi. “On dense granular flow”. In: *Eur. Phys. J. E.* 14 (2004), pp. 341–365.

[24] P. Jop, Y. Forterre, and O. Pouliquen. “Crucial role of side walls for granular surface flows: consequences for the rheology”. In: *J. Fluid Mech.* 541 (2005), pp. 167–192.

[25] P. Jop, Y. Forterre, and O. Pouliquen. “A constitutive law for dense granular flows”. In: *Nature* 441 (2006), pp. 727–730.

[26] Y. Forterre and O. Pouliquen. “Flows of Dense Granular Media”. In: *Annu. Rev. Fluid Mech.* 40 (2008), pp. 1–24.

[27] F. da Cruz et al. “Rheophysics of dense granular materials: Discrete simulation of plane shear flows”. In: *Phys. Rev. E.* 72 (2005), p. 021309.

[28] J.E. Andrade et al. “On the rheology of dilative granular media: Bridging solid and fluid-like behavior”. In: *J. Mech. Phys. Solids* 60 (2012), pp. 1122–1136.

[29] P. Dantu. “Etude statistique des forces intergranulaires dans un milieu pulverent”. In: *Geotechnique* 18 (1968), pp. 50–55.

[30] A. Drescher. “Photoelastic verification of a mechanical model for the flow of a granular material”. In: *J. of Mech. And Phys. of Solids* 20 (1972), pp. 337–340.

[31] M. M. Frocht. *Photoelasticity*. Vol. 1. New York: Wiley, 1941.

[32] M. M. Frocht. *Photoelasticity*. Vol. 2. New York: Wiley, 1941.

[33] T.S. Majmudar and R.P. Behringer. “Contact Force Measurements and Stress-Induced Anisotropy in Granular Materials”. In: *Nature* 435 (2005), pp. 1079–1082.

[34] K.E. Daniels, J.E. Kollmer, and J.G. Puckett. “Photoelastic force measurements in granular materials”. https://arxiv.org/abs/1612.03525. 2016.

[35] M. Cates et al. “Jamming, force chains and fragile matter”. In: *Phys Rev Lett* 81 (1998), pp. 1841–1844.

[36] R. Hartley and R.P. Behringer. “Logarithmic rate dependence of force network in sheared granular materials”. In: *Nature* 421 (2003), pp. 928–931.

[37] K.E. Daniels and N.W. Hayman. “Force chains in seismogenis fault visualized with photoelastic granular shear experiments”. In: *Journal of Geophysical Research* 113 (2008), B11411.

[38] D. Howell and R.P. Behringer. “Stress Fluctuations in a 2D Granular Couette Experiment: A Continuous Transition”. In: *Phys. Rev. Lett.* 82 (1999), p. 5241.

[39] D. Bi et al. “Jamming by shear”. In: *Nature* 480 (2011), pp. 355–358.

[40] A. Shukla. “Dynamic photoelasticity studies of wave propagation in granular media”. In: *Optics and Laser in Engineering* 14 (1991), pp. 165–184.

[41] A.H. Clark, L. Kondic, and R.P. Behringer. “Particle Scale Dynamics in Granular Impact”. In: *Phys Rev Lett* 109 (2012), p. 238302.

[42] G. Huillard, X. Noblin, and J. Rajchenbach. “Propagation of acoustic waves in a one-dimensional array of noncohesive cylinders.” In: *Phys. Rev. E.* 84 (2011), p. 016602.

[43] A.L. Rechenmacher. “Grain-scale processes governing shear band initiation and evolution in sands”. In: *J. of Mech. And Phys. of Solids* 63 (2005), pp. 154–166.

[44] S. Hall et al. “Localised Deformation Patterning in 2D Granular Materials Revealed by Digital Image Correlation”. In: *Granular matter* 12 (2009), pp. 1–14.

[45] G. Lionello and L. Cristofolini. “A practical approach to optimizing the preparation of speckle patterns for digital-image correlation”. In: *Measurement Science and Technology* 25 (2014), p. 107001.

[46] P. Lava et al. “Assessment of measuring errors in DIC using deformation fields generated by plastic FEA”. In: *OPTICS AND LASERS IN ENGINEERING* 47 (2009), pp. 747–753.

[47] C. Sebastian and E.A. Patterson. “Calibration of a digital image correlation system”. In: *Experimental Tachniques* 39 (2012), pp. 21–29.

[48] Pan B., Yu L., and Wu D. “High-accuracy 2D digital image correlation measurements with bilateral telecentric lenses: error analysis and experimental verification”. In: *Experimental Mechanics* 53 (2013), pp. 1719–1733.

[49] A. Daerr and S. Daoudy. “Two types of avalanche behaviour in granular media”. In: *Nature* 399 (1999), pp. 241–243.

[50] H. M. Jaeger and S. R. Nagel. “Physics of Granular State”. In: *Science* 255 (1992), pp. 1523–1531.

[51] J. Rajchenbach. “Flow in powders: From discrete avalanches to continuous regime”. In: *Phys. Rev. Lett.* 65 (1990), pp. 2221–2224.

[52] José E. Andrade and Carlos F. Avila. “Granular element method (GEM): linking inter-particle forces with macroscopic loading”. In: *Granular Matter* 14 (2012), pp. 51–61.

[53] M. Pailha and O. Pouliquen. “A two-phase flow description of the initiation of underwater granular avalanches”. In: *J. Fluid Mech.* 633 (2009), pp. 115–136.

[54] N. Prime, F. Dufour, and F. Darve. “Solid-fluid transition modelling in geomaterials and application to a mudflow interacting with an obstacle”. In: *Int. J. Numer. Anal. Methods Geomech* 38 (2014), pp. 1341–1361.

[55] C. Peng et al. “Unified modelling of granular media with Smoothed Particle Hydrodynamics”. In: *Acta Geotechnica* 11 (2016), p. 1231.

[56] P. Evesque. “Analysis of the statistics of sandpile avalanches using soil-mechanics results and concepts”. In: *Phys. Rev. A* 43 (1991), pp. 2720–2740.

[57] D.R. Lowe. “Grain flow and grain flow deposits”. In: *J. Sediment. Petrol.* 46 (1976), pp. 188–199.

[58] C.H. Reinsch. “Smoothing by Spline Functions”. In: *Numer. Math* 10 (1967), pp. 177–183.

[59] J.M.N.T Gray. “Granular flow in partially filled slowly rotating drums”. In: *J. Fluid Mech.* 441 (2001), pp. 1–29.

[60] A. Orpe and D.V. Khakhar. “Scaling relations for granular flow in quasi-two-dimensional rotating cylinders”. In: *Phys. Rev. E.* 64 (2001), p. 031302.

[61] B. Pan et al. “Robust full-field measurement considering rotation using digital image correlation”. In: *Meas. Sci. Technol.* 20 (2009), p. 062001.

[62] M.A. Sutton, J.J. Orteu, and H. Schreier. *Image Correlation for Shape, Motion and Deformation Measurements: Basic Concepts,Theory and Applications*. Springer US, 2009.

[63] A.J. Kabla and T.J. Senden. “Dilatancy in slow granular flow”. In: *Phys. Rev. Lett.* 102 (2009), p. 28301.

[64] O. Pouliquen and N. Renaut. “Onset of Granular Flows on an Inclined Rough Surface: Dilatancy Effects”. In: *J. Phys. II France* 6 (1996), pp. 923–935.

[65] M. Pailha, M. Nicolas, and O. Pouliquen. “Initiation of underwater granular avalanches: influence of the initial volume fraction”. In: *Phys. Fluids* 20 (2008), p. 11701.

[66] R.M. Iverson and D.L. George. “A depth-averaged debris-flow model that includes the effects of evolving dilatancy. I. Physical basis”. In: *Proc R. Soc A* 470 (2014), p. 20130819.

[67] D.L. George and R.M. Iverson. “A depth-averaged debris-flow model that includes the effects of evolving dilatancy. II. Numerical predictions and experimental tests”. In: *Proc R. Soc A* 470 (2014), p. 20130820.

[68] R. Fischer et al. “Dynamics of dry granular avalanches”. In: *Phys. Rev. E.* 78 (2008), p. 021302.

[69] F. Forsberg and C.R. Siviour. “3D deformation and strain analysis in compacted sugar using x-ray microtomography and digital volume correlation”. In: *Measurement Science and Technology* 20 (2009), p. 095703.

[70] R. J. Bathurst and L. Rothenburg. “Observations on stress-force-fabric relationships in idealized granular materials”. In: *Mechanics of Materials* 9 (1990), pp. 65–80.

[71] S. N. Coppersmith et al. “Model for force fluctuations in bead packs”. In: *Physical Review E.* 53 (1996), pp. 4673–4685.

[72] N. Guo and J. Zhao. “The signature of shear-induced anisotropy in granular media”. In: *Computers and Geotechnics* 47 (2013), pp. 1–15.

[73] C. Liu et al. “Force Fluctuations in Bead Packs”. In: *Science* 269 (1995), pp. 513–515.

[74] S. Ostojic, E. Somfai, and B. Nienhuis. “Scale invariance and universality of force networks in static granular matter”. In: *Nature* 439 (2006), pp. 828–830.

[75] F. Radjai et al. “Force Distributions in Dense Two-Dimensional Granular Systems”. In: *Physical Review Letters* 77 (1996), pp. 274–277.

[76] F. Radjai et al. “Bimodal character of stress transmission in granular packing”. In: *Phys. Rev. Lett.* 80 (1998), pp. 61–64.

[77] M. Satake. “Fabric tensor in granular materials”. In: *Deformation and Failure of Granular Materials*. Ed. by P.A. Vermeer and H. J. Luger. 1982, pp. 63–68.

[78] J.-P. Bouchaud et al. “Force chain splitting in granular materials: A mechanism for large-scale pseudo-elastic behaviour”. In: *The European Physical Journal E* 4 (2001), pp. 451–457.

[79] P. Claudin et al. “Models of stress fluctuations in granular media”. In: *Physical Review E.* 57 (1998), pp. 4441–4457.

[80] M. Saadatfar et al. “Mapping forces in a 3D elastic assembly of grains”. In: *Journal of the Mechanics and Physics of Solids* 60 (2012), pp. 55–66.

[81] J. Zhou et al. “Measurement of Forces Inside a Three-Dimensional Pile of Frictionless Droplets”. In: *Science* 312 (2006), pp. 1631–1633.

[82] Ryan Hurley et al. “Extracting inter-particle forces in opaque granular materials: Beyond photoelasticity”. In: *Journal of the Mechanics and Physics of Solids* 63 (2014), pp. 154–166.

[83] R.C. Hurley et al. “Dynamic inter-particle force inference in granular materials: Method and application”. In: *Experimental Mechanics* 56 (2016), pp. 217–229.

[84] D.H. Ballard. “Generalizing the Hough transform to detect arbitrary shapes”. In: *Pattern Recognition* 13 (1981), pp. 111–122.

[85] T. Peng. *Detect circles with various radii in grayscale image via hough transform*.

[86] R.C. Gonzalez, R.E. Woods, and S.L. Eddins. *Digital Image Processing using Matlab*. Pearson Prentice Hall, New Jersey, 2004.

[87] J.C. Russ. *The Image Processing Handbook, 5th edition*. CRC Press, 2007.

[88] P. Soille. *Morphological Image Analysis - Principles and Applications, 2nd edition*. Springer-Verlag, New York, 2003.

[89] *Vic-2D, Reference Manual*.

[90] *Vic-2D, Testing Guide*.

[91] M. Grant and S. Boyd. *CVX: Matlab Software for Disciplined Convex Programming, version 1.21*. 2011.

[92] D. Kalyanmoy. *Multi-objective optimization using evolutionary algorithms*. John Wiley and Sons, 2001.

[93] I. Das. “On characterizing the knee of the Pareto curve based on normal-boundary intersection”. In: *Structural Optimization* 18 (1999), pp. 107–115.

[94] J.F. Doyle. *Manual on experimental stress analysis*. Society for Experimental Mechanics, 1989.

[95] J. Christoffersen, M.M. Mehrabadi, and S. Nemat-Nasser. “A micromechanical description of granular material behavior”. In: *J. Appl. Mech* 48 (1981), pp. 339–344.

[96] R. V. Martins et al. “Simultaneous measurement of the strain tensor of 10 individual grains embedded in an Al tensile sample”. In: *Materials Science and Engineering: A* 387 (2004), pp. 84–88.

[97] J-P Bardet. *Experimental Soil Mechanics*. Prentice Hall, Upper Saddle River, NJ, USA, 1997.

[98] A.W. Bishop and D.J. Henkel. *The Measurement of Soil Properties in the Triaxial Test*. Hodder Arnold H&S, London, England, 1970.

[99] W. Kjellman. "Testing the shear strength of clay in Sweden". In: *Géotechnique* 2 (1951), pp. 225–232.

[100] K.H. Roscoe. "An Apparatus for the Application of Simple Shear to Soil Samples". In: *Proc. 3rd Int. Conf. Soil Mechanics Foundation Engineering, Zurich*. 1953, pp. 186–191.

[101] A. Casagrande. "Characteristics of Cohesionless Soils Affecting the Stability of Slopes and Earth Fills". In: *Journal of the Boston Society of Civil Engineers* (1936).

[102] M. Oda, S. Nemat-Nasser, and J. Konishi. "Stress-Induced Anisotropy in Granular Masses". In: *Soils Found.* 25 (1985), pp. 85–97.

[103] C. Thornton. "Induced Anisotropy and Energy Dissipation in Particulate Material - Results from Computer-Simulated Experiments - Yielding, Damage, and Failure of Anisotropic Solids". In: *Mech Eng Pub London* (1990), pp. 113–130.

[104] H. Ouadfel and L. Rothenburg. "'Stress-force-fabric' Relationship for Assemblies of Ellipsoids". In: *Mech. Mater.* 33 (2001), pp. 201–221.

[105] S. Masson and J. Martinez. "Micromechanical Analysis of the Shear Behavior of a Granular Material". In: *J. of Eng. Mech.* 127 (2001), pp. 1007–1016.

[106] L. Cui and C. O'Sullivan. "Exploring the Macro- and Micro-Scale Response of an Idealised Granular Material in the Direct Shear Apparatus". In: *Géotechnique* 56 (2006), pp. 455–468.

[107] P. Fu and Y. F. Dafalias. "Fabric Evolution within Shear Bands of Granular Materials and its Relation to Critical State Theory". In: *Int. J. Numer. Anal. Methods Geomech* 35 (2011), pp. 1918–1948.

[108] H. Matsuoka. "A Microscopic Study of Shear Mechanism of Granular Materials". In: *Soils and Foundations* 14 (1974), pp. 29–43.

[109] M. Oda and J. Konishi. "Rotation of Principal Stresses in Granular Material during Simple Shear". In: *Soils and Foundations* 14 (1974), pp. 39–53.

[110] M. Oda and J. Konishi. "Microscopic Deformation Mechanism of Granular Material in Simple Shear." In: *Soils and Foundations* 14 (1974), pp. 25–38.

[111] S.A. Hall et al. "Experimental Characterisation of (Localised) Deformation Phenomena in Granular Geomaterials from Sample down to Inter- and Intra-Grain Scales". In: *Procedia IUTAM*. Vol. 4. 2012, pp. 54–65.

[112] C. Vitone et al. “Localized Deformation in Intensively Fissured Clays Studied by 2D Digital Image Correlation”. In: *Acta Geotechnica* 8 (2013), pp. 247–263.

[113] S. Timoshenko and J.N. Goodier. *Theory of Elasticity*. McGraw-Hill Book Co, New York, 1951.

[114] K.V.N Surendra and K.R.Y. Simha. “Characterizing Frictional Contact Loading via Isochromatics”. In: *Experimental Mechanics* 54 (2014), pp. 1011–1030.

[115] M. Oda and J. Konishi. “Rotation of Principal Stresses in Granular Material during Simple Shear”. In: *Soils and Foundations* 14 (1974), pp. 39–53.

[116] K.H. Roscoe, R.H. Bassett, and E.R.L. Cole. “Principal axes observed during simple shear of a sand”. In: *Proc. Geotech. Conf, Oslo*. 1967, pp. 231–237.

[117] J. Duran. *Sands, Powders, and Grains: An Introduction to the Physics of Granular Materials*. Springer-Verlag New York, 2000.

[118] K. Iwashita and M. Oda. *Mechanics of Granular Materials: An Introduction*. CRC Press, 1999.

[119] J.F. Peters et al. “Characterization of force chains in granular material”. In: *Phys. Rev. E.* 72 (2005), p. 041307.

[120] D.M. Mueth, H.M. Jaeger, and S.R Nagel. “Force distribution in a granular medium”. In: *Phys. Rev. E.* 57 (1998), p. 3164.

[121] I. Holubec and E. D’Appolonia. “Effect of particle shape on the engineering properties of granular soils”. In: *ASTM STP* 523 (1973), pp. 304–318.

[122] J.M. Ting, L. Meachum, and J.D. Rowell. “Effect of particle shape on the strength and deformation mechanisms of ellipse-shaped granular assemblages”. In: *Engineering Computations* 12 (1995), pp. 99–108.

[123] K. Miura et al. “Mechanical characteristics of sands with different primary propertiesq”. In: *Soils and Foundations* 38 (1998), pp. 159–172.

[124] S.J.M. Yasin and A.M.M. Safiullah. “Effect of particle characteristics on the strength and volume change behavior of sand”. In: *Journal of Civil Engineering* 31 (2003), pp. 127–148.

[125] G-C Cho, J Dodds, and J.C. Santamarina. “Particle Shape Effects on Packing Density, Stiffness, and Strength: Natural and Crushed Sands”. In: *Journal of Geotechnical and Geoenvironmental Engineering* 132 (2006), p. 1473.

[126] A.G. Athanassiadis et al. “Particle Shape Effects on the Stress Response of Granular Packings”. In: *Soft Matter* 10 (2014), pp. 48–59.

[127] S. Wegner et al. “Effects of grain shape on packing and dilatancy of sheared granular materials”. In: *Soft Matter* 10 (2014), pp. 5157–5167.

[128] W.G. Holtz and H.J. Gibbs. “Triaxial Shear Tests on Pervious Gravelly Soils”. In: *Journal of the Soil Mechanics and Foundations Division* 82 (1956), pp. 1–22.

[129] W.G. Holtz and H.J. Gibbs. “Triaxial shear characteristics of clayey gravel soils”. In: *Journal of the Soil Mechanics and Foundations Division* 82 (1956), pp. 143–149.

[130] K.W. Lim et al. “Multiscale characterization and modeling of granular materials through a computational mechanics avatar: a case study with experiment”. In: *Acta Geotechnica* 11 (2016), pp. 243–253.

[131] I. Vlahinić et al. “Towards a more accurate characterization of granular media: extracting quantitative descriptors from tomographic images”. In: *Granular Matter* 16 (2014), pp. 9–21.

[132] H. Wadell. “Volume, shape, and roundness of quartz particles”. In: *The Journal of Geology* 43 (1935), pp. 250–280.

[133] J.C. Santamarina and G.C. Cho. “Soil behaviour: The role of particle shape”. In: *Advances in geotechnical engineering: the Skempton conference*. Vol. 1. 2004, pp. 604–617.

[134] J. Zheng and R.D. Hrycim. “Traditional soil particle sphericity, roundness and surface roughness by computational geometry”. In: *Géotechnique* 65 (2015), pp. 494–506.

[135] Stratasys Ltd. *Professional 3D-Printing*. `http://www.stratasys.com`. [Online; accessed 04.30.18]. 2018.

[136] Stratasys Ltd. *PolyJet Technology*. `http://www.stratasys.com/3d-printers/technologies/polyjet-technology`. [Online; accessed 04.30.18]. 2018.

[137] J. Mueller, K. Shea, and C. Daraio. “Mechanical properties of parts fabricated with inkjet 3D printing through efficient experimental design”. In: *Materials and Design* 86 (2015), pp. 902–912.

[138] T. Chen, J. Mueller, and K. Shea. “Integrated design and simulations of tunable, multi-state structures fabricated monolithically with multi-material 3D printing”. In: *Scientific Reports* 7 (2017), p. 45671.

[139] E. Marteau and J.E. Andrade. “A novel experimental device for investigating the multiscale behavior of granular materials under shear”. In: *Granular Matter* (2017).

[140] L.E. Silbert et al. “Geometry of frictionless and frictional sphere packings”. In: *Phys. Rev. E.* 65 (2002), p. 031304.

[141] E. Azema and F. Radjai. “Stress-strain behavior and geometrical properties of packings of elongated particles”. In: *Phys. Rev. E.* 81 (2010), p. 051304.

[142] E. Azema and F. Radjai. “Force chains and contact network topology in packings of elongated particles”. In: *Phys. Rev. E.* 82 (2011), p. 031303.

[143] V. Richefeu, G. Combe, and G. Viggiani. “An experimental assessment of displacement fluctuations in a 2D granular material subjected to shear”. In: *Geotechnique Letters* 2 (2012), pp. 113–118.

[144] N. Estrada, A. Toboada, and F. Radjai. “Shear strength and force transmission in granular media with rolling resistance”. In: *Phys. Rev. E.* 78 (2008), p. 021301.